The Recombination Spectrum of Carbon II

Alisdair Richard Davey
Department of Physics & Astronomy
University College London

A thesis submitted for the degree of Doctor of Philosophy
in the Faculty of Science of the University of London.

November 1994

Abstract

The determination of the physical parameters of various astrophysical plasmas requires accurate calculation of the radiative and collisional processes involved. The recombination spectrum of Carbon II lends itself to investigating regions such as gaseous nebulae and low temperature stellar winds. In this thesis, a detailed treatment of the recombination processes of CII has been carried out, covering a wide range of temperatures and densities.

Accurate photoionisation calculations, using the R-matrix solution to the close coupling equations have been performed. In the process, bound state energy levels have been determined and new weighted oscillator strengths calculated, over a larger range and with a greater accuracy, than had been previously achieved. With careful attention to resonances, which dominate the recombination at low temperatures, recombination coefficients have been evaluated for all states up to $n = 15, L = 4$. As well as radiative processes, all important collisional processes have been included, creating a full collisional-radiative-cascade model, in order to determine the populations of the states of CII at varying temperatures and densities. Detailed comparison with previous theoretical work has been made.

The application of the CII recombination spectrum to the observed spectra of two contrasting astrophysical plasmas such as cold nova shells and Wolf-Rayet stellar winds is considered. The usefulness and applicability of the CII recombination spectrum as a diagnostic tool is ably demonstrated.

In memory of my father, grandfather and grandmother, and for my mother.

'We don't tackle flying through rock until a little later in the programme.'

Jonathan Livingston Seagull by Richard S Bach

Acknowledgments

I would like to thank my supervisor Dr Peter Storey, without whose help, encouragement and excellent supervision, this thesis would never have been completed. I would also like to thank Dr Hannelore Saraph, for her help in my first year.

Many people have helped me along the way and I take great pleasure in mentioning them here. Wendy, to whom I shall always be grateful. Andy Phillips, with whom I shared many a meal and bottle of wine. The various inhabitants of A11, Paul, Liesl, Grahame, Caroline, Susan, David and the members of group C. Thanks for all the great lunches. Dr Tony Lynas-Grey, a man to whom I probably owe more 'jars' than a lifetime of drinking could consume. His help, and cups of coffee kept me going through many nights. To my friend who kept nagging me to finish. My love and appreciation.

A special word of thanks to Andy Reid and Barry Smalley for putting up with me for two years. My humblest apologies, for the alarm clock from hell and my grateful thanks for the shared journeys, the food and the violin music !

My thanks too, to Dr Paul Lamb and MSSL for giving me time to work on my thesis when I needed it.

I acknowledge receipt of a SERC (PPARC) grant, the financial aid of the Department of Physics and Astronomy, UCL, and the help of the personal lending assistants at Barclays Bank, Truro, Cornwall.

Last and most, to my family who have always let me do my own thing. Thank you for all your support and encouragement.

Contents

List of Figures

List of Tables

Chapter 1

Introduction

The study of the physical processes occurring in ionized plasmas of varying temperature and density has been of interest to astrophysicists for a long time. Formerly, the analysis and physical interpretation of the plasmas relied on strong emission lines. With the advances in equipment however, leading to observations of increased sensitivity and resolution, accurate measurement of the intensities of even weak emission lines in astrophysical plasmas can be made. The increase in the number of observed lines formed by recombination, has allowed more detailed analysis of, for example, gaseous nebulae. Any detailed analysis though, must rely on models which accurately and fully describe the processes which lead to the formation of the observed spectrum.

The physical principles governing the formation of recombination spectra are well defined and lead to a theory and model for calculating emission line spectra which may be easily compared to observations. By adjusting the model, fits to observed intensities can be made and the physical conditions of the astrophysical plasma under observation deduced. Provided all the atomic processes contributing to the levels of an ion have been suitably modeled, elemental abundances can be determined from recombination line fluxes. Recombination, followed by radiative cascade is important in populating bound excited states, whose energy levels, may be greater than the thermal kinetic energy of the gas. Recombination rates are also needed to determine the ionisation and thermal balance of the plasma. At low temperatures, recombination is believed to very significantly contribute to forbidden line emissivity (e.g Petitjean *et al.*, 1990) and may need to be considered in nebulae at higher temperatures. Effective recombination coefficients for metastable levels, are required in detailed modeling of nebula spectra and there is a general need for homogeneous sets of recombination coefficients and radiative transition probabilities as a basis for modeling and interpreting the observed data, over a wide range of wavelengths. It is the aim of this thesis to provide such a homogeneous set of data for Carbon II and to use the results in the interpretation of spectra.

1.1 Recombination Processes

The primary processes of recombination in astrophysical plasmas are three-body recombination, radiative recombination and dielectronic recombination;

$$\begin{array}{rcll} X_{n+} + e^- + e^- & \longrightarrow & X^*_{(n-1)+} + e^- & \text{Three} - \text{body} \\ X_{n+} + e^- & \longrightarrow & X^*_{(n-1)+} + h\nu_a & \text{Radiative} \\ X_{n+} + e^- & \longrightarrow & X^{**}_{(n-1)+} & \\ & \longrightarrow & X^*_{(n-1)+} + h\nu_b & \text{Dielectronic} \end{array} \qquad (1.1)$$

where X_{n+} is an ion of effective charge number n, $X^*_{(n-1)+}$ is an excited bound state of the recombined ion and $X^{**}_{(n-1)+}$ is a doubly excited autoionizing state.

Three-body recombination is the inverse process of collisional ionisation. The three body recombination / collisional ionisation rate is proportional to the square of the electron density and will generally not be important in regions of low density, (optically thin plasmas) such as those found in the interstellar medium and nebulae. In these cases recombination proceeds mainly to the ground state ions. However, it will be an important process, even at intermediate densities for states with a high principal quantum number or particularly a high total angular momentum. Three body recombination / collisional ionisation quickly becomes the dominant recombination process in dense regions, such as Wolf-Rayet stellar winds.

Radiative recombination is the inverse process of photoionisation and is dominant in low density, low temperature plasmas. It quickly becomes less important as the electron temperature rises. Recombination rates to the ground state complexes of many ions have been calculated from detailed photoionisation calculations, but this may ignore the recombination to higher excited states for which few detailed calculations have been performed.

The process of dielectronic recombination involves the radiationless capture of a free electron into a doubly excited state, quickly followed by radiative decay to a true bound state. Dielectronic recombination is known to be the dominant recombination process at high temperatures, but also is very significant at low temperatures (Storey, 1981), particularly when there are autoionising states which lie just above the ionisation threshold.

The most important radiative decays from autoionising states are generally those to the ground complex. Examples are C^{2+} $2p^2$ ^1D – $2s2p$ $^1P^0$ at λ2997 and C^+ $2s2p^2$ ^2D – $2s^22p$ $^2P^0$ at λ1335. Such lines have been observed in planetary nebulae and symbiotic stars.

1.2 Previous Work

The calculation of recombination rates, the generation of theoretical recombination spectra and their application to observations has been of interest to many authors. Varying degrees of completeness have been used in the models and in the approximations to the various radiative and collisional rates, needed to fully describe the physical processes involved. Some of the relevant work is mentioned here. The following list is not a history of calculating recombination spectra. The papers mentioned here are the ones having a bearing, to a lesser or greater degree, on the work carried out in this thesis. They contain information on the methods of solution of the level population equations, the atomic data used in the calculations and the application of theoretically determined recombination spectra to observations.

Much of the previous work has concentrated on hydrogen and hydrogenic ions. Brocklehurst (1971) calculated relative intensities of HI and compared them with observed intensities in the planetary nebula NGC 7662. These calculations were based on the recombination coefficients of Burgess (1965) and made allowance for collisional redistribution of angular momentum and energy using the impact parameter approximation, (Seaton, 1962). His results gave good agreement with photoelectric observations.

Aldrovandi and Péquignot (1973) made significant improvements in terms of the available atomic data, by calculating radiative and dielectronic recombination coefficients for all non-hydrogenic ions of He, C, N, O, Ne, Mg, Si and S, and giving them in the form of a fit, suitable for evaluation over a wide temperature range. They noted that in a large number of cases, hydrogenic approximations gave cross-sections that were in error by a factor two for complex ions. They also suggested that one of the possible explanations for the line intensities observed in planetary nebulae was dielectronic recombination at low temperatures.

Summers (1977) extended the work on the analysis of recombination and population structure described in Burgess and Summers (1976), to include angular momentum for highly excited states as well as lower ones and techniques for joining very many resolved and unresolved levels in an LS coupling approximation. Approximations were used for all collisional processes but dielectronic recombination was excluded as he considered a temperature range for Hydrogen and Helium at which it was 'switched off'.

Storey (1981), calculated rate coefficients for dielectronic recombination for the recombined ions C^+, C^{2+}, N^{2+}, N^{3+} and O^{4+} at the temperatures and densities appropriate to planetary nebulae. In his evaluation of effective recombination coefficients, he assumed that all states permitted to autoionize where in thermodynamic equilibrium and used transition probabilities, calculated with the multi-configuration atomic structure code, SUPERSTRUCTURE (Eissner *et al.*, 1974; Nussbaumer and Storey, 1978). Using an LS coupling scheme he neglected the effects of collisions, assuming that they would be negligible at typical nebular densities (10^4 cm^{-3}). This paper confirmed, that the CIII $2p^2$ $^1D \rightarrow 2s2p$ $^1P^0$ λ2996 line found in the spectra of planetary nebulae was indeed formed by dielectronic recombination as had been proposed. The calculation of dielectronic recombination coefficients was extended by Nussbaumer and Storey (1984), who gave fits to effective dielectronic recombination coefficients for a large number of lines, for all ions of CNO.

Mendoza (1982) reviewed atomic calculations and experiments of interest in the study of planetary nebulae. He gave a selected and critically evaluated compilation of transition probabilities, electron excitation rate coefficients and photoionisation cross-sections for a large number of ions.

Ferland *et al.* (1984) presented an analysis of the cold nova DQ Her. In this paper they gave data for CII and calculated effective recombination coefficients for λ1335 and λ4267. Then by comparing observed and theoretical intensity ratios, they were able to deduce the temperature in the nova shell. In their work they used a scaled hydrogenic approximation to the radiative recombination coefficients and evaluated the dielectronic component for λ1335 from Nussbaumer and Storey (1983), to obtain a very low temperature for nova DQ Her. Later work, Petitjean *et al.* (1990), Smits (1991) and this thesis, confirm the low temperature, but show that ratio of the theoretical intensities, $I(\lambda1335)/I(\lambda4267)$ give a temperature approximately double, that Ferland *et al.* (1984) derived.

Hummer and Storey (1987), extended the work of Brocklehurst (1971) to calculate relative intensities of HI and HeII, fully including collisional effects and considerably expanding the range of temperature, density and principal quantum number.

Seaton (1987) published the first paper of the collaborative effort referred to as the Opacity Project. This work included calculations of atomic energy levels, oscillator strengths and photoionisation cross-sections for a large number of ions producing some of the most accurate data to date. A set of codes employing the R-matrix formulation of the close coupling method was used to produce the data. These codes were used extensively in the course of this thesis. Yu Yan and Seaton (1987) calculated photoionisation cross-sections for CII as part of the project. The reasons for not using these cross-sections are considered later in this chapter and in chapter 2.

More recently, Péquignot *et al.* (1991) produced total and effective recombination coefficients for all H, He, C, N, O and Ne ions in the form of fits valid at low density and over a range of temperatures. They used explicitly calculated cross-sections for the ground state and $n = 2$ excited levels where available. For $n = 3$ states, the systematic cross-sections of Hofsaess (1979) were used. Where no data was available they interpolated or extrapolated from ions in the same isoelectronic series. They noted that for some ions, e.g. CII (Yu Yan and Seaton, 1987) there existed detailed cross-sections for excited states, but they declined to use them. Detailed comparison is made with Péquignot *et al.* (1991) in chapter 5.

Storey (1994) calculated rate coefficients for OII lines at nebular densities and temperatures. Previous work had used separate calculations of the radiative and dielectronic components of the total recombination coefficient to a state. In this paper, Storey used a unified approach, by deriving recombination coefficients directly from photoionisation cross-sections calculated by the *ab initio* methods of the Opacity Project.

1.3 Applications of Recombination Theory

Some of the applications of recombination theory have already been mentioned. They cover a wide range of objects and wavelengths but seem particularly suited to the analyses of objects such as planetary nebulae where the low electron temperature and density of the nebulae envelope give rise to a variety of atomic processes which would be difficult to reproduce and measure in more accessible laboratories. Analysis of the observations, relies heavily on theoretically calculated quantities. A review of the data used in such calculations was given by Mendoza (1982).

The modeling of the observed fluxes of lines formed by recombination, is often suitable for analysis using the recombination spectra of C, N and O ions. More recently, Liu *et al.* (1994), have produced detailed analyses of the planetary nebula NGC 7009. NGC 7009 has been well known for its unusually strong and rich OII optical permitted lines and they utilized the detailed and more accurate calculations made by Storey (1994) in their analysis. Previous analyses of this planetary nebula have used the effective radiative recombination rates of Péquignot *et al.* (1991), and the works' of Storey (1981) and Nussbaumer and Storey (1984) to give the dielectronic component of the total rate. A comparison of the combined rates mentioned here for CII and the new rates calculated in this thesis, is given in chapter 5. While the agreement is good for near hydrogenic lines, there are marked discrepancies for states with large quantum defects.

In chapter 6, the application of the CII recombination spectra is considered in two other distinct and physically different regimes, one of which has previously been mentioned. These are 'cold' nova shells, characterized by temperatures, perhaps as low as 500 K and densities as low as 10^2 cm^{-3}, and the cool stellar winds of Population II Wolf-Rayet carbon stars, where the density may range from 10^9 – 10^{13} cm^{-3} at temperatures of ~15000 K. These regions are described in more detail below.

1.3.1 Cold Nova Shells

The importance of recombination in old nova envelopes and some supernovae remnants has been noted by several authors, Williams (1982), Ferland *et al.* (1984), Martin (1988) and Smits (1991) for example. In these regions, it is necessary to calculate radiative coefficients down to very low temperatures since the intensity of recombination lines are not proportional to the intensity of, for instance, Hβ for widely varying values of T_e.

Another unusual feature in the spectra of the cool gas is the presence of heavy metal recombination lines with fluxes relative to the HI Balmer lines, much larger than normally found in nebulae. Although not uniformly distributed in the shells, lines of CII, NII and OII are identified in the spectra of DQ Her (Williams *et al.*, 1978) and NII, NIII and NIV in CP Pup (Williams, 1982). The implication of these large fluxes is that the CNO abundances are enhanced with respect to the other nebulae by large factors (Smits, 1991).

As has been noted the low electron temperature and densities of the nebula, mean that, the atomic data required to interpret the observations is mainly obtained by theoretical calculations, where understanding is followed by a large computational effort !

1.3.2 Wolf-Rayet Stars

The name Wolf-Rayet (WR) stars is in use for stars similar in optical appearance to the stars mentioned in the original paper of Wolf and Rayet (1867), which are now known to be massive, hot, luminous Population I stars. The name is also used for stars of planetary nebulae (Population II stars), which are objects of low mass and low luminosity. The stars at the centre of planetary nebulae, show the same emission line spectra that is characteristic of WR stars. Observational differences between the two WR populations have been discussed by Smith and Aller (1971) and by Méndez *et al.* (1991).

WR stars are classified as such, based on the appearance of emission lines in their spectra. A classification system based on such emission lines will not be closely coupled to the stellar parameters, of effective temperature and luminosity. There is a class of WR stars, known as WC stars, which show prominent Carbon emission lines. Though carbon lines will be observed in nearly all types of WR stars, they are particularly predominant in the WC class. Of particular interest are the late type WC stars, e.g. WC10, in which the level of ionisation is such as to allow the appearance of strong emission in CII lines. In order to accurately calculate the recombination spectra, full allowance must be taken of collisional processes, which at densities of 10^{13} cm^{-3} will dominate radiative rates down to low values of the principal quantum number. Theoretical comparisons will be made to an observed spectra of a WC10 star, which is one of the low mass, low luminosity Population II variety, at the heart of a planetary nebulae.

1.4 Re-evaluation of Carbon II Radiative Data

In general, but more fundamentally in a low temperature and density regime, the accurate evaluation of effective recombination rates is essential if any accuracy is to be attached to the analysis of observed spectra. This requires that special attention must be given to the evaluation of the rates for the processes of radiative and dielectronic recombination.

At high temperatures, dielectronic recombination proceeds via large numbers of doubly excited auto-ionising states with a high principle quantum number of the captured electron. At temperatures typical of planetary nebulae (10^4K) only the lowest of these states are accessible (Storey, 1981).

At very low temperatures, where the mean free electron energy is less that the energy E_0 of the lowest autoionizing state, relative to the first ionization threshold, the calculated recombination coefficient falls as $\exp(-E_0/kT_e)$ with decreasing temperature. To obtain reliable recombination coefficient at these low temperatures, typically in the range 500-5000 ^{0}K, it is necessary to obtain the recombination coefficients by integrating over the bound state photoionisation cross-sections. In this approach, autoionising states appear as resonances in the photoionisation cross-sections and effects such as the mean free electron energy being comparable to the resonance widths and the non-zero back ground cross-sections between resonances, are correctly treated. The omission of these effects would severely underestimate the recombination coefficient at very low temperature (Nussbaumer and Storey, 1983). At temperatures where kT_e is larger than the first ionisation energy, high temperature dielectronic recombination becomes important. This process is not fully accounted for in this work, so the applicable range of temperature is limited to less than 20000 ^{0}K.

Previously, recombination coefficients have been evaluated in general using hydrogenic approximations, scaled for the effective charge of the ion and where appropriate, have included the effects of dielectronic recombination, based on Storey (1981) and Nussbaumer and Storey (1984). Where detailed photoionisation calculations have been available these have been used, but there was a general lack of detailed photoionisation cross-sections for excited states. The Opacity Project has gone some way to remedy this, with calculations over a wide range of elements and ions.

The more satisfactory and exact approach is the one that makes no distinction between radiative and dielectronic recombination. Consider the radiative capture process

$$X_{n+} + e^- \longrightarrow X^*_{(n-1)+} + h\nu \tag{1.2}$$

The photoionisation cross-section for this process will in general, have the form of a smooth background interrupted by resonances. The resonances correspond to quasi-bound states of the recombined system $X^*_{(n-1)+}$, and Rydberg series of states, converging on the terms of the recombining system. The rate coefficient for radiative capture is obtained by integrating the photoionisation cross-section over the free electron velocity distribution. The resonances in the photoionisation cross-section correspond to the dielectronic component of the total recombination coefficient. The calculation of the total radiative recombination coefficient requires the integration of the photoionisation cross-section including resonances for all bound states of the ion. Storey (1994) employed this unified approach to determine recombination coefficients for OII using photoionisation cross-sections generated in the course of the Opacity Project. However in many cases treated by the Opacity Project, the free electron mesh on which the photoionisation cross-sections are calculated, was too coarse to accurately map narrow resonance features. This may lead to significant contributions to the recombination coefficient being missing, since the resonance contribution is proportional to the area underneath the resonance and not just the width. Broader resonances may also be truncated. Storey (1994) discusses this problem, but in the case of OII, the dielectronic resonance contributions are weak, otherwise recalculation of the cross-sections would have been needed. This was not the case for Carbon II. Poorly mapped resonances required that photoionisation cross-sections be recalculated for all states up to and including $n = 15$, $L = 4$ and a different method be used to ensure accurate mapping of resonances in the free state energy mesh. The unified approach suffers from a shortcoming in the theory whereby the cross-section in the vicinity of resonance whose autoionisation width is only comparable to the radiative width, overestimates the contribution to the recombination coefficient. In this work, the implicit assumption of thermodynamic equilibrium for autoionising states was checked and where found not to hold, the resonances were eliminated from the calculation of the photoionisation cross-section.

Various approximations have been used for radiative transition probabilities as well, with authors taking transitions from many sources using many approximations. For transitions where explicit calculations are not available, use is made of hydrogenic or coulomb rates which may sometimes be considerably in error. The original oscillator strengths for CII calculated during the Opacity Project have been recalculated here and extended. Great care has been taken to deduce accurate transition probabilities from highly excited states to lower ones. Hydrogenic or coulomb rates have only been used where it was appropriate to do so.

1.5 Summary

The aim of this thesis is to provide a full and accurate treatment of the recombination spectrum of Carbon II, making full allowance for all important physical processes and calculating where necessary new and more accurate rates. CII emission lines appear in a wide range of astrophysical regimes and the CII emission spectrum is very suited to the task of interpreting observational data.

As more and higher quality spectra become available covering a wide variety of objects and spectral regions, there is a need for the atomic data, a large amount of which is purely theoretical, to match the quality of the observations. This thesis sets out to provide accurate recombination coefficients for CII, not just for the ground or first excited state complexes, but also to a large number of excited states, where hydrogenic or coulomb approximations are not appropriate. Improved radiative transition probabilities are calculated and used, and tables of lines useful for identification purposes are given.

Chapter 2 describes the application of R-matrix theory to the solution of the close-coupling approximation. The chapter explains the determination of bound state-energy levels and the evaluation of photoionisation cross-sections using quantum defect theory. A summary of the Opacity Project codes is also given.

Chapter 3 details the application of the R-matrix theory to the generation of photoionisation cross-sections in the particular case of CII. The Opacity Project CIII target is described along with the determination of fundamental parameters of R-matrix theory. Calculated bound state energy levels are produced, as part of the generation of the photoionisation cross-sections and compared with experiment. The problem of autoionising states not in thermodynamic equilibrium, is also considered and the energy meshes used in the generation of the free state wave functions are explained. Finally some results of the photoionisation calculations are presented.

Chapter 4 details the evaluation of recombination coefficients from the photoionisation cross-sections. The resonances contributions, of the 2s2p3d $^2F^0$ and $^2P^0$ states, which lie just above threshold are carefully considered. The tabulation of the calculations is considered along with the generation of hydrogenic and coulomb cross-sections in the appropriate regions.

Chapter 5 explains the solution of the level population equations. It details all radiative and collisional rates not previously considered. The new radiative transition probabilities are examined. Hydrogenic and coulomb rates are also evaluated where necessary and appropriate, and the use of below threshold cross-section interpolation, to determine transition probabilities between high and low states is described. The various approximations to the collision rates are described and the formulation of the solutions of the level populations in terms of departure coefficients is given. The use of hydrogenic solutions to the level population equations as a first approximation is considered. The generation of effective recombination coefficients and effective fluxes is described and tables of wavelengths, and case A and case B effective recombination coefficients are given applicable to nebular temperatures and densities. Detailed comparison is made with published work.

Chapter 6 demonstrates the applications of recombination theory to the cold nova shell, DQ Her and the WC10 star, CPD -56^0 8032. Finally, a summary of the results, and a discussion of the shortcomings of this work and the possibility of future work are given.

Chapter 2

R-matrix Photoionisation Cross-sections

2.1 Introduction

The photoionisation process is characterized by the interaction of a photon and an atom, causing an electron to be excited from a ground or excited state to the continuum. Equation (2.1) describes this process.

$$X_a^{n+} + \omega \rightarrow X_f^{(n+1)+} + e^- \tag{2.1}$$

Let $\sigma_\omega(a \rightarrow f)$ be the cross-section for the process, then

$$\sigma_\omega(a \rightarrow f) = \frac{4\pi^2}{3} a_0^2 \alpha \frac{\omega}{g_a} \mathrm{S}(E, f; a) \tag{2.2}$$

where ω is the photon energy in Rydbergs and $\mathrm{S}(E, f; a)$, is a generalised line strength.

Various approximations exist for the evaluation of photoionisation cross-sections for complex ions. If the wave functions for the $X_f^{(n+1)+} + e^-$ system are evaluated by a method such as the close-coupling (CC) approximation, in which the interaction between open and closed channels is calculated, resonance effects are automatically included. The determination of accurate resonance structure is important for calculating recombination to low lying states particularly at low temperatures. The calculations in this thesis were based upon the codes used by the Opacity Project (OP) (Seaton, 1987). These evolved from the codes of Berrington *et al.* (1974, 1978) and used the R-matrix method, to solve the Schrödinger equation in the CC approximation of electron-atom collision theory.

2.2 The Close-Coupling Approximation

The basic expansion of the CC approximation can be written,

$$\Psi = \mathcal{A}\sum_{i} \chi_i \theta_i \tag{2.3}$$

where $\mathcal{A}$ is an antisymmetrisation operator. χ_i are functions of the 'N-electron' target and θ_i are orbital functions of the colliding electron. If ψ_i are functions which are vector coupled products, of functions representing the 'N-electron' core and functions representing the spin and angle coordinates of the added electron, then total wave function can be written,

$$\Psi = \mathcal{A}\sum_{i=1}^{I} \psi_i \frac{1}{r} F_i(r) + \sum_{j=1}^{J} \Phi_j D_j \tag{2.4}$$

For convenience, $F_i(r)$, the radial functions of the added electron, are taken to be orthogonal to radial functions for the core, ψ_i, having the same angular symmetry. Φ_j are functions of a bound-state type, which are included to compensate for the imposition of orthogonality conditions on $F_i(r)$. Additional functions can be included to improve accuracy. For complex atoms and ions it is more convenient to introduce additional pseudo-contracted orbitals with the same range as the Hartree-Fock orbitals for the target, and to construct additional correlation configurations from these.

Since (2.4) is truncated, Ψ is not a solution of the Schrödinger equation,

$$(H - E)\Psi = 0 \tag{2.5}$$

where H is the Hamiltonian for the whole system and E is the total energy. The equations used in CC theory can be derived from the variational condition,

$$(\delta\Psi | H - E | \Psi) = 0 \tag{2.6}$$

where $\delta\Psi$ is any variation in Ψ due to a variation in $F_i(r)$ or D_j. This gives rise to a set of integrodifferential equations to be satisfied by $F_i(r)$ and D_j.

The target functions χ_i are constructed using conventional configuration interaction (CI) wavefunctions, using a common set of radial functions, $P_{nl}(r)$. These radial functions are of two types. *Spectroscopic orbitals, nl* of the type which would occur in a central field model; and *correlation orbitals,* $\overline{n}l$, described above, included to improve accuracy. The radial functions are calculated using Slater-type orbitals given by,

$$P_{nl}(r) = \sum_{k} C_k r^{m_k} \exp(-\mu_k r) \tag{2.7}$$

Powers of r are related to the orbital quantum number, l, by $m_k \geq l + 1$. Hartree-Fock functions together with correlation orbitals are usually employed to provide initial estimates. The target Hamiltonian is then diagonalised in a CI representation and the parameters C_k and μ_k varied, subject to orthonormality constraints to minimise a specific eigenvalue or group of eigenvalues.

2.3 The R-matrix Solution to the Close-Coupling Approximation

The central feature of the R-matrix method, is the division of the configuration space of the colliding particles into two physically distinct regions. These are commonly described as the inner and outer regions.

The inner region contains the particles when they are close to the collision centre, so that the most mathematically complex part of the interaction is confined to a finite region of configuration space. The collision wave function can be expressed in terms of a discrete, complete, set of basis functions. The inner region is also known as the R-matrix box. In the outer region, the collision wave function has an asymptotic form and can be directly obtained from the asymptotic Schrödinger equation. Berrington *et al.* (1987), summarize the R-matrix method used in these calculations.

2.3.1 Solutions in the Inner Region

Solutions are first obtained for inner region functions, $\Psi = \psi_n$, which satisfy fixed boundary conditions at $r = a$. The value a, of the radial variable r, is chosen such that the functions χ_i and Φ_j are small, and exchange and correlation effects can be neglected, for $r \geq a$. Solutions exist for a discrete set of energies, $E = e_n$ and contain radial functions $F_i(r) = f_{in}(r)$. The normal boundary condition assumes that the derivatives of the radial functions are zero at $r = a$.

For any value of E, the complete wave function Ψ_E can be expanded as,

$$\Psi_E = \sum_n \psi_n A_{nE} \tag{2.8}$$

and it can be shown (Burke *et al.* 1971) that

$$A_{nE} = (e_n - E)^{-1} \sum_i f_{in}(a) F'_{iE}(a) \tag{2.9}$$

where $F'_{iE}(a)$ is taken to be such that Ψ_E satisfies the required normalization and boundary conditions. Hence,

$$F_{iE}(a) = \sum_{i'} R_{ii'}(E) F'_{iE}(a) \tag{2.10}$$

where

$$R_{ii'}(E) = \sum_{n} f_{in}(a)(e_n - E)^{-1} f'_{in}(a) \tag{2.11}$$

is referred to as the R-matrix.

The functions ψ_n are calculated in the following manner. First the radial functions $f_{in}(r)$ are expanded in terms of functions $u_{l_ik}(r)$, where $u_{lk}(r)$, the zero-order basis functions, are solutions of

$$\left(\frac{d^2}{dr^2} - \frac{l(l+1)}{r^2} - V(r) + \varepsilon_{lk}\right) u_{lk}(r) + \sum_{n} \lambda_{nlk} P_{nl}(r) = 0 \tag{2.12}$$

and satisfy the R-matrix boundary conditions,

$$\begin{aligned} u_{lk}(0) &= 0 \\ u'_{lk}(a) &= 0 \end{aligned} \tag{2.13}$$

u_{lk} are often called the continuum orbitals, as opposed to the bound state type orbitals, $P_{nl}(r)$, included in (2.12). $V(r)$ is a model potential and the λ_{nlk} are Lagrange multipliers introduced to orthogonalise the continuum orbitals to the bound state orbitals of the same angular symmetry.

The functions u_{lk} are then Schmidt orthogonalised to the correlation orbitals and used to construct functions,

$$\psi_{ik} = \mathcal{A}\chi_i(r_n^{-1}) \left(\frac{1}{r_n}\right) u_{l_ik}(r_n) \tag{2.14}$$

The functions ψ_n are expanded in terms of

$$\begin{aligned} &\psi_{ik} \quad \text{for} \quad i = 1 \text{ to } I \qquad \text{and} \quad k = 1 \text{ to } K \\ &\Phi_j \quad \text{for} \quad j = 1 \text{ to } J. \end{aligned}$$

The expansion coefficients are obtained on diagonalising the matrix of the Hamiltonian in the above representation.

Truncation of the expansion to include K functions, u_{lk}, k =1 to K, gives N functions, ψ_n, n =1 to N and a truncated R-matrix

$$R_{ii'}^{(N)} = \sum_{n=1}^{N} f_{in}(a)(e_n - E)^{-1} f_{i'n}(a) \tag{2.15}$$

A method for correcting the truncation is given by Buttle (1967). These involve corrections, in the first instance, to the diagonal terms of the R-matrix. Truncation of (2.8), using (2.9) gives,

$$\Psi_E^{(N)} = \sum_{n=1}^{N} \psi_n (e_n - E)^{-1} \sum_{i}^{I} f_{in}(a) F'_{iE}(a) \tag{2.16}$$

putting

$$\Psi_E = \Psi_E^{(N)} + \Delta\Psi_E \tag{2.17}$$

where

$$\Delta\Psi_E = \sum_i \Delta\psi_i \times F'_{eE}(a) \tag{2.18}$$

and from (2.14)

$$\Delta\psi_i = \mathcal{A}\chi_i(r_n^{-1})(\frac{1}{r_n})\Delta u_{l_i,\epsilon_i}(r_n) \tag{2.19}$$

the complete expansion including Buttle correction can be written:

$$\Psi_E = \sum_{n=1}^{N} \psi_n A_{nE} + \sum_{i=1}^{I} \Delta\psi_i F'_{iE}(a) \tag{2.20}$$

The R-matrix method gives functions Ψ_E for the inner region $r \leq a$, which are bounded at the origin and which contain radial functions $F(r)$ at $r = a$. Solutions are required for the outer region, $r \geq a$, which tend to zero for $r \to \infty$ and which are matched to the inner region solutions, at $r = a$.

2.3.2 Solutions in the Outer Region

For each value of the energy, there are a set of linearly independent outer-region functions, $\Psi_{i'}$. For $r \geq a$, these functions have expansions

$$\Psi_{i'} = \mathcal{A} \sum_i \psi_i \frac{1}{r} F_{i'}(r) \tag{2.21}$$

where $F_{i'}$ are radial functions of the outer electron such that $F_{i'} \to 0$ for $r \to \infty$.

In the outer region the integro-differential equations reduce to ordinary differential equations,

$$\left(\frac{d^2}{dr^2} - \frac{l_i(l_i+1)}{r^2} + \frac{2Z}{r} + \epsilon_i \right) F_i(r) - \sum_{i'} V_{ii'}(r) F_{i'}(r) = 0 \tag{2.22}$$

where $V_{ii'}(r)$ are long range multipole potentials of the form,

$$V_{ii'}(r) = \sum_{\lambda} \frac{C_{ii'}^{(\lambda)}}{r^{\lambda+1}} \tag{2.23}$$

In the outer region, it is taken that the functions χ_i are small and this is in general a good assumption. It can be shown (Seaton, 1985) that

$$|V_{ii'}(r)| \ll \frac{2Z}{r} \qquad for \quad r \geq a \tag{2.24}$$

and hence multipole potentials can be regarded as small perturbations and subsequently neglected. With this assumption, the solutions of (2.22) reduce to Coulomb functions.

Let E_i be the energy of the target state i and ε_i, the energy of the added electron. Then the total energy E, is given by

$$E = E_i + \varepsilon_i \tag{2.25}$$

$\varepsilon_i < 0$ corresponds to bound states for all i and the radial functions $F_i(r)$ go to zero exponentially in the limit of $r \rightarrow \infty$. The collisional states are such that $\varepsilon_i > 0$ for some values of i. A channel i is said to be *open* if $\varepsilon_i > 0$ and *closed* if $\varepsilon_i < 0$. Let the E_i be ordered such that $E_1 < E_2 < ... E_i$. For a given E there are I_0 open channels,

$$\begin{aligned} \varepsilon_i &> 0 \quad for\ i = 1\ to\ I_0 \\ \varepsilon_i &< 0 \quad for\ i = (I_0 + 1)\ to\ I \end{aligned} \tag{2.26}$$

$F_{ii'}$ are defined to be radial functions satisfying the reactance matrix boundary conditions,

$$\begin{aligned} F_{ii'} &\overset{r \rightarrow \infty}{\sim} s_i(r)\delta(i,i') + c_i(r)K(i,i') \quad for\ i = 1\ to\ I_0 \\ F_{ii'} &\overset{r \rightarrow 0}{\sim} 0\ for\ i = (I_0 + 1)\ to\ I \end{aligned} \tag{2.27}$$

with $i' = 1$ to I_0. The functions $s_i(r)$ and $c_i(r)$ are the Coulomb functions with asymptotic forms, given by Seaton (1983),

$$\begin{aligned} s(\varepsilon, l; r) &\sim (\pi k)^{-\frac{1}{2}} sin(\xi) \\ c(\varepsilon, l; r) &\sim (\pi k)^{-\frac{1}{2}} cos(\xi) \end{aligned} \tag{2.28}$$

where

$$\xi = kr - \frac{1}{2}l\pi + \frac{Z}{k}\ln(2kr) + \arg\left[\Gamma(l + 1 - \frac{iZ}{k})\right] \tag{2.29}$$

and where Z is the charge on the target system. The Coulomb functions $\phi^{\pm}(r)$ are defined by

$$\phi^{\pm}(r) = c \pm is \tag{2.30}$$

and have the asymptotic form

$$\phi^{\pm}(r) \sim (\pi k)^{-\frac{1}{2}} e^{\pm i\xi} \tag{2.31}$$

The S-matrix is defined by the following boundary conditions

$$\begin{aligned} F_{ii'} &\overset{r\to\infty}{\sim} r^{l_i+1} \\ F^-_{ii'} &\sim \frac{1}{2}\{\phi_i^-(r)\delta(i,i') - \phi_i^+(r)S(i,i')\} \qquad for\ i = 1\ to\ I_0 \\ F^-_{ii'} &\sim 0 \quad for\ i = (I_0+1)\ to\ I \end{aligned} \tag{2.32}$$

Comparing (2.27) and (2.32) the two $n_{I_0} \times n_{I_0}$ matrices, $S_{ii'}$ and $K_{ii'}$ are related by the matrix equation,

$$\mathbf{S} = \frac{(1+i\mathbf{K})}{(1-i\mathbf{K})} \tag{2.33}$$

and that

$$\mathbf{F}^- = -\mathbf{F}(1-i\mathbf{K})^{-1} \tag{2.34}$$

where the $\mathbf{F}(r)$ are functions with K-matrix asymptotic forms. The functions $\mathbf{F}^+(r)$, representing final state radial functions used in the photoionisation calculations, are the complex conjugates of the functions $\mathbf{F}^-(r)$.

$$\mathbf{F}^+(r) = \mathbf{F}^{-*}(r) \tag{2.35}$$

The radial functions, $\mathbf{F}^\pm$ give functions $\Psi^\pm$ satisfying

$$(\Psi^\pm(E)|\Psi^\pm(E')) = \delta(E-E') \tag{2.36}$$

with E and E' in Rydbergs.

2.3.3 Matching Solutions at the Boundary

All equations are matched at $r = a$. Equation (2.10) can be written

$$\mathbf{F} = \mathbf{R}\mathbf{F}' \tag{2.37}$$

When all channels are open this gives,

$$\mathbf{F} = \mathbf{S} + \mathbf{C}\mathbf{K} \tag{2.38}$$

and substitution in (2.37) leads to

$$\mathbf{K} = -(\mathbf{C} - \mathbf{R}\mathbf{C}')^{-1}(\mathbf{S} - \mathbf{R}\mathbf{S}') \tag{2.39}$$

When some channels are open and some closed, a square matrix of outer region functions can be defined,

$$\overline{\mathbf{C}} = \begin{pmatrix} \mathbf{C}_{\mathbf{oo}} & \Theta_{\mathbf{oc}} \\ \mathbf{C}_{\mathbf{co}} & \Theta_{\mathbf{cc}} \end{pmatrix} \tag{2.40}$$

containing i rows and I columns, and a rectangular matrix

$$\overline{\mathbf{K}} = \begin{pmatrix} \mathbf{K}_{\mathrm{oo}} \\ \mathbf{K}_{\mathrm{co}} \end{pmatrix} \tag{2.41}$$

containing I rows and I_0 columns. In (2.41), $\mathbf{K}_{\mathrm{oo}}$ is a square matrix defined in §2.3.2, containing I_0, rows and columns. The matrix $\overline{\mathbf{K}}$ is such that the outer region functions are,

$$\mathbf{F} = \mathbf{S} + \overline{\mathbf{C}}\overline{\mathbf{K}} \tag{2.42}$$

and substitution into (2.37) gives

$$\overline{\mathbf{K}} = -(\overline{\mathbf{C}} - \mathbf{R}\overline{\mathbf{C}})^{-1}(\mathbf{S} - \mathbf{R}\mathbf{S}') \tag{2.43}$$

Once the matrix $\overline{\mathbf{K}}$ has been calculated, the derivatives of the functions $F'(a)$ can be calculated and hence the coefficients A, in (2.9).

2.4 Bound States

The use of the R-matrix method in the determination of bound state energy levels is detailed by Seaton (1985). A column vector of functions $\mathbf{F}(r)$ can be constructed for $r \leq a$ which satisfy

$$\mathbf{F} = \mathbf{R}(\mathbf{F}' - \beta\mathbf{F}) \tag{2.44}$$

where $\mathbf{R}$ is the matrix of elements $R_{ii'}(E)$ and β is a constant. A square matrix of functions $\mathbf{P}(r)$ for $r \geq a$ can be constructed. All functions of r are taken to be matched at $r = a$.

The condition for matching is

$$\mathbf{F} = \mathbf{P}\mathbf{X} \tag{2.45}$$

$$\mathbf{F}' = \mathbf{P}'\mathbf{X} \tag{2.46}$$

where $\mathbf{X}$ is a column vector. Substituting (2.45) and (2.46) into (2.44) gives

$$\mathbf{P}\mathbf{X} = \mathbf{R}(\mathbf{P}' - \beta\mathbf{P})\mathbf{X} \tag{2.47}$$

Let the function $\mathbf{Q}$ be defined such that for $r \geq a$,

$$\mathbf{Q} = \mathbf{P}' - \beta\mathbf{P} \tag{2.48}$$

Then from (2.47) the following is obtained.

$$(\mathbf{P} - \mathbf{R}\mathbf{Q})\mathbf{X} = 0 \tag{2.49}$$

This equation can be considered to be a standard form for the matching condition. From this a general form is taken to be,

$$\mathbf{B}(E)\mathbf{X} = 0 \tag{2.50}$$

Equations of this form have solutions only at certain discrete values of E, corresponding to the bound-state energy eigenvalues. These energy eigenvalues can be located by a systematic search for zeros of the determinant of $\mathbf{B}(E)$.

$$\det\,[\mathbf{B}(E)] = 0 \tag{2.51}$$

Given an initial estimate, E_0 of an eigenvalue, (2.50) can be solved using successive linearisations. Putting,

$$\mathbf{B}(E) = \mathbf{B}(E_0) + (E - E_o)\dot{\mathbf{B}}(E) \tag{2.52}$$

the standard eigenvalue problem

$$\mathbf{BX} = x\mathbf{DX} \tag{2.53}$$

with $\mathbf{B} = \mathbf{B}(E_0)$, $\mathbf{D} = -\dot{\mathbf{B}}(E_0)$ and $x = (E - E_0)$, is obtained. Then $E = E_1 = E_0 + x$ is taken to be an improved estimate of the eigenvalue obtained from solving (2.52). The linearisation procedure is repeated, taking $E_0 = E_1$ and continuing until x is sufficiently small. The form, (2.49), of the matching condition corresponds to taking

$$\mathbf{B}(E) = \mathbf{P}(E) - \mathbf{R}(E)\mathbf{Q}(E) \tag{2.54}$$

This form has a disadvantage in that the matrix $\mathbf{B}(E)$ will have poles at the R-matrix poles, $E = e_n$ (see 2.9). A method of solving this problem of energy eigenvalues corresponding to R-matrix poles and the method for obtaining the smallest eigenvalue x, above, is given in the appendices of Seaton (1985).

2.5 Photoionisation Cross-sections

Equation (2.2) gives the formula for the cross-section, σ_ω for the process (2.1). The generalised line strength, in atomic units, is

$$S(E, f; a) = \sum_L |D^+_{fa}(E, SL\pi; a)|^2 \tag{2.55}$$

where SLπ specifies the spin, orbital angular momentum and parity of the final state and D^+_{fa} is the dipole matrix element. The initial and final states have the same spin and opposite parities. Yu Yan and Seaton (1987) detail the calculation of atomic photoionisation cross-sections using CII as an example.

2.5.1 Final State Radial Wave Functions

The dipole matrix element, D^+_{fa}, is calculated using the final-state radial wave functions, $F^+_{if}(r)$, given by (2.34) and (2.35). If I is the total number of channels included in the CC expansion, then i is the channel index, $i = 1$ to I. The total energy E, is given by

$$E = E_i + \varepsilon_i \tag{2.56}$$

where E_i is the energy of the target state X_i^+, for channel i, and ε_i is the energy of the added electron. Similarly to (2.26), open channels have $\varepsilon_i \geq 0$ and closed channels have $\varepsilon_i < 0$. Let there be I_0 open channels. Then

$$\begin{aligned} i &= 1 \;\; to \;\; I_0 \quad \text{for open channels} \\ i &= (I_0 + 1) \;\; to \;\; I \quad \text{for closed channels} \\ f &= 1 \;\; to \;\; I_0 \end{aligned} \tag{2.57}$$

The matrix $\mathbf{F}^+(r)$, with elements $F^+_{if}(r)$, is partitioned into open-open and closed-open submatrices.

$$\mathbf{F} = \begin{pmatrix} \mathbf{F}^+_{\mathrm{oo}} \\ \mathbf{F}^+_{\mathrm{co}} \end{pmatrix} \tag{2.58}$$

$\mathbf{F}^+_{\mathrm{oo}}(r)$ and $\mathbf{F}^+_{\mathrm{co}}(r)$ are the complex conjugates of the asymptotic forms given in (2.34). The numerical calculations are made with real functions $\mathbf{F}(\mathbf{K}|r)$ with K-matrix normalization (2.27). It follows that

$$\mathbf{F}^+ = i\mathbf{F}(\mathbf{K})(1 + i\mathbf{K})^{-1} \tag{2.59}$$

The expansions for the wave functions involve summations over the channel indices i, and, for a given initial state, a, the dipole matrix elements depend only on the index f. Let $\mathbf{D}^+$ and $\mathbf{D}(\mathbf{K})$ be the column vectors, with elements D^+_{fa} and $D_{fa}(\mathbf{K})$, calculated using the functions $\mathbf{F}^+$ and $\mathbf{F}(\mathbf{K})$. They are related by

$$\mathbf{D}^+ = -i(1 - i\mathbf{K})^{-1}\mathbf{D}(\mathbf{K}) \tag{2.60}$$

The resonance structure is obtained using quantum defect theory and is described below.

2.5.2 Application of Quantum Defect Theory to Resonances

The behaviour of the scattering matrix, as a function of energy is given by Seaton (1983).

$$\mathbf{S} = \chi_{\mathrm{oo}} - \chi_{\mathrm{oc}}[\chi_{\mathrm{cc}} - \exp(-2\pi i\nu)]^{-1}\chi_{\mathrm{co}} \tag{2.61}$$

It is assumed that χ varies slowly with energy and that all rapid variations in **S**, as a function of energy are due to variation of $\exp(-2\pi i\nu)$ in (2.61).

Resonances are due to poles in S and occur at complex energies $\mathcal{E}$(pole) which are such that

$$\det\left[\chi_{\mathrm{cc}} - \exp(-2\pi i\nu)\right] = 0 \tag{2.62}$$

When all channels are closed this expression is equivalent to the search in (2.51) for bound states.

The matrix χ contains functions pertaining to both open and closed channels. It has dimensions, $I \times I$, compared to S which has dimensions $I_0 \times I_0$, where I_0 is the number of open channels and $I_0 < I$ if some channels are closed. In the case of all channels open, $\mathbf{S} = \chi$. **S** can be thought of as a contraction of χ. This contraction is done over several stages.

Firstly, χ is partitioned into two groups of channels. A lower group (a) which may be open or closed and an upper group (b) which are all closed.

$$\chi = \begin{pmatrix} \chi_{aa} & \chi_{ab} \\ \chi_{ba} & \chi_{bb} \end{pmatrix} \tag{2.63}$$

Subsequently a contracted matrix is defined,

$$\chi(\mathrm{contr}) = \chi_{aa} - \chi_{ab}[\chi_{bb} - \exp(-2\pi i\nu_b)]^{-1}\chi_{ba} \tag{2.64}$$

If all channels in a are open then $\mathbf{S} = \chi(\mathrm{contr})$. If some of the channels in a are closed then $\chi(\mathrm{contr})$ is partitioned so as to obtain

$$\mathbf{S} = \chi_{\mathrm{co}}(\mathrm{contr}) - \chi_{\mathrm{oc}}(\mathrm{contr})[\chi_{\mathrm{cc}}(\mathrm{contr}) - \exp(-2\pi i\nu_c)]^{-1}\chi_{\mathrm{co}}(\mathrm{contr}) \tag{2.65}$$

where ν_c is a matrix of effective quantum numbers for the closed channels in group a. **S** will have rapid variations due to ν_c in (2.65) and slower variations due to ν_b in (2.64).

Consider the region below a new threshold. It is assumed that higher thresholds have been eliminated by using a contracted χ matrix and that all closed channels belong to the new threshold. χ_{cc} can be diagonalised,

$$\chi_{\mathrm{co}}\mathbf{X} = \mathbf{X}\chi_{\mathrm{cc}}' \tag{2.66}$$

with χ_{cc}' diagonal, and putting $\chi_{\mathrm{cc}}' = \exp(2\pi i\mu_c)$, where μ_c is the *complex quantum defect* given by,

$$\mu_c = \alpha_c + i\beta_c \tag{2.67}$$

with α_c and β_c real.

Since χ'_{cc} is symmetric, $\mathbf{X}$ in (2.66) can be normalised to $\mathbf{X}^{\mathbf{T}}\mathbf{X} = 1$. This leads to

$$[\chi_{cc} - \exp(-2\pi i\nu)] = \mathbf{X}[\chi'_{cc} - \exp(-2\pi i\nu)]\mathbf{X}^{\mathbf{T}} \tag{2.68}$$

Defining $\chi'_{oc} = \chi_{oc}\mathbf{X}$ and $\chi'_{co} = \mathbf{X}^{\mathbf{T}}\chi_{co}$ gives

$$\mathbf{S} = \chi_{oo} - \chi'_{oo}[\chi'_{cc} - \exp(-2\pi i\nu)]^{-1}\chi'_{co} \tag{2.69}$$

or

$$S_{ij} = \chi_{ij} \sum_p \frac{\chi'_{ip}\chi'_{pi}}{\exp(2\pi i\mu_p) - \exp(-2\pi i\nu)} \tag{2.70}$$

where i and j are open channels and p is summed over the degenerate closed channels.

In practice, χ_{cc} is diagonalised, giving rise to complex quantum numbers ν_p described previously. $\nu_p = \ln\chi'_{cc}$. Using $\nu_p = n - \mu_p$ then for closed channels belong to a core with energy $\mathcal{E}_c$, then the energy of the pole is $\mathcal{E}(\text{pole}) = \mathcal{E}_c - [\nu(\text{pole})]^{-2}$. Putting $\mu_p = \alpha_p + i\beta_p$ and dropping subscripts p,

$$\mathcal{E}(\text{pole}) = \mathcal{E}_c - \frac{[(n-\alpha)^2 - \beta^2] + i[2(n-\alpha)\beta]}{[(n-\alpha)^2 + \beta^2]^2} \tag{2.71}$$

and hence for $(n - \alpha) \gg \beta$,

$$\mathcal{E}(\text{pole}) \simeq \mathcal{E}_c - \frac{1}{(n-\alpha)^2} - \frac{i}{2}\gamma \tag{2.72}$$

where $\gamma = 4\beta(n-\alpha)^{-3}$, is the autoionisation width. Care must be taken in interpreting γ as a width, since in a Rydberg series, the widths cannot be larger than the separations.

2.5.3 The Gailitis Average

In all practical applications, cross-sections averaged over some distribution $f(v)$ of electron velocities are required. In the region just below a threshold, the variation in the cross-section due to an infinite series of resonances will be more rapid than the variation in $f(v)$. For $\nu \geq \nu_{max}$ one can calculate cross-sections averaged over the resonances in series converging on the next threshold. For a photon energy ω_0, corresponding to some effective quantum number $\nu = \nu_0$, the averaged cross-section is defined by Gailitis (1963).

$$< \sigma_{\omega_0} >= \int_{\nu_0 - \frac{1}{2}}^{\nu_0 + \frac{1}{2}} \sigma_\omega \; d\nu \tag{2.73}$$

It follows that the averaged total cross-section below threshold, joins smoothly onto σ_ω above.

2.6 A Summary of the Opacity Project Suite of Codes

The Opacity Project codes based on the R-matrix theory, as described, were adapted from the codes of Berrington *et al.* (1974,1978). The codes break down into sequential modules and were written in such a way that once the solutions to the inner region and the Hamiltonian have been calculated, there is no need to run them again for solving the outer region processes, since all the necessary datasets are archived. A brief summary of the codes is given here, and figure (2.6.4) illustrates the order in which the codes are run, and the datasets produced.

2.6.1 STG1

STG1 reads radial functions for the target, calculates the solutions $u_{lk}(r)$ of (2.12) and evaluates all necessary radial integrals.

2.6.2 STG2

STG2 calculates all the necessary angular algebra. It read the radial integrals generated by STG1 and evaluates matrices of the Hamiltonian and dipole operators, in the representation of the states.

2.6.3 STGH

STGH diagonalises the Hamiltonian matrix and produces datasets **H** and $\mathbf{D}_i$. Dataset **H** contains the basic R-matrix data, the energies, e_n and the surface amplitudes, $f_{in}(a)$. Dataset $\mathbf{D}_i$, contains the dipole matrices $D(n, n')$. STGH writes an index file **D00** and then one file for each $SL\pi$ combination.

2.6.4 STGB

The methods of STGB are discussed in §2.4. STGB reads the **H** dataset and calculates bound states energies. It again, produces an individual dataset, **B**, which holds the energy and effective quantum numbers for each $SL\pi$, in the effective quantum number range specified. This dataset is required in bound-bound (oscillator strengths) and bound-free (photoionisation) radiative calculations.

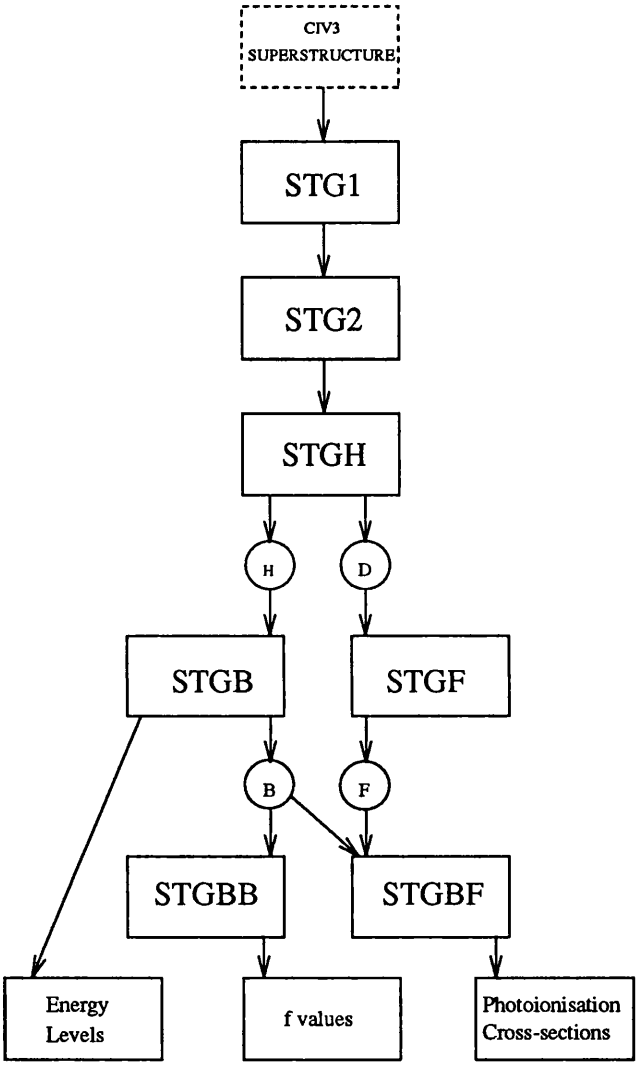

Figure 2.1: The Opacity Project suite of programs, used to generate atomic data for this thesis. CIV3 (Hibbert 1975) and SUPERSTRUCTURE (Eissner *et al.* 1974, Nussbaumer & Storey 1978) are not part of the suite, but are two programs that can be used to provide a target for STG1.

2.6.5 STGF

STGF reads the **H** dataset. From this it produces **F** datasets, detailed in sections §2.3.2 and §2.5, which contain the information on the final states, used in the calculation of the photoionisation cross-section in STGBF.

2.6.6 STGBF

STGBF reads the **B**, **D** and **F** datasets and calculates photoionisation cross-sections. It has options to calculate a total cross-sections to all final states, or partial cross-sections to all available channels. Use was made of both of these options where appropriate. A fuller description of STGBF is given by Yu Yan (1986).

2.6.7 STGBB

STGBB reads the B and D datasets and calculates oscillator strengths for bound-bound transitions.

2.7 Conclusions

The CC approximation provides a powerful technique for solving the interaction between an electron and a (N-electron) target. It can be used to obtain wave functions for bound states of the entire (N+1)-electron system and hence to determine bound state energy levels, and to evaluate oscillator strengths and photoionisation cross-sections.

The R-matrix method provides an accurate way of solving the CC approximation. It is also efficient, since the inner region Hamiltonian has only to be diagonalised once. Solutions can then be obtained by the running the outer region codes over the required energy range.

Chapter 3

R-matrix Photoionisation Cross-Sections for Carbon II

3.1 Introduction

The previous chapter, explained the R-matrix method for calculating photoionisation cross-sections. This chapter details the application of the theory, to the calculation of cross-sections for CII, and gives new energy levels of states calculated in the process.

Photoionisation cross-sections for CII were generated in the course of the OP (Yu Yan and Seaton, 1987). It was the original intention to use these cross-sections in the calculation of recombination coefficients. On inspection, however, the OP cross-sections showed little resolution in some of the resonance structures. The OP cross-sections were based on a quantum defect mesh which placed 100 points between each integer quantum number relative to the next threshold. This generated cross-sections of sufficient accuracy and resolution for the purposes of the OP, where the main focus was opacity but they were not good enough for the accurate calculation of recombination coefficients. These can only be generated from photoionisation cross-sections with well resolved resonance structures, for which the quantum defect mesh, was not sufficiently accurate. Figure (3.1) illustrates the difference in resolution between an OP cross-section and one subsequently calculated in this project. In the OP cross-section, the resonance labeled (A), at 1.135 Ryd consists only of 3 points. The peak height of the resonance was subsequently calculated to be ~20000 Mb. Figure (3.2), shows the difference in area under the two cross-sections, which is a more important indicator of their accuracy. In some cases the lack of accurate resonance structure would not preclude the use of the OP photoionisation cross-sections

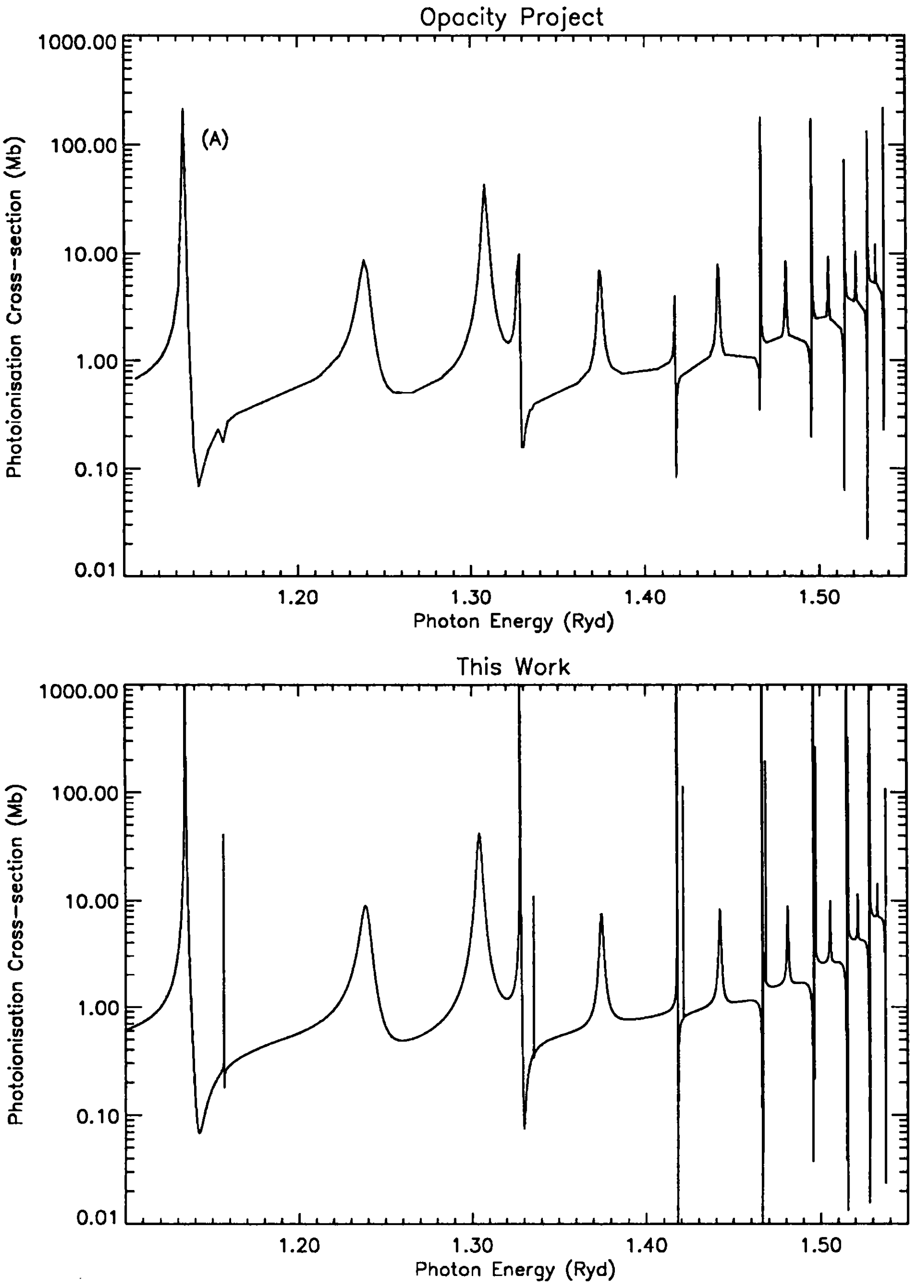

Figure 3.1: Comparison of the photoionisation cross-section for $2s2p^2$ ^2D, calculated by the OP (top) and this work (bottom). The OP cross-section consists of 199 points, based on a quantum defect mesh, whilst the latter is based on an energy mesh of 3281 points.

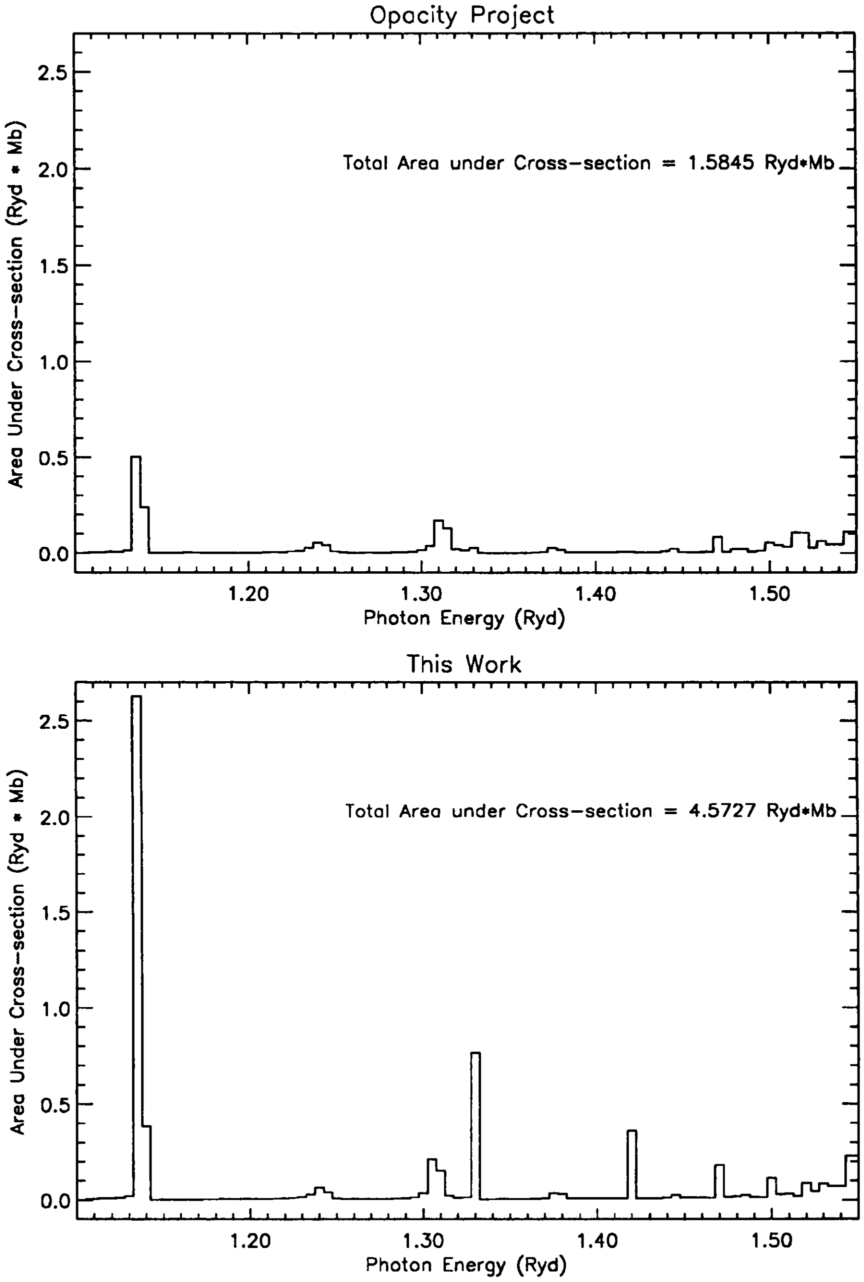

Figure 3.2: Comparison of the area under the $2s2p^2\ ^2D$ cross-section. The figure clearly illustrates, that using the OP cross-sections would significantly underestimate the recombination to the state, particularly at low temperatures, where much of the recombination is due to the first resonance.

in determining recombination coefficients. Storey (1994) used OP OII cross-sections in his calculation of recombination coefficients at nebula temperatures. The use of OP cross-sections was acceptable since the dielectronic component would have been very small. This is not the case for CII. At low temperatures, resonance (A), would provide the major contribution to the total recombination to the state, so it is vitally important that it is accurately mapped. It was initially because of the lack or resolution in the cross-sections that a decision was made to recalculate them. The differences in area under the OP cross-sections and ones subsequently calculated only served to confirm the correct nature of the decision. Cross-sections for photoionisation from all doublet states of CII having a principle quantum number $n \leq 15$ and total orbital angular momenta $L \leq 4$ (a total of 68 states) were calculated, using the methods described in the previous chapter.

3.2 The Carbon III Target

The photoionisation of CII is considered in terms of a ($C^{2+} + e^-$) problem. The starting point for the calculations, is the C III target. In these photoionisation calculations, and also the Opacity Project calculations (Yu Yan and Seaton, 1978), the CIII target calculated by Berrington *et al.* (1977) was used. The following target states were included in the calculation.

Table 3.1: The Carbon III Target States

Configuration	Term
$2s^2$	^1S
2s2p	$^3P^0$
	$^1P^0$
$2p^2$	^3P
	^1D
	^1S

All of these were represented as CI expansions in terms of seven, orthogonal basis orbitals and pseudo orbitals: 1s, 2s, 2p, $\overline{3s}$, $\overline{3p}$,$\overline{3d}$ and $\overline{4f}$. The six target eigenstates are represented as a linear sum of all possible configurations formed from these orbitals. This representation gives calculated energy level separations from the ground state, that agree to within 1.5% of the experimental CIII energy level values tabulated by Moore (1970).

3.3 Inner Region Codes

STG1 is the first program in the suite of codes to be run. This reads the target wavefunctions described in the previous section and evaluates all the radial integrals needed in the calculations. STG1 calculates the ground state energy of the target, and the separations of the various excitation thresholds, from the ground state. It was decided, in order to minimise errors, to use the experimental differences for the excited thresholds, instead of those calculated in STG1. These formed part of the input to STG2. The experimental values were obtained from Moore (1970).

3.4 Inner Region Parameters

STG2 is the second program of the inner region suite to be run and it is at this point that two fundamental parameters need to be defined. These are the size of the *R*-matrix box and the number of basis functions. These are represented by RA and NRANG2, respectively, in the notation of the codes. Two methods were used to test various values of these parameters. For RA, the values were tested by running the inner region codes and then running STGB, STGF and STGBF to obtain photoionisation cross-sections. The effect of altering RA was examined by looking at variations in resonance positions. NRANG2 was tested, by again running the inner region codes and then by running STGB and looking at bound state energy levels. In practice, these two tests cannot be performed independently since increasing the size of RA demands an increase in NRANG2 in order to achieve the same accuracy. The need for testing, arose partly from concern about the placement in energy of the resonances in the OP cross-sections, and from the realization that the OP set out to generate data uniformly across many ions and that not necessarily the best solution was used for individual ions.

RA determines how much of the bound state wave functions are in the inner region. An examination was made of the $2s2p^2\ {}^2D \rightarrow {}^2F^0$ partial cross-section. A large number of basis functions were used to ensure the accuracy of test. By observing the variation in energy of the resonance positions, as a function of RA, the accuracy of the boundary assumptions §2.3.1 in terms of the convergence of the resonance positions, could be gauged. The energies of various resonances showed no better convergence for RA > 10, so this was the value that was adopted.

The number of basis functions to be used was inferred from examining the bound state energies of the $2s^2 5s$ and $2s^2 6s$ states. These were chosen because the target wave functions contain almost no (N+1) electron wave function contribution. The electron wave function is solely dependent on NRANG2. The testing of various values of NRANG2, threw up an anomaly whereby very small values of NRANG2 would give lower bound state energies. This led to the investigation of the effect of adding the Buttle correction. The calculations, without the Buttle correction added, are variational in nature, implying that adding more basis functions would lower the bound state energies. However the Buttle correction is perturbative and adding it to the *R*-matrix diagonal terms changes the variational nature of the calculation.

As Figure (3.4) illustrates, the uncorrected calculation is variational. The Buttle corrected energies are plotted on the same scale for comparison. The effect of adding the Buttle correction is shown in detail at the bottom. The figure illustrates that at low values of NRANG2, the Buttle correction is overestimated, giving lower energies than can be achieved with larger values of NRANG2. The results with the Buttle correction added, converge much more quickly than a purely variational case and have a much smaller spread of energies. It should be noted however that the convergence may not be necessarily to the purely variational result. Care must be taken to check that the result obtained is 'close' to what might be expected in a variational case and that not too few basis functions are used.

There is also a marked contrast between the energies of bound states for odd and even values of NRANG2. This is again illustrated by Figure (3.4). These results dictated that an odd number of basis functions was appropriate. An extra consideration when deciding the number of basis functions to use is the amount of extra computing time that increasing the values requires. A value of NRANG2=15, was chosen as being the value beyond which the increase of accuracy was not sufficient to justify the extra computational time.

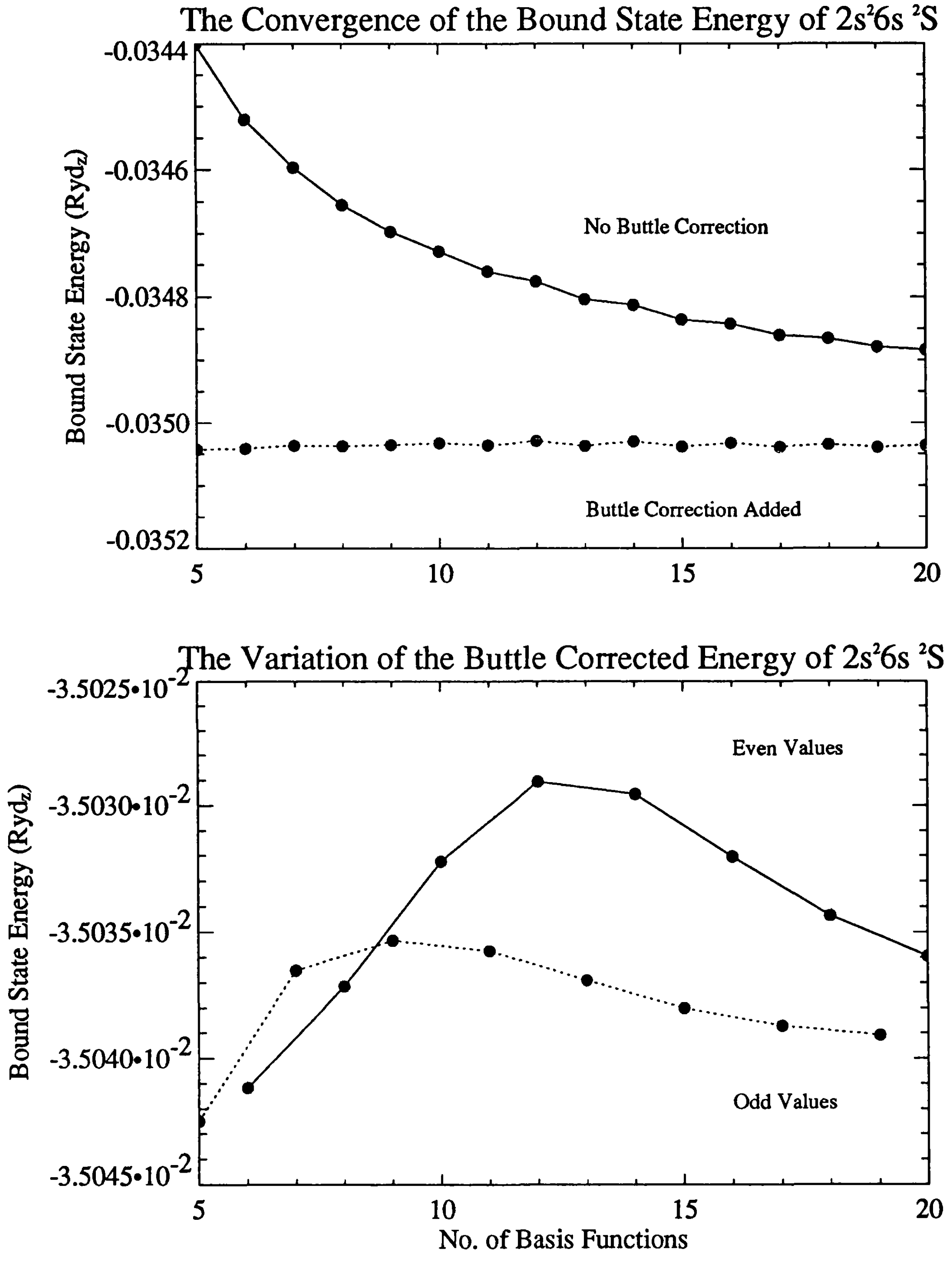

Figure 3.3: Comparison of the variation of bound state energy of $2s^26s$ with the number of basis functions

3.5 Calculated Bound State Energy Levels

In the process of calculating photoionisation cross-sections the energy levels of all the bound states in the problem were determined. Firstly, a fast scan is made for the roots of **det** [**B**] = 0 (2.51), to obtain first approximations to the eigenvalues, E_0. The determinant is calculated for energies that lie between the effective quantum number range supplied to the program. The step in effective quantum number, $\delta\nu$, is taken to be such that it is unlikely that more than one bound state will be found in any interval, $\nu_i < \nu < \nu_i + \delta\nu$. The codes were run with a $\delta\nu$ of 0.01. The initial values for bound state energies are calculated and written to a file. They are read back in and used as estimates in the eigenvalue equation. An improved value is then obtained by iteration. The iteration process was taken to be complete when $\Delta E < 10^{-4}$ Ryd. As well as energy levels, effective quantum numbers for the states are produced. These were used to aid the identification of the bound-states. They also gave a strong indication of how some of the states were perturbed. This information, along with a comparison with experimental energy level values, where available, is given in tables (3.2) to (3.8).

The final energy level files produced were saved and used not only in photoionisation calculations but also to provide the basis for indexing in the level population code.

Table 3.2: ^{2}S Bound State Energies

Configuration	Effective Quantum No.	Calculated Energy Relative To Threshold (Ryd)	Experimental Energy Relative To Threshold (Ryd)
$2s2p^2$	2.10925	-8.99095E-01	-9.12867E-01
$2s^23s$	2.34768	-7.25740E-01	-7.30205E-01
$2s^24s$	3.34038	-3.58483E-01	-3.59335E-01
$2s^25s$	4.34233	-2.12136E-01	-2.12489E-01
$2s^26s$	5.34232	-1.40152E-01	-1.40346E-01
$2s^27s$	6.34097	-9.94829E-02	-9.96223E-02
$2s^28s$	7.33832	-7.42790E-02	.....
$2s^29s$	8.33388	-5.75924E-02	.....
$2s^210s$	9.32621	-4.59885E-02	.....
$2s^211s$	10.31122	-3.76218E-02	.....
$2s^212s$	11.27287	-3.14768E-02	.....
2s2p3p	12.11123	-2.72699E-02	.....
$2s^213s$	12.66909	-2.49212E-02	.....
$2s^214s$	13.46059	-2.20766E-02	.....
$2s^215s$	14.41381	-1.92532E-02	.....

Table 3.3: ^{2}P Bound State Energies

Configuration	Effective Quantum No.	Calculated Energy Relative To Threshold (Ryd)	Experimental Energy Relative To Threshold (Ryd)
$2s2p^2$	1.79284	-7.67228E-01	-7.83844E-01
$2s2p3p$	2.56407	-1.31191E-01	-1.33305E-01

Table 3.4: ^{2}D Bound State Energies

Configuration	Effective Quantum No.	Calculated Energy Relative To Threshold (Ryd)	Experimental Energy Relative To Threshold (Ryd)
$2s2p^2$	1.90635	-1.10066E+00	-1.10937E+00
$2s^23d$	2.93632	-4.63932E-01	-4.65812E-01
$2s^24d$	3.92769	-2.59290E-01	-2.60092E-01
$2s^25d$	4.92064	-1.65203E-01	-1.65578E-01
$2s^26d$	5.91128	-1.14471E-01	-1.14731E-01
$2s^27d$	6.88228	-8.44490E-02	.....
$2s2p3p$	7.54857	-7.01989E-02	-7.34804E-02
$2s^28d$	8.01167	-6.23181E-02	.....
$2s^29d$	8.95572	-4.98723E-02	.....
$2s^210d$	9.94481	-4.04452E-02	.....
$2s^211d$	10.94027	-3.34198E-02	.....
$2s^212d$	11.93779	-2.80680E-02	.....
$2s^213d$	12.93623	-2.39026E-02	.....
$2s^214d$	13.93517	-2.05985E-02	.....
$2s^215d$	14.93440	-1.79343E-02	.....

Table 3.5: ^{2}G Bound State Energies

Configuration	Effective Quantum No.	Calculated Energy Relative To Threshold (Ryd)	Experimental Energy Relative To Threshold (Ryd)
$2s^25g$	4.99736	-1.60169E-01	-1.60314E-01
$2s^26g$	5.99622	-1.11251E-01	-1.11320E-01
$2s^27g$	6.99564	-8.17344E-02	-8.17746E-02
$2s^28g$	7.99530	-6.25735E-02	-6.26116E-02
$2s^29g$	8.99509	-4.94367E-02	.....
$2s^210g$	9.99494	-4.00405E-02	.....
$2s^211g$	10.99483	-3.30889E-02	.....
$2s^212g$	11.99475	-2.78021E-02	.....
$2s^213g$	12.99469	-2.36880E-02	.....
$2s^214g$	13.99465	-2.04238E-02	.....
$2s^215g$	14.99461	-1.77906E-02	.....

Table 3.6: $^2P^0$ Bound State Energies

Configuration	Effective Quantum No.	Calculated Energy Relative To Threshold (Ryd)	Experimental Energy Relative To Threshold (Ryd)
$2s2p^2$	1.49580	-1.78778E+00	-1.79184E+00
$2s^23p$	2.60390	-5.89943E-01	-5.91739E-01
$2s^24p$	3.59155	-3.10095E-01	-3.11142E-01
$2p^3$	4.03582	-2.45582E-01	-2.54462E-01
$2s^25p$	4.57841	-1.90823E-01	-1.94769E-01
$2s2p3s$	4.90866	-1.66010E-01	-1.72032E-01
$2s^26p$	5.67575	-1.24169E-01	-1.24589E-01
$2s^27p$	6.65919	-9.02022E-02	-9.03910E-02
$2s^28p$	7.65385	-6.82810E-02	.....
$2s^29p$	8.65117	-5.34454E-02	.....
$2s^210p$	9.64954	-4.29582E-02	.....
$2s^211p$	10.64845	-3.52766E-02	.....
$2s^212p$	11.64767	-2.94837E-02	.....
$2s^213p$	12.64708	-2.50080E-02	.....
$2s^214p$	13.64663	-2.14788E-02	.....
$2s^215p$	14.64627	-1.86469E-02	.....

Table 3.7: $^2D^0$ Bound State Energy

Configuration	Effective Quantum No.	Calculated Energy Relative To Threshold (Ryd)	Experimental Energy Relative To Threshold (Ryd)
$2p^3$	2.11887	-4.13724E-01	-4.21035E-01

Table 3.8: $^2F^0$ Bound State Energies

Configuration	Effective Quantum No.	Calculated Energy Relative To Threshold (Ryd)	Experimental Energy Relative To Threshold (Ryd)
$2s^24f$	3.98401	-2.52011E-01	-2.52308E-01
$2s^25f$	4.98101	-1.61223E-01	-1.61382E-01
$2s^26f$	5.97929	-1.11882E-01	-1.12070E-01
$2s^27f$	6.97817	-8.21442E-02	-8.22284E-02
$2s^28f$	7.97740	-6.28547E-02	.....
$2s^29f$	8.97684	-4.96378E-02	.....
$2s^210f$	9.97643	-4.01892E-02	.....
$2s^211f$	10.97611	-3.32019E-02	.....
$2s^212f$	11.97587	-2.78898E-02	.....
$2s^213f$	12.97567	-2.37575E-02	.....
$2s^214f$	13.97552	-2.04797E-02	.....
$2s^215f$	14.97539	-1.78363E-02	.....

3.6 Outer Region Codes

The free state code, STGF was used to determine solutions in the outer region and used quantum defect theory to determine resonance positions and widths, throughout the energy range of interest.

STGF, contains various options for generating an energy mesh on which the final photoionisation cross-sections will be based. The form of the mesh depends in turn on the kind of mesh that is used to search for resonances in the scattering matrix. It has been shown earlier in this chapter, that a straightforward quantum defect mesh is not always accurate enough for the detailed determination of resonance parameters. For highly accurate results an impossibly small step in effective quantum number would have to be used.

Three types of mesh were used, dependent on where in the energy range, the point under consideration lay. The most effort was concentrated in the region above the $2s^2(^1S)$ limit and up to $(1/n^2_{max})$ below the $2s2p(^3P)$ threshold, since this region contained the major contribution to the recombination to the various states, at the temperatures of interest.

The initial mesh had a fixed energy step, that was small enough to provide sufficient resolution to locate all the resonance positions in (2.53). A value of $\sim 10^{-3}$ Z-scaled Rydbergs was used. The resonance positions and widths were written to a file and saved.

The code calculates bound-continuum amplitudes and so the resonance widths correspond to autoionisation probabilities. Since there is no explicit information on the radiative decay rates, it is assumed that they are very much smaller than the autoionisation rates and that in effect the population of a state can be obtained from its local thermodynamic equilibrium (LTE) value. The possibility of departures from thermodynamic equilibrium needed to be investigated since including states where the autoionisation width is not significantly larger than the radiative width would overestimate the contribution of the resonance to the recombination coefficient.

3.6.1 The Autoionisation Approximation

Consider a state U, which can autoionise to the continuum. In local thermodynamic equilibrium (LTE) the population of the state U is defined by

$$N_u^s \Gamma_u^a = N_e N_+ \alpha_c \tag{3.1}$$

where N_u^s is the Saha population and α_c is the dielectronic capture rate coefficient.

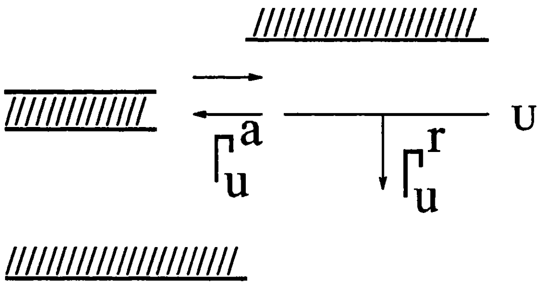

Figure 3.4: The populating and depopulation processes of state U. Γ_u^r is the total radiative transition probability, summed to all final states, and Γ_u^a is the autoionisation transition probability.

In non-LTE,

$$N_e N_+ \alpha_c = N_u(\Gamma_u^a + \Gamma_u^r) \tag{3.2}$$

which gives us

$$b_u = \frac{\Gamma_u^a}{\Gamma_u^a + \Gamma_u^r} \tag{3.3}$$

where b_u is a dimensionless parameter, and is a measure of the departure of the population of U, from its thermodynamic equilibrium.

$$\begin{aligned} &\text{If} \quad \Gamma^a_u \gg \Gamma^r_u, \quad b_u \to 1 \\ &\text{If} \quad \Gamma^a_u \ll \Gamma^r_u, \quad b_u \to 0 \end{aligned} \tag{3.4}$$

The rate of recombination from state U, is proportional to $b_u\Gamma^r_u$. It is assumed that $\Gamma^a_u \gg \Gamma^r_u$ and the population of the state can be given by the Saha equation.

In order to test this assumption, values for both Γ^a_u and Γ^r_u needed to be calculated. For the assumption to be valid, the departure coefficient was required to be larger than $\sim$0.9 for all states.

The values of Γ^a_u were taken from the autoionisation widths calculated by STGF. The value of Γ^r_u was calculated using the Zurich version of the programme SUPERSTRUCTURE (SS) (Eissner *et al.*, 1974, Nussbaumer & Storey, 1978). SS is a general purpose atomic structure program, which enables the calculation of large amounts or radiative data with reasonable accuracy. It requires only the minimum input to specify the atomic system and the level of approximation. SS takes into account configuration mixing which is important in the determination of energy levels and transition probabilities. SS allows configurations to be treated as spectroscopic, or as correlation configurations, used to give better descriptions of the terms of interest. The energies of terms arising from correlation configurations will not be meaningful in a physical sense, but may affect those terms which are spectroscopic. SS calculates the radial functions P_{nl} in a Thomas-Fermi potential. Nussbaumer and Storey abandoned the restriction that all P_{nl} of the same l, are calculated in the same potential and are thus orthogonal to each other. Each P_{nl} is calculated in a separate potential and then orthogonalised to each other such that the function $P_{n_1 l}$ is orthogonalised to the function $P_{n_2 l}$ when $n_2 < n_1$. The adjusting parameter λ_{nl} in the Thomas-Fermi potential is chosen to minimalise the energy sum of selected spectroscopic terms. The list of configurations included in the calculation, is given in Table (3.9).

The states with $2s^2(^1S)$ parents are true bound states, as are the states of $2s2p^2$ and $2p^3$. It is only for states of the form 2s2pnl, excluding states of 2s2p3s and 2s2p3p, which are again true bound states, that the approximation needs to be checked. The results obtained, are given in tables (3.10) and (3.11). The tabulated values of b_{nl} for $^2H^0$ states show clearly that to use them as final states would be an error since the approximation of LTE does not hold. For transitions from ^2G, only $^2F^0$ final states were included in the problem.

Table 3.9: A List of the 87 Configurations in the SUPERSTRUCTURE Calculation

Configuration	n-Range	Terms
2s^2*ns*	3 - 10	^{2}S
2s^2*np*	2 - 10	^{2}P^0
2s^2*nd*	3 - 10	^{2}D
2s^2*nf*	4 - 10	^{2}F^0
2s^2*ng*	5 - 10	^{2}G
2s^2*nh*	6 - 10	^{2}H^0
2s2p*ns*	3 - 10	^{2}P^0
2s2p*np*	3 - 10	^{2}D ^{2}P ^{2}S
2s2p*nd*	3 - 10	^{2}F^0 ^{2}D^0 ^{2}P^0
2s2p*nf*	4 - 10	^{2}G ^{2}F ^{2}D
2s2p*ng*	5 - 10	^{2}H^0 ^{2}G^0 ^{2}F^0
2s2p*nh*	6 - 10	^{2}I ^{2}H^0 ^{2}G
2s2p^2	.....	^{2}D ^{2}P ^{2}S
2p^3	.....	^{2}D^0 ^{2}P^0

The tables reveal some other values of b_{nl}, belonging to other states of smaller L that caused some concern. Most of these have b_{nl} of between 0.8 and 0.9 and it was decided that it was not too unreasonable to include these states in the problem. For states with b_{nl} lower than 0.8, particularly the 2s2p8g state, the respective resonance in the photoionisation cross-section was examined. In each case the resonance was found to be small and contribute little to the total recombination. In such a case it is also not unreasonable to include the resonances in the calculation and so the states remained in the problem. It should be noted that only states up to and including principal quantum number $n = 10$ are considered here. The results were extrapolated when the range of states to be explicitly included was raised to $n \leq 15$, thus excluding ^{2}H^0 final states from this principal quantum number range too.

3.6.2 Free State Mesh: Below the 2s2p (^{3}P^0) Threshold

Once the initial fixed energy search for resonances had been completed and those resonances for which b_{nl} was too small had been eliminated, the file containing resonance positions and widths was fed into a program called RESMESH (Storey, 1992). The function of RESMESH is to generate an energy mesh that maps the resonances in the most accurate way possible.

RESMESH requires the initial $SL\pi$, the maximum step size, h, the energy range and

Table 3.10: Radiative and Autoionisation Transition Probabilities and Departure Coefficients for 2s2pnl States

Term	Configuration	Radiative Transition Probability (S^{-1})	Autoionisation Transition Probability (S^{-1})	b$_{nl}$
^{2}S	2s2p4p	1.60661E+08	8.9719E+12	0.99998
	2s2p5p	1.35033E+08	2.2596E+11	0.99940
	2s2p6p	1.39700E+08	1.7370E+14	1.00000
	2s2p7p	3.29452E+08	3.5064E+13	0.99999
	2s2p8p	2.56305E+08	1.3214E+13	0.99998
	2s2p9p	7.99103E+07	6.9715E+12	0.99999
	2s2p10p	1.80546E+09	5.0612E+12	0.99964
^{2}P^0	2s2p4s	1.19943E+09	4.6995E+13	0.99997
	2s2p5s	6.21671E+08	2.5523E+13	0.99998
	2s2p6s	4.33538E+08	1.5106E+13	0.99997
	2s2p7s	3.83701E+08	9.6372E+12	0.99996
	2s2p8s	1.82359E+09	6.5060E+12	0.99972
	2s2p9s	3.70620E+08	4.5877E+12	0.99992
	2s2p10s	1.57739E+09	3.3911E+12	0.99954
	2s2p3d	4.22363E+08	1.4896E+11	0.99717
	2s2p4d	5.67654E+08	1.9883E+11	0.99715
	2s2p5d	9.89873E+08	4.3421E+10	0.97771
	2s2p6d	2.55820E+08	1.9186E+10	0.98684
	2s2p7d	2.50069E+08	1.0138E+10	0.97593
	2s2p8d	6.12275E+08	5.8813E+09	0.90571
	2s2p9d	3.18546E+08	3.6103E+09	0.91892
	2s2p10d	1.08437E+08	2.6363E+09	0.96049
^{2}D	2s2p4p	2.81369E+08	2.3418E+13	0.99999
	2s2p5p	2.82839E+08	7.3307E+12	0.99996
	2s2p6p	2.08698E+08	8.8931E+12	0.99997
	2s2p7p	6.01504E+08	4.1800E+12	0.99986
	2s2p8p	2.59731E+08	2.5185E+12	0.99990
	2s2p9p	4.86109E+07	1.6626E+12	0.99997
	2s2p10p	2.33484E+09	1.2005E+12	0.99806
	2s2p4f	2.05849E+08	1.8089E+11	0.99886
	2s2p5f	1.06727E+09	3.1491E+11	0.99966
	2s2p6f	6.60450E+07	4.7345E+10	0.99861
	2s2p7f	6.03025E+07	4.8280E+10	0.99875
	2s2p8f	3.10475E+07	3.7605E+10	0.99918
	2s2p9f	2.19352E+07	2.8640E+10	0.99923
	2s2p10f	5.49937E+07	2.0884E+10	0.99737

Table 3.11: Radiative and Autoionisation Transition Probabilities and Departure Coefficients for 2s2pnl States

Term	Configuration	Radiative Transition Probability (S^{-1})	Autoionisation Transition Probability (S^{-1})	b_{nl}
$^2F^0$	2s2p3d	2.07818E+09	1.4416E+12	0.99856
	2s2p4d	1.19651E+09	3.9116E+11	0.99695
	2s2p5d	7.98051E+09	1.7916E+11	0.95736
	2s2p6d	6.30290E+08	5.9377E+10	0.98950
	2s2p7d	5.95580E+08	3.2460E+11	0.99817
	2s2p8d	1.73345E+08	7.7495E+11	0.99778
	2s2p9d	1.94283E+09	1.4696E+12	0.99987
	2s2p10d	6.28430E+08	1.0707E+12	0.99941
	2s2p5g	6.65871E+07	7.1372E+08	0.91467
	2s2p6g	3.87836E+07	2.1598E+08	0.84777†
	2s2p7g	2.47088E+07	1.0726E+08	0.81277†
	2s2p8g	1.68396E+07	1.5018E+07	0.47141†
	2s2p9g	1.23489E+07	2.9542E+08	0.95988
	2s2p10g	1.11561E+07	2.1540E+08	0.95076
^2G	2s2p4f	2.07641E+08	1.6740E+09	0.88965†
	2s2p5f	1.07052E+08	1.3037E+09	0.92412
	2s2p6f	6.44187E+07	4.9289E+08	0.88441†
	2s2p7f	4.48871E+07	2.8973E+08	0.86586†
	2s2p8f	2.72446E+07	1.8235E+08	0.87001†
	2s2p9f	1.82820E+07	1.1020E+08	0.85771†
	2s2p10f	2.34093E+07	8.0332E+07	0.77435†
	2s2p6h	2.61057E+07	3.3416E+08	0.92754
	2s2p7h	1.65187E+07	2.3203E+08	0.93354
	2s2p8h	1.11333E+07	1.5810E+08	0.93421
	2s2p9h	7.88735E+06	1.2105E+08	0.93883
	2s2p10h	5.89764E+06	8.8260E+07	0.93736
$^2H^0$	2s2p5g	6.73100E+07	2.5343E+06	0.03628
	2s2p6g	3.91800E+07	3.2474E+06	0.07654
	2s2p7g	2.49226E+07	2.5091E+06	0.09147
	2s2p8g	1.69094E+07	1.9228E+06	0.10210
	2s2p9g	1.20812E+07	1.4844E+06	0.10942
	2s2p10g	9.18853E+06	1.0822E+06	0.10537

† represents states for which the LTE assumption needed investigation.

the error index, P, such that the maximum error on the integration is smaller than 10^{-P}. The step size is important because at low temperatures, the peak of the Maxwellian velocity distribution, lies close to the $2s^2$ (^1S) threshold. It was found that initial estimates of the maximum step length put the peak between the first two points of the cross-section leading to large errors. This was corrected so that a minimum of 10 points occurred before the peak. The base step size chosen was 2.0×10^{-4} Ryd.

RESMESH reads all the positions and widths and selects those appropriate for the initial $SL\pi$ and those that lie within the specified energy range. The program then searches through the list of resonance positions and widths and finds the nearest resonance, in units of the width, γ. The program assumes a Lorentzian profile for the resonance, given by

$$F(x,\gamma) = \frac{(\frac{\gamma}{2})^2}{(x-x_0)^2 + (\frac{\gamma}{2})^2} \tag{3.5}$$

The program generates points based on the current step length, h, in such a manner, that the mesh is integrable using a 3-point Simpson's rule. This function has a known error which is given by

$$\Delta \sim \frac{h^5}{90} f^{(4)}(\xi) = 10^{-P} \tag{3.6}$$

where $f^{(4)}(\xi)$ is the 4th derivative of the function at the maximum value of the cross-section of the 3 points under consideration. h is given in terms of the derivative and the maximum allowed error by,

$$h^5 = \frac{90 \times 10^{-P}}{f^{(4)}(\xi)} \tag{3.7}$$

This leads to an iterative procedure in which the error is calculated on the integration, the step length is adjusted and the error recalculated from the derivatives at the new positions. This process continues until the error is smaller than the maximum allowed. This gives a step length for the next two points, based on a particular resonance. The program steps through all the resonances, and calculates a step length based on their positions. It then takes the minimum of the values and uses this as the step length for the next two points. Once the entire energy range has been mapped in this fashion, STGF is run again and final state radial wavefunctions obtained at the energies calculated by RESMESH. The assumption of the Lorentzian profile is good for isolated resonances with little background. There exist regions in the cross-sections where the assumption might not be so good. To check this, all the cross-sections were closely examined for signs of resonances that were not well mapped, but none were found.

One problem that arose was that of interlopers from the higher ^{1}P series. In the region below a particular threshold, the program cannot calculate resonances that come from the higher threshold, these having been eliminated by the use of contracted matrices (see §2.4.1). Below the 2s2p (^{3}P^0) threshold there were two resonances from the 2s2p (^{1}P^0) 3p, ^{2}D and ^{2}S states. As they did not appear in the resonance list produced by STGF, they had to be mapped by hand from the photoionisation cross-section and their position and width deduced. These were inserted into the resonance list and the cross-section recalculated. Better values of the position and width were obtained and the process repeated until the values had stabilised.

From $\sim(1/n^2_{max})$ below each threshold, to the threshold, Gailitis averaging is used. (§2.5.3)

3.6.3 Free State Mesh: Above the 2s2p (^{3}P^0) Threshold

In the region above the 2s2p (^{3}P^0) threshold, a quantum defect mesh was used. A very high degree of accuracy is not required since the major contribution to the recombination, even at higher temperatures, comes from below the threshold. However, accuracy was still a concern and so a step in effective quantum number was chosen that put 1000 points between each integer quantum number, relative to the next threshold.

3.7 Photoionisation Cross-sections: Some Results

Figure (3.5) illustrates the mapping of resonances in two of the cross-sections. The respective OP cross-sections are included for comparison. The figure clearly shows the differences in resolution, width and energy the calculated photoionisation cross-sections have compared to the OP ones. Figure (3.6) shows a cross-section calculated using a quantum defect mesh. Again the OP cross-section is included for comparison. When the cross-sections were calculated based on the quantum defect mesh, there was some deliberate overlap with the previously calculated ones. The top half of figure (3.7) illustrates the region just below the ^{3}P^0 threshold where Gailitis averaging is used, giving rise to the averaged OP cross-section, show by the dotted line. The region in which Gailitis averaging is used in this work is smaller since there is data for resonances up to n=15.

To a first approximation, the strength of the background and resonance contributions to the photoionisation cross-section is a function of the parentage of the state. In CII, for example, states belonging to the 2s^2(^{1}S)nl series, have a strong background contribution,

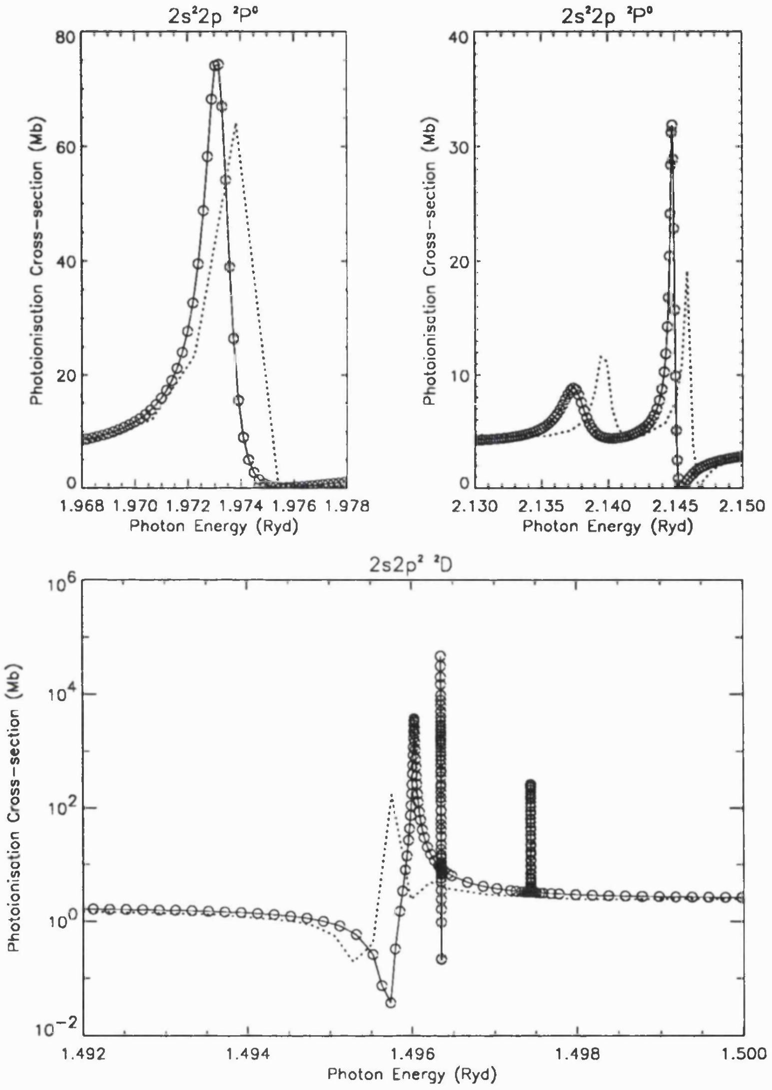

Figure 3.5: Examples of the photoionisation cross-section of $2s^2 2p\ ^2P^0$ (top) and $2s2p^2\ ^2D$ (bottom). The corresponding OP cross-sections are represented by the dotted lines. The difference in resolution, energy and area is very apparent. Each point on the cross-section is labeled as an indication of the resolution of the resonances.

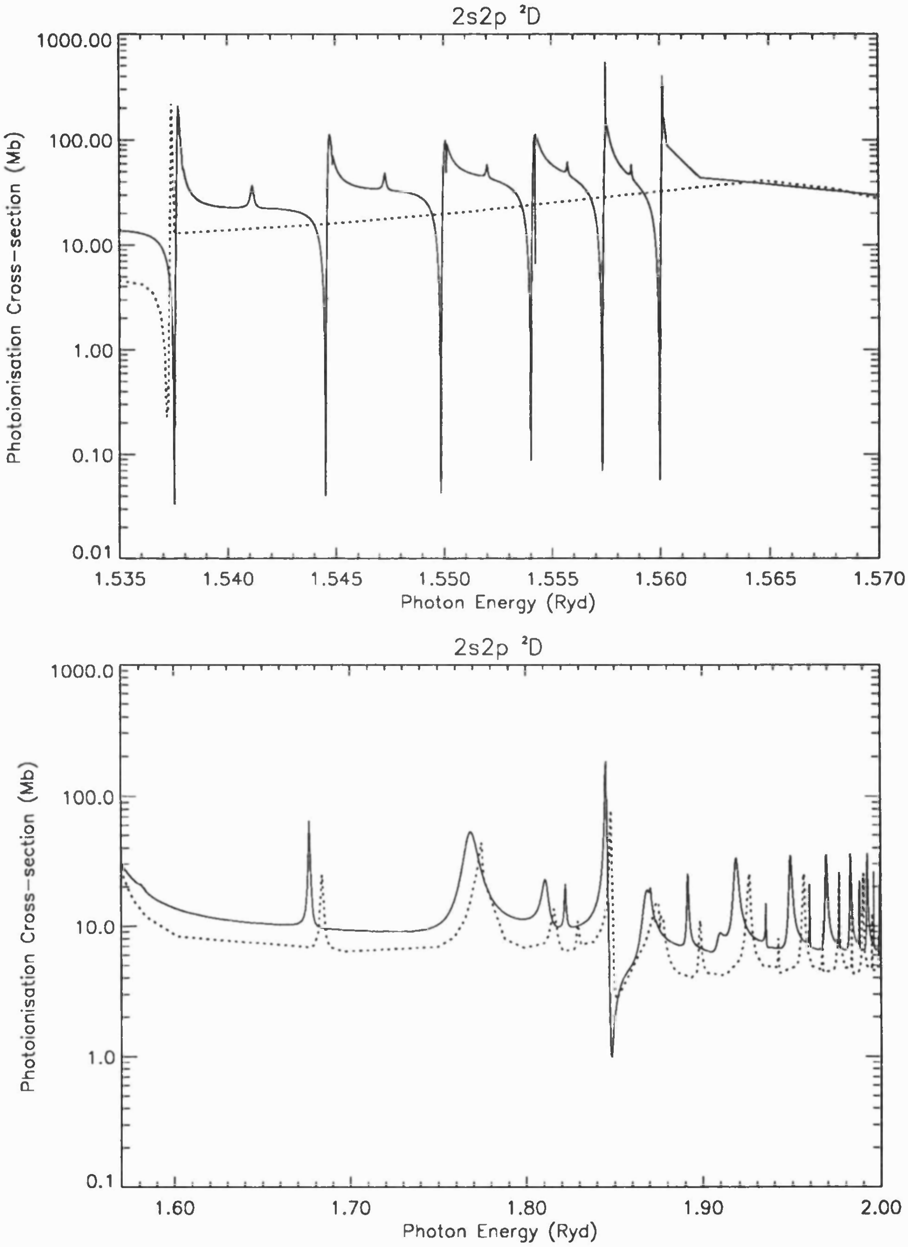

Figure 3.6: An example of the photoionisation cross-section of $2s2p^2$ ^2D in the region where a quantum defect mesh was used. The cross-section is the total one, summed to all final states. The corresponding OP cross-section is represented by the dotted line. Even using a fine quantum defect mesh, the resolution is not comparable to using a dedicated energy mesh.

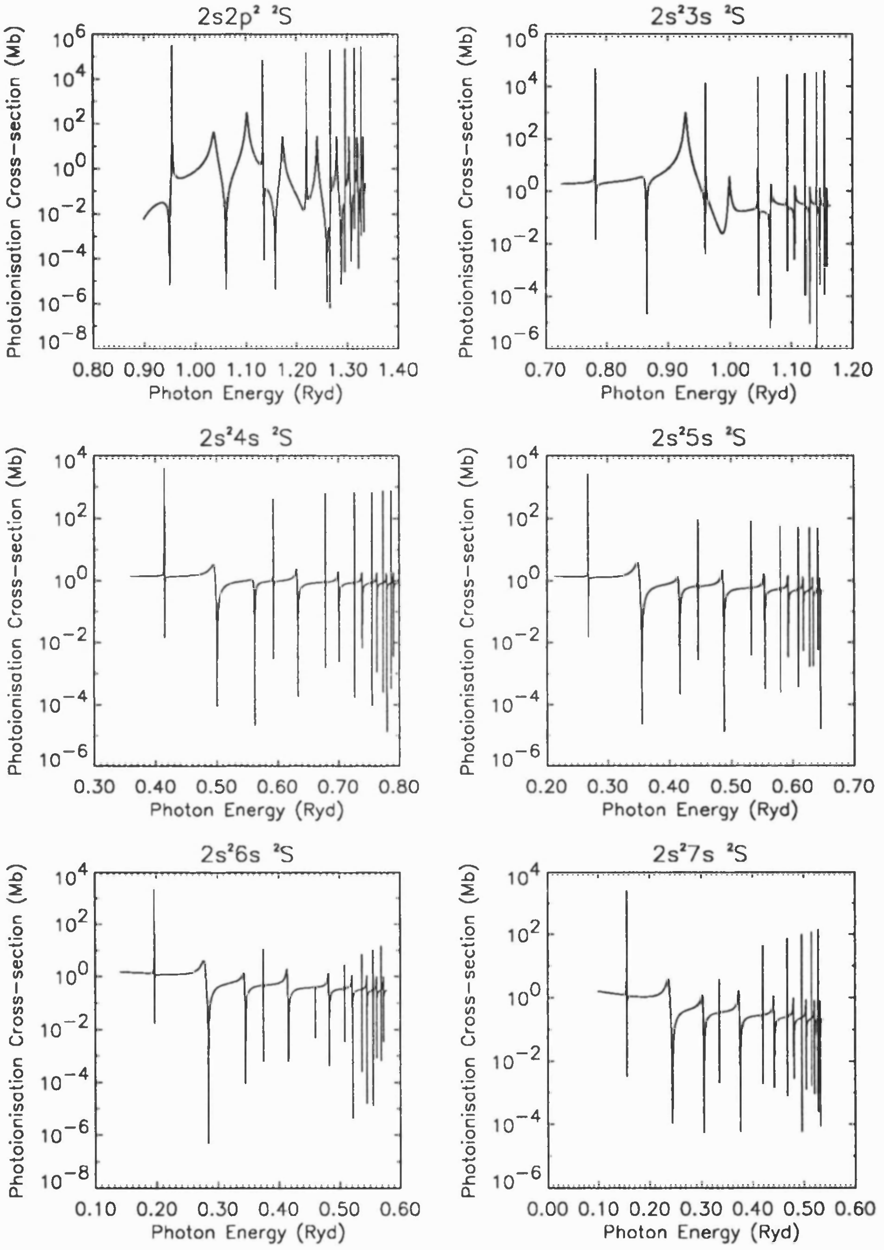

Figure 3.7: ^{2}S Photoionisation cross-sections up to $1/n_{max}^2$ below the 2s2p (^{3}P^0) threshold.

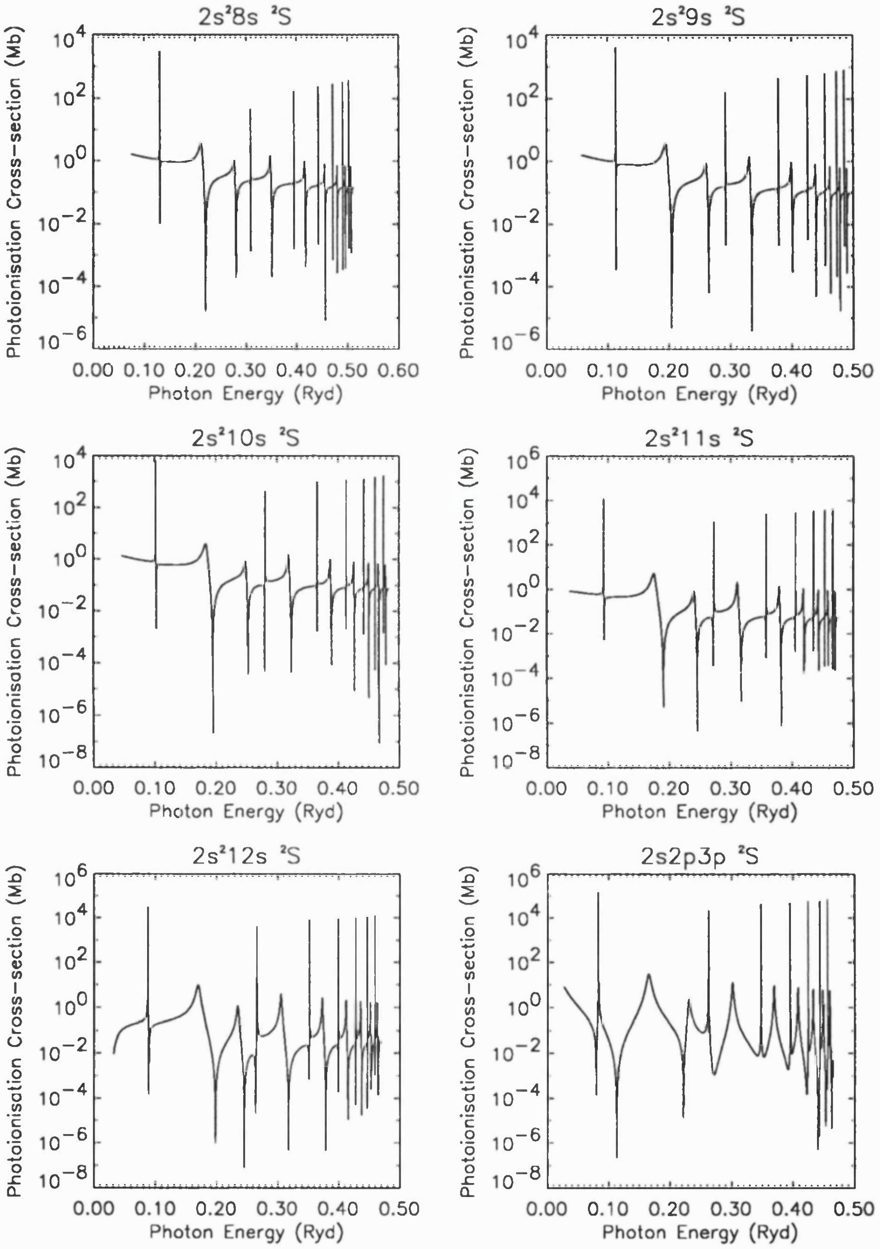

Figure 3.8: ^{2}S Photoionisation cross-sections up to $1/n_{max}^2$ below the 2s2p (^{3}P^0) threshold.

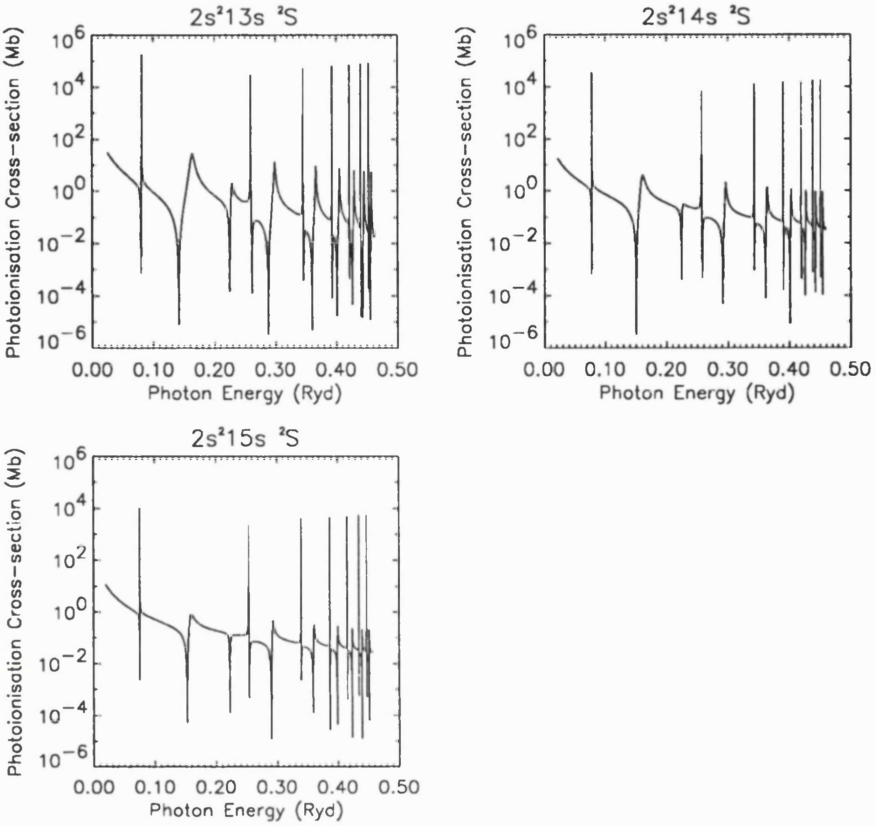

Figure 3.9: ^{2}S Photoionisation cross-sections up to $1/n_{max}^2$ below the 2s2p (^{3}P^0) threshold.

corresponding to photoionisation to the $2s^2(^1S) + e^-$ continuum and weak resonance contributions from the $2s2p(^3P^0)nl$ series of resonances. For bound states of $2s2p(^3P^0)$ parentage, there is a weak background with prominent resonances.

Figures (3.7), (3.8) and (3.9) show the complete set of ^2S cross-sections. These illustrate the points just mentioned, the general trends as n increases and for the $2s^2 12s$ and $2s^2 13s$ states, the perturbation from the 2s2p3p state due to configuration mixing. The perturbation is clearly visible in the reduced background contributions to these two states and the increase in prominence of the resonance contributions, particularly the case of the $2s^2 12s$ state. Conversely the 2s2p3p cross-sections shows an enhanced background contribution. This interaction was one of the principal reasons for extending the calculation up to $n = 15$.

Above the $2s2p(^3P^0)$ threshold, differences in position and values of the background are particularly noticeable. This is illustrated in the bottom diagram of figure (3.7). In this region, more channels are open and this led to the necessity of calculating partial cross-sections to the respective channels. A careful search was made of the resultant photoionisation cross-sections for pseudo resonances, that might arise from the inclusion of correlation orbitals in the target. None were found.

3.8 Conclusions

This chapter presents cross-sections for photoionisation from all doublet states of C II having a principle quantum number $n \leq 15$ and total orbital angular momenta $L \leq 4$; 68 states in total. These were calculated, using the Opacity Project suite of codes which employ the R-matrix method to solve the Schrödinger equation in the close-coupling approximation.

As the previous figures have shown, the general improvement in the photoionisation cross-sections calculated is very marked, when compared to those of the OP. All the resonances are well mapped, the cross-sections showing excellent resolution, and the areas under all cross-sections are larger. The use of the program RESMESH, was fundamental in the determination of the accurate final state energy mesh. The calculated cross-sections represent not only a substantial improvement in accuracy, but also a larger range in both n and L than previous work.

A large amount of effort was directed to ensuring the cross-sections below the $^3P^0$ threshold were as accurate as they could possibly be. Above this threshold, the resolution based on a $\delta\nu$ of 0.001 is still good and certainly no major resonances were missed. The photoionisation cross-sections generated using the 3-point Simpson's rule can easily be turned into accurate recombination coefficients.

Chapter 4

Carbon II Recombination Coefficients

4.1 Introduction

Radiative recombination and dielectric recombination, are the dominant processes in low density plasmas at relatively low temperatures. These processes are characterized by equation (1.1). Recombination into the ground state is usually determined from detailed photoionisation calculations. However an accurate treatment of radiative-cascade problem requires detailed calculations of recombination into excited states. Few such detailed photoionisation calculations had been performed for $n > 2$ states, before the work of the Opacity Project. However, it has been demonstrated that the Opacity Project cross-sections are not always suitable, for the detailed evaluation of recombination rates for states, where dielectronic recombination is the major part of the recombination to a state. Other authors have primarily used scaled hydrogenic rates for higher states, though in some cases an attempt has been made to make allowance for their non-hydrogenic nature. It will be shown in chapter 5, that scaled hydrogenic rates may not be a good approximation for states which have a large quantum defect.

Three approximations were used for determining CII recombination coefficients in the calculations in this thesis. In the region $n \leq 15$, $L \leq 4$ the recombination coefficient is obtained directly by integrating the appropriate R-matrix photoionisation cross-section. For all other states, a hydrogenic recombination coefficient is calculated. In the region $n > 15$, $L \leq 2$ a coulomb to hydrogenic ratio is applied to the hydrogenic results, extrapolated from coulomb to hydrogenic ratios calculated for $L = 0, 1, 2$ at the limit of the tabulation of the coulomb approximation to the recombination coefficients, by Peach (1967).

4.2 Recombination Coefficients: General

Detailed balance arguments, mean that the cross-section for recombination from level i of the N-electron ion, to level f of the (N+1)-electron ion can be written in terms of the cross-section for photoionisation from level f to level i as, (Griffin, 1989),

$$\sigma^r_{if} = \frac{g_f}{g_i}\frac{\varepsilon^2}{(pc)^2}\sigma^p_{fi} \tag{4.1}$$

where g_f is the statistical weight of level f, g_i is the statistical weight of level i, $\varepsilon = h\nu$ is the photon energy, p is the momentum of the free electron and c is the speed of light. The rate coefficient for recombination is given by,

$$\alpha^r_{if}(T_e) = \int_0^\infty v\sigma^p_{if}(v)f(v)dv \tag{4.2}$$

where $f(v)$ is the Maxwell-Boltzmann distribution function,

$$f(v)dv = \left[\frac{2m^3}{\pi(kT_e)^3}\right]^{\frac{1}{2}} v^2 \exp\left(-\frac{mv^2}{2kT_e}\right) dv \tag{4.3}$$

Rewriting equation (4.2), the recombination coefficient to the state f, is given by

$$\alpha^r_{if}(T_e) = \frac{8\pi}{c^2}\frac{N^s_f}{N_e N_i}\int_{\nu_0}^\infty \nu^2\sigma^p_{if}(\nu)\exp\left(-\frac{h\nu}{kT_e}\right)d\nu \tag{4.4}$$

where $\sigma^p_{if}(\nu)$ is the photoionisation cross-section at frequency ν, N_i is the N-electron ion density, N_e is the electron density and N^s_f is given by the Saha equation,

$$\frac{N^s_f}{N_e N_i} = \frac{g_f}{2g_i}\left(\frac{h^2}{2\pi mkT_e}\right)^{\frac{3}{2}}\exp(\chi_f) \tag{4.5}$$

Hence the recombination coefficient is given by,

$$\alpha^r_{if}(T_e) = \frac{8\pi}{c^2}\frac{g_f}{g_i}\left(\frac{h^2}{2\pi mkT_e}\right)^{\frac{3}{2}}\exp(\chi_f)\int_{\nu_0}^\infty \nu^2\sigma^p_{if}(\nu)\exp\left(-\frac{h\nu}{kT_e}\right)d\nu \tag{4.6}$$

This is the basic form of the equation used to obtain recombination coefficients for the various approximations to $\sigma^p_{if}(\nu)$.

4.3 Recombination Coefficients: R-matrix Cross-sections

Chapter 3, detailed the calculation of accurate photoionisation cross-sections for the ground and excited states of CII, $n \leq 15$, $L \leq 4$. The photoionisation cross-sections produced by STGBF are tabulated as a function of photon energy, E_{ph}. Writing the initial state i, in terms of n and l and putting $\chi_f = I_{nl}/kT_e$, where I_{nl} is the ionisation energy of the initial state relative to to the ^{1}S threshold,

$$E_{ph} = I_{nl} + E_f \tag{4.7}$$

where E_f is the free electron energy. The integral in (4.6) becomes,

$$\int_{I_{nl}}^{\infty} E_{ph}^2 \sigma_{nl}^p(E_f) \exp\left(-\frac{I_{nl}+E_f}{kT_e}\right) dE_f \tag{4.8}$$

Putting,

$$G(E_f) = E_{ph}^2 \sigma_{nl}^p(E_f) \exp\left(-\frac{E_f}{kT_e}\right) \tag{4.9}$$

Equation (4.6) can then be written,

$$\alpha_{nl}^r(T_e) = 2.061850776 \times 10^{-13} g_{nl} \left(\frac{1}{T_e}\right)^{\frac{3}{2}} \int_{I_{nl}}^{\infty} G(E_f) dE_f \tag{4.10}$$

and this is the form used in the integration. The function, $G(E_f)$ is tabulated at each energy point and the integration is evaluated from the 1s^2(^{1}S) threshold up to $1/n_{max}^2$ below the 2s2p(^{3}P^0) threshold using Simpson's 3-point rule.

4.3.1 Moving the 2s2p(^{3}P^0)3d, ^{2}F^0 and ^{2}P^0 Resonances

The terms in the ground complex, such as 2s2p^2 ^{2}D, have mixed parentage and can have large resonance contributions from more than one series. It has also been noted (Storey, 1982) that in CII, the dominant contribution to the recombination coefficient of the 2s2p^2 ^{2}D states comes from the 2s2p(^{3}P^0)3d ^{2}F^0 resonance. It is not only an important source of recombination for this state, but for all states in which it occurs, particularly at low temperatures when the peak of the Maxwellian velocity distribution will lie close to threshold. The 2s2p(^{3}P^0)3d ^{2}P^0 resonance, though higher in energy is also a considerable source of recombination to allowed initial states at higher temperatures.

In general the theoretically calculated energies of states will be higher than experimentally derived values. In the work of the Opacity Project the exact positioning of resonances was not critical to the calculations. For low temperature recombination work though, their placement is critical. A small change in the position of the resonances leads to a big change in the the value of the total recombination coefficient as shown in figure (4.2).

The experimentally determined positions of the ^{2}F^0 and ^{2}P^0 resonances (Moore, 1970) are respectively, 3301 cm^{-1} and 5523 cm^{-1} above the 2s^2(^{1}S) threshold. This compares

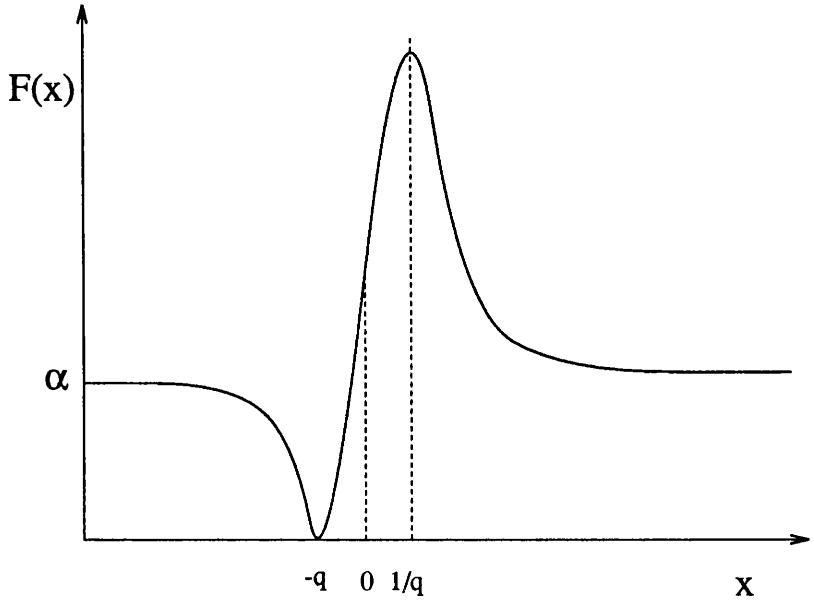

Figure 4.1: A general Fano profile for resonance fitting.

with the theoretically calculated values of 3778 cm^{-1} and 6172 cm^{-1}. It was decided to evaluate the resonance contributions to the total recombination coefficient at their experimental rather than the theoretically calculated energies. The resonances were in effect moved.

This was done by fitting the area around the resonances using a Fano profile (Fano, 1961). The Fano profile for a fit to a single channel resonance is given by,

$$F(x) = \alpha \frac{(x+q)^2}{(1+x^2)} \tag{4.11}$$

As $x \rightarrow \pm\infty, F(x) \rightarrow \alpha$. Hence α can be thought of as the background contribution. Differentiating,

$$F'(x) = \frac{2\alpha(x+q)(1-xq)}{(1+x^2)^2} \tag{4.12}$$

This gives

$$F'(x) = 0 \begin{cases} x = -q & \text{minimum} \\ x = \frac{1}{q} & \text{maximum} \end{cases} \tag{4.13}$$

This gives a ratio of peak cross-section to background of $(1+q^2)$. A negative value of q would change the order of minimum and maximum. If there is another channel whose cross-section is added, then the profile should be,

$$F_1(x) = \beta + \alpha \frac{(x+q)^2}{(1+x^2)} \tag{4.14}$$

Table 4.1: Recombination Coefficients for the $2s2p^2(^2D)$ State.

Temp.	Recombination Coefficient		Resonance Contributions			
(K)	α_i	α_f	$\alpha_i^{^2F^0}$	$\alpha_f^{^2F^0}$	$\alpha_i^{^2P^0}$	$\alpha_f^{^2P^0}$
1000	1.2819D-18	2.0962D-18	1.0700D-18	1.8842D-18	1.3771D-22	1.6327D-22
2000	5.0003D-18	6.6949D-18	4.8450D-18	6.5395D-18	2.7791D-22	3.8040D-22
3000	6.4904D-18	7.8874D-18	6.3572D-18	7.7540D-18	4.8564D-22	6.2053D-22
4000	6.5469D-18	7.5668D-18	6.4212D-18	7.4410D-18	6.0433D-22	7.3021D-22
5000	6.1192D-18	6.8598D-18	5.9899D-18	6.7304D-18	6.4636D-22	7.5229D-22
6000	5.5803D-18	6.1280D-18	5.4381D-18	5.9858D-18	6.4476D-22	7.3110D-22
7000	5.0585D-18	5.4729D-18	4.8964D-18	5.3108D-18	6.2147D-22	6.9138D-22
8000	4.5921D-18	4.9124D-18	4.4058D-18	4.7260D-18	5.8862D-22	6.4542D-22
9000	4.1870D-18	4.4395D-18	3.9744D-18	4.2268D-18	5.5257D-22	5.9905D-22
10000	3.8385D-18	4.0408D-18	3.5992D-18	3.8015D-18	5.1656D-22	5.5490D-22
11000	3.5386D-18	3.7033D-18	3.2736D-18	3.4382D-18	4.8212D-22	5.1402D-22
12000	3.2797D-18	3.4153D-18	2.9906D-18	3.1263D-18	4.4996D-22	4.7672D-22
13000	3.0547D-18	3.1678D-18	2.7438D-18	2.8569D-18	4.2029D-22	4.4292D-22
14000	2.8580D-18	2.9532D-18	2.5275D-18	2.6227D-18	3.9311D-22	4.1237D-22
15000	2.6847D-18	2.7656D-18	2.3371D-18	2.4180D-18	3.6828D-22	3.8479D-22
16000	2.5311D-18	2.6003D-18	2.1687D-18	2.2379D-18	3.4563D-22	3.5987D-22
17000	2.3939D-18	2.4537D-18	2.0190D-18	2.0787D-18	3.2498D-22	3.3731D-22
18000	2.2708D-18	2.3227D-18	1.8853D-18	1.9372D-18	3.0612D-22	3.1687D-22
19000	2.1596D-18	2.2049D-18	1.7654D-18	1.8107D-18	2.8888D-22	2.9829D-22
20000	2.0586D-18	2.0983D-18	1.6575D-18	1.6973D-18	2.7309D-22	2.8136D-22

α_i and α_f are the total recombination coefficients at the initial and moved resonance positions. The coefficients superscripted $^2F^0$ and $^2P^0$ represent the initial and moved individual resonance contributions to the total recombination coefficient.

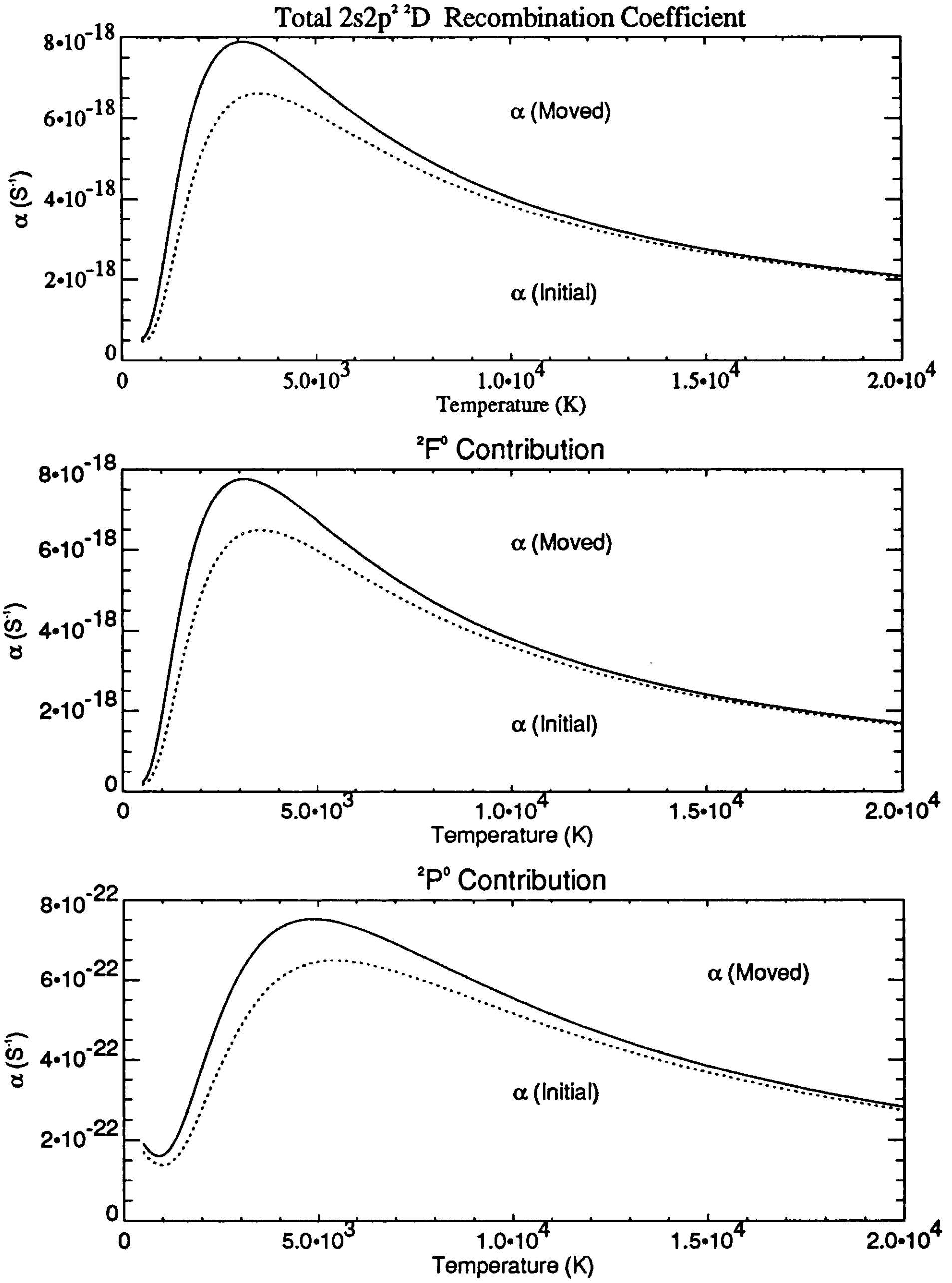

Figure 4.2: The effect of moving the $^2P^0$ and $^2F^0$ resonances on the 2s2p^2 ^2D recombination coefficient. The top figure illustrates the effect on the total recombination coefficient of moving the two resonances. The central figure illustrates both the effect of moving the $^2F^0$ resonance and the size of its contribution to the final recombination coefficient. The lower figure illustrates the effect of moving the $^2P^0$ resonance.

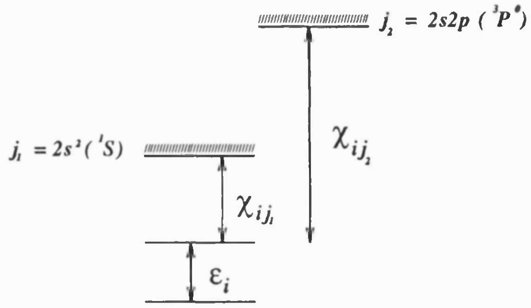

Figure 4.3: The lowest two excitation thresholds of CII

The value of β can be estimated from the minimum point, $x = -q$, since then $F_1(x) = \beta$.

This form does not allow for any energy dependence in the background, so can only be used to fit a narrow energy range. The initial position and width of the resonance is taken from the output of STGF and the quantities q, β and α can be easily deduced. A single profile is then produced for the resonance at its calculated position and a recombination coefficient over the entire energy range evaluated. A new profile is then generated, differing only in the energy of the peak of the profile, and integrated to give a new value of the contribution to the total recombination coefficient for the resonance. The integration mesh is generated by RESMESH (§3.6.3) so the accuracy and the ease of integration can be maintained. Using the new profile, gives a modified recombination coefficient for the state with the resonance contributions evaluated at their experimental positions. This method was applied to all cross-sections in which the two resonances appeared, for all states $n \leq 10$. The effect on the value of the recombination coefficient over a range of temperatures is illustrated on the previous page. Table (4.3.1) gives the quantitative effect of the individual resonance contributions, and their combined effect on the total recombination coefficient for the 2s2p^2 ^{2}D state.

4.3.2 Above the 2s2p(^{3}P^0) Threshold

From ~1/n^2 below the 2s2p(^{3}P^0) threshold up to the highest energy considered, a quantum defect cross-section was calculated. In this region a trapezoidal rule is used to integrate the cross-section. Above the threshold, another channel is open and the recombination coefficient is calculated in a modified form to (4.6),

$$\alpha_{j,i} = \frac{8\pi}{c^2}\left(\frac{N_i}{N_e N_j^+}\right)_{Saha} \int_0^\infty \nu^2 \sigma_{i,j}(\nu) \exp\left(-\frac{h\nu}{kT_e}\right) d\nu \tag{4.15}$$

where $h\nu$ is the photon energy, $\sigma_{i,j}(\nu)$ is the cross-section from initial state i to final state

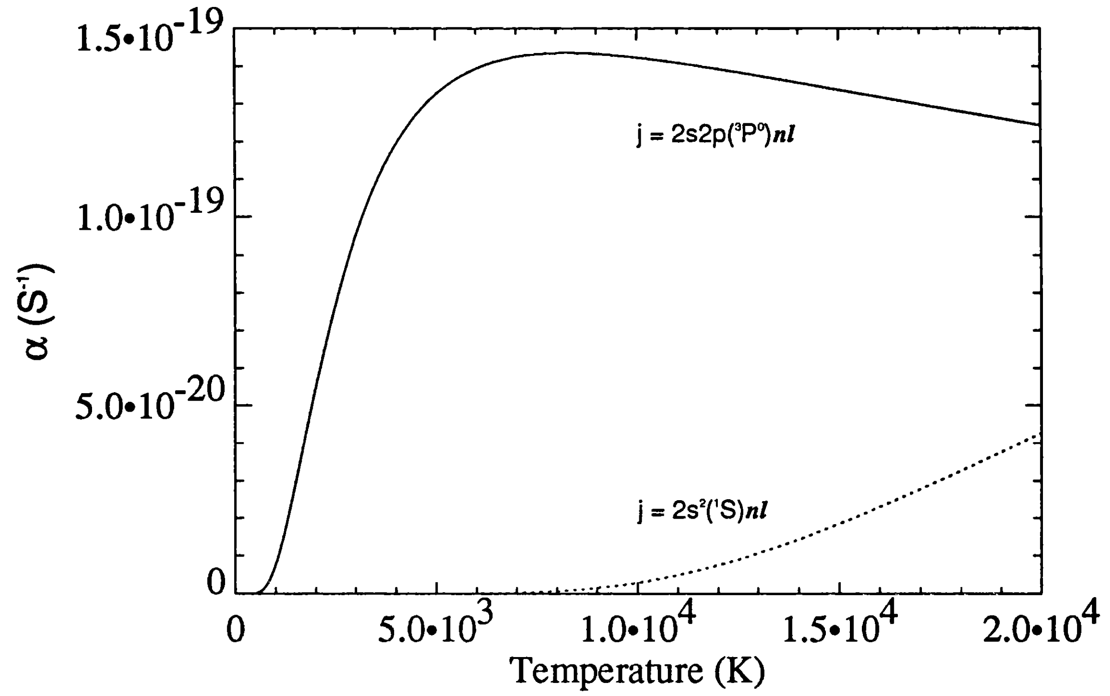

Figure 4.4: The two contributions to the 2s2p^2 ^{2}D recombination coefficient from the ^{1}S and ^{3}P^0 parent states above the 2s2p(^{3}P^0) threshold.

j. STGBF provides both length and velocity partial cross-sections to each open channel and following convention, the length formulation only was used. The Saha bracket is given by,

$$\left(\frac{N_i}{N_e N_j^+}\right)_{Saha} = \frac{g_i}{g_j^+}\left(\frac{h^2}{2\pi mkT}\right)^{\frac{3}{3}} \exp\left(\frac{\chi_{i,j}}{kT}\right) \tag{4.16}$$

Here, g_i, g_j^+ are the statistical weights of the recombined state and the initial ion state respectively, and $\chi_{i,j}$ is the ionization energy of the state i relative to the excited ion state j. See figure (4.3).

4.3.3 Evaluating the 2s^2(^{1}S) and 2s2p(^{3}P^0) populations

The contribution to the total recombination coefficient of a state, is dependent on the relative populations of the 2s^2(^{1}S) and 2s2p(^{3}P^0) states. (For the temperature and density range under consideration, the effective population of CIII can be thought to reside in these two states.)

$$N(^1S) + N(^3P^0) = N(C^{2+}) \tag{4.17}$$

$$\frac{N(^1S)}{N(C^{2+})} + \frac{N(^3P^0)}{N(C^{2+})} = 1 \tag{4.18}$$

The contribution to the recombination to the level i, α_i, is given by,

$$\alpha_i = \sum_j \frac{N_j^+}{N^+} \alpha_{j,i} \tag{4.19}$$

where N^+ is the total number density of ions. The 2s2p(^{3}P^0) state will be populated by collisional excitation and depopulated by collisional de-excitation, and radiative decay.

$$N_i q_{ij} N_e = N_j [A_{ji} + q_{ji} N_e] \tag{4.20}$$

This gives

$$\frac{N_j}{N_i} = \frac{N_e q_{ij}}{N_e q_{ji} + A_{ji}} \tag{4.21}$$

The collisional de-excitation rate coefficient, q_{ji}, can be obtained from the relation (Mendoza, 1982),

$$q_{ji}(T_e) = \frac{8.63 \times 10^{-6} \gamma_{ji}(T_e)}{w_j T_e^{\frac{1}{2}}} \quad (\mathrm{cm}^3\mathrm{s}^{-1}) \tag{4.22}$$

where w_j is the statistical weight of the upper level. The excitation rate coefficient is given by,

$$q_{ij} = \frac{w_j}{w_i} q_{ji} \exp\left(\frac{-\Delta E_{ji}}{kT_e}\right) \quad (j > i) \tag{4.23}$$

$\gamma_{ji}(T_e)$ is the effective collision strength (Dufton *et al.* 1978) and is the value for the whole multiplet. $A(^3P_1^0 \rightarrow ^1 S) = 120$ s^{-1} (Kwong *et al.*, 1993), however this is a single multiplet value. An average, over all possible J values is used, $A_{ji}^{Av} = 40.3$. and hence the ratio (4.21) is evaluated. Let this ratio be X, the fractional population.

$$\frac{N(^1\mathrm{S})}{N(\mathrm{C}^{2+})} = \frac{1}{1+X} \tag{4.24}$$

and

$$\frac{N(^3\mathrm{P}^0)}{N(\mathrm{C}^{2+})} = \frac{X}{1+X} \tag{4.25}$$

These two ratios give coefficients by which the previously calculated recombination coefficients, from each final state, were multiplied. Figure (4.5) illustrates the relative population of the 2s2p(^{3}P) state as a function of density at 20000 K. The contribution from the 2s2p(^{3}P) state only starts to be significant at densities, $N_e > 10^9$ cm^{-3}. At typical Wolf Rayet stellar wind temperature/densities, this contribution will not be more than ~8%. The maximum possible contribution, given by the Boltzmann distribution, is ~17% which is approached at densities, $N_e > 10^{11}$ cm^{-3}.

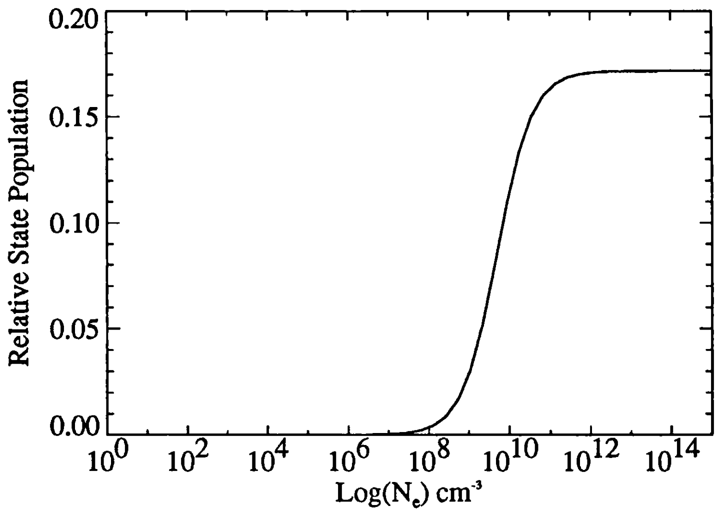

Figure 4.5: The relative population in the 2s2p(^{3}P^0) state of CIII as a function of density at 20000 K.

4.3.4 Tabulating the Integrated Recombination Coefficients

For speed of calculation, the recombination coefficients for all states in the range 400–20000 K were calculated at intervals of 100 K and stored in a data file. Coefficients at the tabulation points were then obtained directly and for temperatures in between, 4-point Lagrange interpolation was used. In cases where the recombination coefficient is changing rapidly ie. at low temperatures, the values were converted to logarithmic quantities, which are then interpolated. Interpolation rather than direct calculation provided negligible loss of accuracy. The worst case discrepancy was shown to be less than < 0.3%.

4.4 Recombination Coefficients: Hydrogenic Cross-sections

For all states for which a R-matrix photoionisation cross-section had not been calculated explicitly, a hydrogenic approximation to the photoionisation cross-section was evaluated, using the routines of Storey and Hummer (1991) which were designed for the fast computation of radiative data in hydrogenic systems. The photoionisation cross-section of state nl, is given by,

$$a_\nu(nl \rightarrow El') = \left(\frac{4\pi\alpha}{3}\right)\frac{(1+n^2k^2)}{\mu^2 Z^2 n^2}\frac{l_>}{(2l+1)}\left|\int_0^\infty P_{nl}(\rho)\rho G_{kl'}(\rho)d\rho\right|^2 \qquad (4.26)$$

where μ is the reduced mass and the constant $\frac{4\pi\alpha}{3}a_0^2 = 8.5596557 \times 10^{-25} m^2$.

4.4.1 Evaluation of the Radial Integrals

The matrix elements of equation (4.26) are evaluated, by Storey and Hummer (1991) using the method of Infeld and Hull (1951). $R(l,l')$ is defined such that,

$$R(l',l) \equiv \int_0^\infty P_{n'l'}(\rho)\rho P_{nl}(\rho)d\rho \tag{4.27}$$

where the primed quantities now refer to the lower state. $P_{n'l'}(\rho)$ and $P_{nl}(\rho)$ are orbitals of bound state type. For fixed values of n', n. Infeld and Hull (1951) obtained the following recurrence relations,

$$2lC(n',l)R(l-1,l) = (2l+1)C(n,l+1)R(l,l+1) + C(n',l+1)R(l+1,l) \tag{4.28}$$

and

$$2lC(n,l)R(l,l-1) = C(n,l+1)R(l,l+1) + (2l+1)C(n',l+1)R(l+1,l) \tag{4.29}$$

where

$$C(n,l) = [(n-l)(n+l)]^{\frac{1}{2}}/(nl) \tag{4.30}$$

All the necessary integrals for a given set (n', n) can be generated given two starting values,

$$R(n',n'-1) = 0 \tag{4.31}$$

and from Gordon (1929),

$$R(n'-1,n') = \frac{1}{4}(4nn')^{n'+2}\left[\frac{(n+n')!}{(n-n'-1)!(2n'-1)!}\right]^{\frac{1}{2}}\frac{(n-n')^{n-n'-2}}{(n+n')^{n+n'+2}} \tag{4.32}$$

The recursive evaluation of R proceeds in descending order of l'. The recurrence relations are also valid for,

$$\tilde{R}(l,l') \equiv \int_0^\infty P_{n'l'}(\rho)\rho G_{kl}(\rho)d\rho \tag{4.33}$$

where $G_{kl}(\rho)$ represents an orbital of free state type. Substituting $n = i/k$ in (4.30) gives,

$$\tilde{C}(k,l) = \frac{(1+l^2k^2)^{\frac{1}{2}}}{l} \tag{4.34}$$

The starting values are,

$$\tilde{R}(n',n'-1) = 0 \tag{4.35}$$

and again from Gordon (1929),

$$\tilde{R}(n'-1,n')_{k=0} = \frac{1}{4}\left[\frac{\pi}{2(2n'-1)!}\right]^{\frac{1}{2}}(4n')^{n'+2}\exp(-2n') \tag{4.36}$$

and

$$\tilde{R}(n'-1,n')_k = \left[\frac{\Pi_{s=1}^{n'}(1+s^2k^2)}{1-\exp(-2\pi/k)}\right]^{\frac{1}{2}} \frac{\exp[2n' - (2/k)\arctan(n'k)]}{(1+n'^2k^2)^{n'+2}}\tilde{R}(n'-1,n')_{k=0} \quad (4.37)$$

Using the stable recursive procedures described the dipole radial integrals from states of different orbital angular momentum were evaluated and hydrogenic cross-sections and hydrogenic recombination coefficients calculated.

4.5 Recombination Coefficients: Coulomb Cross-sections

A coulomb approximation to the photoionisation cross-section can be calculated using the methods of Peach (1967). The cross-section at frequency $\tilde{\nu}$ is given by,

$$\sigma_{\tilde{\nu}}(\varepsilon',\nu) = \frac{4\pi\alpha a_0^2}{3}(I_{nl} + z^2\varepsilon') \sum_{l'=l\pm 1} C_{l'} \left| \int_0^\infty P_{\nu l}(r) r G_{k'l'}(r) dr \right|^2 \quad (4.38)$$

where the nl electron has been ejected and $I_{nl} = z^2/\nu^2$ (Rydbergs) is the associated threshold ionisation energy. z is the residual charge on the final ion and ν is the effective quantum number of the initial state. $k'^2 = z^2\varepsilon'$ denotes the energy in Rydbergs of the ejected electron. Expressions for the coupling coefficients $C_{l'}$ are given by Burgess and Seaton (1960). The initial bound radial function $P_{\nu l}$ is defined by,

$$P_{\nu l}(r) = z^{\frac{1}{2}} K(\nu,l) W_{\nu,l+\frac{1}{2}}\left(\frac{2\rho}{\nu}\right) \quad (4.39)$$

where W is the Whittaker function. The normalising factor is

$$K(\nu,l) = [\zeta(\nu,l)\nu^2\Gamma(\nu+l+1)\Gamma(\nu-l)]^{\frac{1}{2}}; \quad \zeta(\nu,l) = 1 + \frac{2}{\nu^3} \quad (4.40)$$

$\mu = n - \nu$ being the quantum defect for the series of initial states of the same parent. For all but the lowest series members, $\zeta(\nu,l)$ is generally taken to be unity. The asymptotic form of the Whittaker function is,

$$W_{\nu,l+\frac{1}{2}}\left(\frac{2\rho}{\nu}\right) = \left(\frac{2\rho}{\nu}\right)^{\nu} e^{-\rho/\nu} \sum_{t=0}^{t'} b_t(\nu,l)\rho^{-t}; \quad \rho = zr \quad (4.41)$$

where $b_0 = 1$ and

$$b_t = \frac{\nu}{2t}[l(l+1) - (\nu-t)(\nu-t+1)]b_{t-1}, \quad t \geq 1 \quad (4.42)$$

An approximate bound-state radial wave function is thus defined for all r by

$$P_{\nu l}(r) = z^{\frac{1}{2}} K(\nu,l) \left(\frac{2\rho}{\nu}\right)^{\nu} e^{-\rho/\nu} \sum_{t=0}^{t'} b_t(\nu,l)\rho^{-t} \quad (4.43)$$

For $\nu = n = (l+1), (l+2), ...$, equation (4.42) terminates at $t = t^1 = n - l - 1$ and is then equal to the exact hydrogenic eigenfunction. The choice of t_0 is discussed by Bates and Damgaard (1949).

The continuum function $G_{k'l'}(\mathrm{r})$, is given by Burgess and Seaton (1960),

$$G_{k'l'}(r) = Z^{-\frac{1}{2}}\{F_{k'l'}(r)\cos\pi\mu' + H_{k'l'}(r)\sin\pi\mu'\} \tag{4.44}$$

where

$$H_{k'l'}(r) = [1 - \exp(-\tau_{l'}r)]^{2l'+1}H'_{k'l'} \tag{4.45}$$

$F_{k'l'}$ and $H_{k'l'}(r)$ are the regular and irregular solutions of the coulomb equation,

$$\left\{\frac{d^2}{dr^2} - \frac{l'(l'+1)}{r^2} + k'^2\right\}y_{k'l'} = 0 \tag{4.46}$$

This gives $G_{k'l'}$ the virtually exact asymptotic form

$$G_{k'l'} \sim k'^{-\frac{1}{2}}\sin\left[k'r - \frac{1}{2}l'\pi + \frac{z}{k'}\ln(2k'r) + \arg\Gamma\left(l' + 1 - \frac{iz}{k'}\right) + \pi\mu'\right] \tag{4.47}$$

The cutoff parameter $\tau_{l'}$, in (4.45) is necessary to remove the divergence of the irregular function at the origin (Burgess and Seaton, 1960) and their definition $\tau_{l'} = 10/(l'(l'+1))$, is used.

4.5.1 Evaluation of the Radial Integrals

For $\rho \geq 20$, $F_{k'l'}(r)$ and $H_{k'l'}(r)$ are obtained using the W.K.B. functions derived by Burgess (1963) which are known to be accurate for large ρ. The integrals,

$$\int_{20}^{\infty} P_{\nu l}(r)rF_{k'l'}dr, \qquad \int_{\rho}^{\infty} P_{\nu l}(r)rH_{k'l'}dr, \tag{4.48}$$

can be evaluated using Gaussian quadrature. For $\rho \leq 20$ $F_{k'l'}(r)$ and $H_{k'l'}(r)$ are calculated by direct numerical integration of the coulomb equation, integrating outwards for the regular function and inwards for the irregular function, using the W.K.B. functions to give starting values for the Numerov integration procedure.

Peach (1967) tabulates the integral functions only as far as $\nu \leq 11$, $L \leq 2$. In order to take advantage of using a coulomb approximation over a hydrogenic one, a ratio of the hydrogenic values, previously calculated at $n = 11$ for $L = 0, 1, 2$, to the coulomb values for the same values of L, were calculated. The ratios were then applied to all the hydrogenic values calculated for states $n > 15$, $L \leq 2$.

4.6 Conclusions

This chapter detailed the calculation of recombination coefficients for subsequent use in the level population calculations. A sensible balance between accuracy and effort was struck. In the case of recombination coefficients for lower states, great care was taken to ensure the accuracy inherent in the R-matrix photoionisation cross-sections was maintained. Moving the 2s2p(^{3}P^0)3d (^{2}F^0,^{2}P^0) resonances in the appropriate cross-sections markedly increased their contribution to the recombination coefficients. As an example, the placement of the two resonances at their experimental positions brought about a 63% increase in the recombination coefficient of the 2s2p^2(^{2}D) state at 1000 K. The necessity of a detailed treatment of recombination into excited states was illustrated by comparing the integrated values with hydrogenic and coulomb values. The hydrogenic approximation to the recombination coefficient for the 2s^{2}11s state at 10000 K overestimates the value integrated from the appropriate R-matrix photoionisation cross-section by 250%. In the case of the 2s^{2}12s state hydrogenic / coulomb approximations again give values which are severely in error as the state is affected by configuration mixing, which lowers its recombination coefficient.

However, states with $L \geq 5$ are very nearly hydrogenic and it made sense to make use of a hydrogenic approximation in this region. It was expected that all approximations should converge on the hydrogenic values for high values of angular momenta and there was very little to be gained from performing a more detailed calculation. A degree of refinement to the hydrogenic values was gained by using extrapolated coulomb values above $\nu = 15$ incorporating the available quantum defect data, for states, $L \leq 2$.

Chapter 5

Level Populations

5.1 Introduction

The population of a state is given, in equilibrium, by equating the populating and depopulating processes of any given level.

The primary excitation process in a low density astrophysical plasma is photoionisation. The inverse process, is radiative recombination and in the case of CII, involves photo-electrons recombining with a doubly charged ion. The importance of dielectronic recombination has also been noted. The capture of an electron by either of these processes gives rise to an ion in an excited state, X^+_{a*}. Population, will be quickly followed by depopulation, by means of radiative decay to any allowed state of lower energy, X^+_{b*},

$$X^+_{a*} \rightarrow X^+_{b*} + h\nu \tag{5.1}$$

Cascade will continue until the atom reaches the ground state or a meta-stable level. In regions of low density ($\lesssim 10^4$ cm^{-3}), such as planetary nebulae, the effects of collisional processes may be neglected, except in so far as they maintain a Maxwellian velocity distribution among the free electrons.

In regions of higher density, collisional processes become increasingly more important and above densities of $\sim 10^5$ cm^{-3}, particularly for high L states, become the dominant populating and depopulating mechanisms. These processes include, collisional ionisation and its inverse process, three body recombination given by equation (1.1). They also include collisional redistribution of energy and angular momentum, typified by

$$X^+_{b*} + P \rightleftharpoons X^+_{c*} + P \tag{5.2}$$

where X^+_{c*} is a state for which, either, just the total angular momentum changes, or the principal quantum number and the angular momentum change. P is any charged perturber and rates were evaluated for collisions with electrons, protons and helium nuclei with respective fractional ratios of 1.0, 0.833 and 0.0833.

The evaluation of the recombination rates has been given in detail in chapter 4. The approximations used in the evaluation of rates for the other radiative and collisional processes, and the evaluation of the equilibrium population of a state, for a given temperature and density, are detailed here.

5.2 Carbon II Transition Probabilities

Spontaneous radiative transition probabilities were required between all states, $n \leq NLIM$, where $NLIM$ was the variable limit of n for which population solutions were obtained explicitly for all L. The total radiative decay rate for each state, $n \leq NLIM$, was calculated and used directly in the solution of the level population equations and indirectly, as a cut-off in the calculation of collisional rates.

Spontaneous radiative transition probabilities were evaluated using, four approximations, dependent on the region of calculation. These approximations were;

- rates derived from CII oscillator strengths calculated using the Opacity Project suite of codes
- coulomb and hydrogenic rates and
- rates derived from interpolation in photoionisation cross-sections extended below the ^{1}S threshold.

Figure (5.1) illustrates the regions where the various approximations were used.

5.2.1 Transition Probabilities Calculated Using Opacity Project Codes

Initial calculations made use of the CII oscillator strengths calculated in the course of the Opacity Project (Yu Yan *et al.*, 1987). These were recalculated following the changes, to the number of basis functions and the size of the R-matrix box and to extend the calculations to cover the same range of principal quantum number and total angular momenta as the R-matrix photoionisation cross-section calculations.

The close-coupling methods detailed in Berrington *et al.* (1987), were used to calculate weighted oscillator strengths, *gf*, for all transitions between states of CII having principal

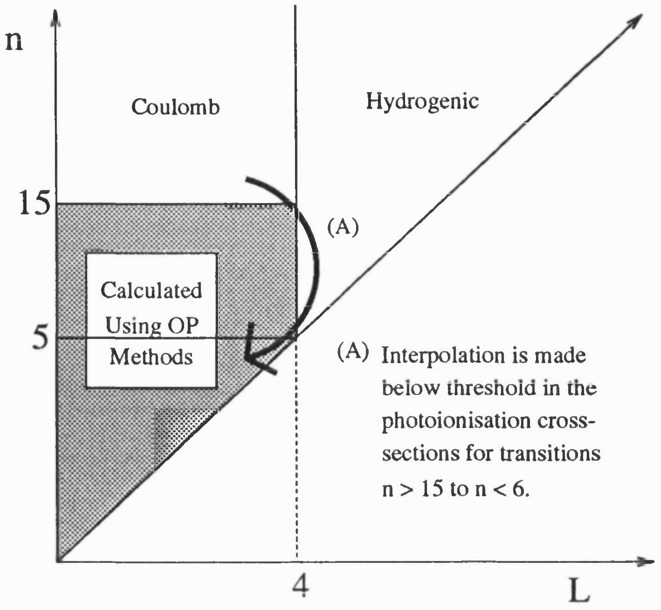

Figure 5.1: The division of the approximations used to calculate spontaneous radiative transition probabilities, as a function of n and L.

quantum numbers, $n \leq 15$ and total orbital angular momenta, $L \leq 4$, a total of 127 states. The weighted oscillator strengths were calculated using STGBB, part of the OP suite of codes, from the D and B datasets produces by running the codes STG1, STG2, STGH and STGB (§2.6).

For the transition $a \rightarrow b$, the dimensionless oscillator strength $f(b,a)$ is given by, (Seaton, 1987),

$$f(b,a) = \frac{(E_b - E_a)\mathbf{S}(b;a)}{3g_a} \tag{5.3}$$

where

$$\mathbf{S}(b;a) = |(b||\mathbf{D}||a)|^2 \tag{5.4}$$

The dipole operator $\mathbf{D}$ is

$$\mathbf{D} = e\sum_n \mathbf{r}_n \tag{5.5}$$

where $\mathbf{r}_n$ is the coordinate of the ionic electron and the sum is over all electrons in the ion. The Opacity Project codes generate gf values given by Yu Yan *et al.* (1987),

$$gf(a,b) = f(b,a) \times g_a \tag{5.6}$$

This is positive for absorption, $E_b > E_a$, and the gf values are tabulated with b taken to be of even parity and a to be of odd parity. For $E_b < E_a$, the quantity tabulated is negative

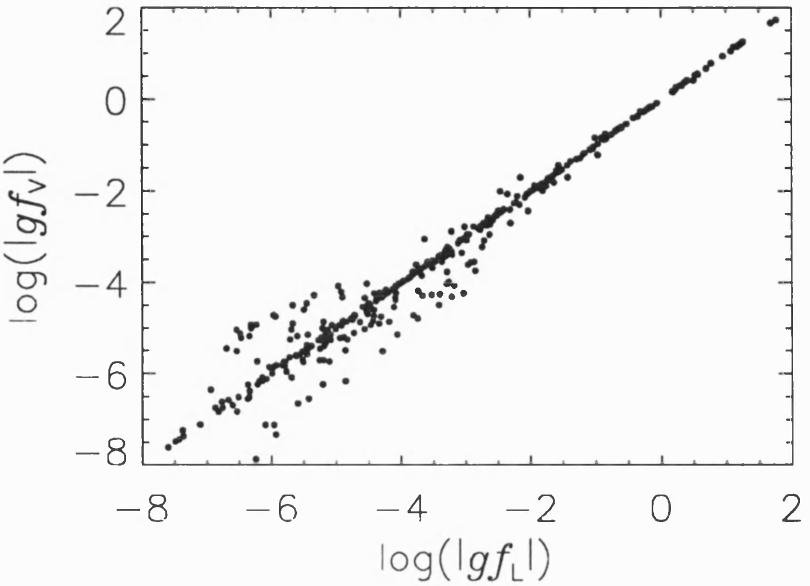

Figure 5.2: Comparison of *gf* values for gf_L and gf_V components, from dipole-length and dipole-velocity calculations.

and the *gf* values for the emission process $b \rightarrow a$ is given by

$$gf(a, b) = -gf(b, a) \tag{5.7}$$

The probability for spontaneous emission, $b \rightarrow a$ is,

$$A(b \rightarrow a) = \frac{\alpha^3 \tilde{\nu}^2}{2g_b} \times gf(a, b) \times \tau_0^{-1} \tag{5.8}$$

where $\alpha = e^2/(\hbar c)$, $\tilde{\nu}$ is the photon energy in rydbergs and $\tau_0^{-1} = \hbar^3/me^4$.

The f_L and f_V values are respectively, the oscillator strengths calculated using the length and velocity operators. All transition probabilities were calculated using gf_L values, calculated using the length operator. The variation between length and velocity values show the same trends noted by Yu Yan *et al.* (1987). Figure (5.2) gives a plot of $\log(|gf_L|)$ against $\log(|gf_V|)$. The agreement is generally good but there are discrepancies for small *gf* values.

Yu Yan *et al.* (1987) define the average percentage difference between gf_L and gf_V as,

$$100 \times \left(\sum (gf_L - gf_V)^2\right)^{\frac{1}{2}} \left(\sum (gf_L \times gf_V)\right)^{-\frac{1}{2}} \tag{5.9}$$

Table 5.1: Lifetimes of CII levels from the experimental work of Reistad *et al.* (1986) and calculated works of Yu Yan *et al.* (1987) and this thesis.

	Lifetime (ns)		
	Experimental	Calculated	
Level	Reistad	Yu Yan	This Work
$2s2p^2\ ^2S$	0.44± 0.02	0.42	0.44
$2s^23s\ ^2S$	2.4± 0.3	2.8	2.6
$2s^24s\ ^2S$	1.9± 0.1	2.2	2.0
$2s^25s\ ^2S$	3.7± 0.2	3.8	3.7
$2s2p^2\ ^2P$	0.25± 0.01	0.23	0.24
$2s^23p\ ^2P^0$	8.9± 0.4	9.2	8.6
$2s^24p\ ^2P^0$	3.8± 0.2	4.4	4.1
$2p^3\ ^2P^0$	0.48± 0.02	0.50	0.49
$2s^25p\ ^2P^0$	5.2± 0.3	5.0	5.1
$2s^23d\ ^2D$	0.34± 0.01	0.35	0.34
$2s^24d\ ^2D$	0.75± 0.03	0.73	0.72

which they find equal to 3.7%. The same formula gives 0.9% for the current calculations. However direct comparison is not possible. The difference may in part, be explained by the changes in the values of the R-matrix parameters, but it is more readily explained by noting that the weighted oscillator strengths calculated here contain no quartet states. Where the energy, ΔE_{obs} of a transition is known from experiment, the Opacity Project value gf_{OP} is corrected according to

$$gf_{corr} = gf_{OP}\frac{\Delta E_{obs}}{\Delta E_{cal}} \tag{5.10}$$

where ΔE_{cal} is the calculated transition energy. This correction removes any error in the value of gf due to errors in the calculated transition energy. Transition probabilities are then calculated from (5.8) using experimental energies where available.

Also of interest, is the comparison of the total lifetimes of various states, where direct comparison is possible. The probability for spontaneous emission $b \rightarrow a$ is given by (5.8). The total radiative probability is

$$A(b) = \sum_a A(b \rightarrow a) \tag{5.11}$$

with a summed over all lower states, and the lifetime of level b is

$$\tau_b = 1/A(b) \tag{5.12}$$

The comparison between Yu Yan *et al.* (1987) and Reistad *et al.* (1986) is reproduced here for the length components. The results in nearly all cases, fall within the experimental error.

5.2.2 Coulomb Approximation

A coulomb approximation to the radial transition integrals, based on van Regemorter *et al.* (1979) and Bates and Damgaard (1949), was used to generate transition probabilities, $\nu, \nu' \geq 16; L \leq 3$ and for transitions from states, $\nu' \geq 16 \rightarrow \nu \geq 6; L \leq 3$. Solutions to the radial integrals

$$R_{\nu l}^{\nu' l'} = \int_c^\infty P_{\nu l} P_{\nu' l'} \tag{5.13}$$

are required between all states of ^{1}S parentage for any value of the effective quantum number, for which there is available quantum defect data.

In the coulomb approximation the radial wave functions are solutions of

$$\left(\frac{d^2}{dr^2} - \frac{l(l+1)}{r^2} + \frac{2}{r} - \frac{1}{\nu^2}\right) P_{\nu l}(r) = 0 \tag{5.14}$$

As noted by Bates and Damgaard (1949) and Burgess and Seaton (1960) the variation of the radial integrals $R_{\nu l}^{\nu' l'}$, for fixed values of $\Delta\nu = \nu' - \nu, l, l'$, with ν (or ν') is very slow. This allows one of the quantum numbers to be an integer and the results to be obtained accurately by interpolating different calculations for the same value of $\Delta\nu$.

Therefore, one of the functions is expanded using the asymptotic expansions of the Whittaker function, given by Bates and Damgaard (1949)

$$P_{\nu l} = K_{\nu l} \left(\frac{2r}{\nu}\right)^{\nu} e^{-r/\nu} \sum_{t=0}^{t_0} b_t(\nu l) r^{-t} \tag{5.15}$$

the other being taken to be $P_{n' l'}$, the hydrogenic form. The radial integral has the form

$$\begin{aligned} R_{\nu l}^{n' l'} &= (-1)^{n'+l+1} \frac{1}{\nu n'} \frac{1}{(2l'+1)!} \left(\frac{\Gamma(n'+l'+1)}{\Gamma(\nu+l+1)\Gamma(\nu-l)\Gamma(n'-l')}\right)^{\frac{1}{2}} \\ &\times \left(\frac{2}{n'}\right)^{l'+1} \left(\frac{2}{\nu}\right)^{\nu} \sum_{t=0}^{t_0} b_t(\nu l) I_t \end{aligned} \tag{5.16}$$

with

$$\begin{aligned} I_t &= \int_0^\infty \exp\left[-r\left(\frac{1}{n'} + \frac{1}{\nu}\right)\right] r^{\nu+l'+2-t} {}_1F_1\left(-n' + l' + 1, 2l' + 2, \frac{2r}{n'}\right) dr \\ &= \Gamma(\nu + l' + 3 - t) \left(\frac{n'\nu}{n' + \nu}\right)^{\nu+l'+3-t} \\ &\times \; {}_2F_1\left(-n' + l' + 1, \nu + l' + 3 - t; 2;' + 2; \frac{2\nu}{n' + \nu}\right) \end{aligned} \tag{5.17}$$

using the Laplace transform of the confluent hypergeometric function.

Application of (5.17) reduces to the repeated calculation of the hypergeometric polynomial

$$F(\alpha,\beta;\gamma;x) = 1 + \frac{\alpha\beta}{\gamma}\frac{x}{1!} + \frac{\alpha(\alpha+1)\beta(\beta+1)}{\gamma(\gamma+1)}\frac{x^2}{2!} + \ldots \tag{5.18}$$

where α is a negative integer. For $(-\alpha) \leq 15$, the direct calculation of $F(\alpha,\beta;\gamma;x)$ using (5.18) is difficult due to the addition of terms of opposite sign that are large in comparison to the function itself. However $F(\alpha,\beta;\gamma;x)$ may be calculated easily using the following recurrence relation.

$$\begin{aligned}(\alpha-\gamma)F(\alpha-1,\beta;\gamma;x) + [\gamma-\alpha-\beta+(\beta-\alpha)(1-x)]& \\ F(\alpha,\beta;\gamma;x) + \alpha(1-x)F(\alpha+1,\beta;\gamma;x) &= 0 \end{aligned} \tag{5.19}$$

Knowledge of two initial values of the function, $F(0,\beta;\gamma;x) = 1$ and $F(-1,\beta;\gamma;x) = 1-(\beta/\gamma)x$, means that $F(\alpha,\beta;\gamma;x)$ can be calculated for arbitrary negative integer values of α by repeated application of (5.19).

With regard to the summation over t in (5.15), an analogous procedure is used to determine $F(-n^{'}+l^{'}+1, \nu+l^{'}+3-t; 2l^{'}+2; 2\nu/(n^{'}+\nu))$. For $t=0$ and $t=1$ the function is calculated using relation (5.18); for $2 \leq t \leq t_0$, the function is evaluated using

$$\begin{aligned}(\gamma-\beta)F(\alpha,\beta-1;\gamma;x) + (2\beta-\gamma-\beta x+\alpha x)& \\ F(\alpha,\beta;\gamma;x) + \beta(x-1)F(\alpha,\beta+1;\gamma;x) &= 0 \end{aligned} \tag{5.20}$$

Summarising,

$$\begin{aligned} F(0,\beta;\gamma;x) &= 1 \\ F(-1,\beta;\gamma;x) &= 1-(\beta/\gamma)x \end{aligned} \tag{5.21}$$

have to be calculated for $t=0$ and $t=1$. All other values of $F(\alpha,\beta;\gamma;x)$ may be deduced from (5.21) using (5.19) and (5.20).

The procedure for interpolation is detailed by Bates and Damgaard (1949). Let $c = \nu^{'}-\nu > 0$ with $n^{'} \leq \nu^{'} < n^{'}+1$ ($n^{'}$ being an integer) and $\nu_c = n^{'}-c$. In order to calculate the radial integral $R_{\nu l}^{\nu^{'}l^{'}}$, $R_{\nu_c l}^{n^{'}l^{'}}$ and $R_{\nu_c+1,l}^{n^{'}+1,l^{'}}$ must first be calculated using (5.16). Since the variation of

$$\mathcal{R}_{\nu_c+1,l}^{n^{'}+1,l^{'}} = R_{\nu_c+1,l}^{n^{'}+1,l^{'}}[\frac{3}{2}\nu_c(\nu_c^2-l_>^2)^{\frac{1}{2}}]^{-1} \tag{5.22}$$

with ν_c (or $n^{'}$) is very slow for a fixed value of c, linear interpolation is sufficient to determine $\mathcal{R}_{\nu_c+1,l}^{n^{'}+1,l^{'}}$ and

$$R_{\nu l}^{\nu^{'}l^{'}} = \frac{3}{2}\nu(\nu^2-l_>^2)^{\frac{1}{2}}\mathcal{R}_{\nu l}^{\nu^{'}l^{'}} \tag{5.23}$$

where $l_> = \max(l, l')$.

From Bates and Damgaard (1949), the spontaneous transition probability, A, can be expressed in terms of the line strength **S**.

$$A = \frac{64\pi^4}{3h}\frac{1}{g_2\lambda^3}\mathbf{S} \quad (s^{-1}) \tag{5.24}$$

Evaluation of A depends of upon the evaluation of **S**. It can be shown that

$$\mathbf{S} = \mathcal{J}(\mathcal{M})\mathcal{J}(\mathcal{L})R_{\nu l}^{\nu' l' 2} \tag{5.25}$$

where $\mathcal{J}(\mathcal{M})$ is a a factor depending on the particular multiplet of the transition array, $\mathcal{J}(\mathcal{L})$ is a factor depending on the particular line of the multiplet and $R_{\nu l}^{\nu' l'}$ is the derived solution to the radial integral.

When the program to obtain the population of a state was run in a normal mode, only the routine based on van Regemorter *et al.* (1979) was used. However when testing the code, calculations were performed, for which the code uses the methods of Bates and Damgaard (1949) directly. The swap over between the two methods was originally set at $n = 17$, but investigation showed that the transition probabilities produced involving states with $n = 17$ were very unstable. The asymptotic expansions of the wave functions, contain large oscillating terms which when summed caused a loss of precision due to cancellation, despite using double precision arithmetic. The stability was improved by sorting the terms of the sum using a routine coded by Lynas-Gray (1991). This proved beneficial for $n \leq 15$ but the Bates and Damgaard (1949) routine still proved too unstable at $n = 16$ and the swap over to using the van Regemorter *et al.* (1979) code was lowered to this value of n.

5.2.3 Hydrogenic Approximation

Brocklehurst (1971), details the evaluation of spontaneous transition probabilities, $A_{nl,n'l'}$, for electric dipole radiation in a hydrogenic approximation.

$$A_{nl,n'l'} = \frac{64\pi^4\tilde{\nu}^3}{Z^2 3hc^3}\frac{l_>}{(2l+1)}e^2a_0^2\left[\int_0^\infty R(n'l')rR(nl)dr\right]^2 \tag{5.26}$$

where

$$a_0 = \frac{\hbar^2}{me^2} \tag{5.27}$$

and where

$$\tilde{\nu} = cRZ^2\left(\frac{1}{n'^2} - \frac{1}{n^2}\right) \tag{5.28}$$

is the frequency of the transition $n'l' \rightarrow nl$ and $R(nl)$ is the normalised radial wave function. Substituting for $\tilde{\nu}$ in (5.26) and rearranging gives

$$A_{nl,n'l'} = 2.6774 \times 10^9 Z^4 a_{nl,n'l'} \tag{5.29}$$

where

$$a_{nl,n'l'} = \left(\frac{1}{n'^2} - \frac{1}{n^2}\right)^3 \frac{l_>}{(2l+1)} |\rho(n'l', nl)|^2 \tag{5.30}$$

and

$$\rho(n'l', nl) = \int_0^\infty R(n'l') r R(nl) dr. \tag{5.31}$$

The following expression (Gordon 1929) can be used to compute the integrals,

$$\begin{aligned} |\rho(n'l-1, nl)|^2 \ = \ & \left\{ \frac{(-1)^{n'-l}}{4(2l-1)!} \sqrt{\frac{(n+1)!(n'+l-1)!}{(n-l-1)!(n'-l)!}} \frac{(4nn')^{l+1}}{(n+n')^{n+n'}} \right. \\ \times \ & (n-n')^{n+n'-2l-2} \left[{}_2F_1\left(-n+l+1, -n'+l, 2l, \frac{-4nn'}{(n-n')^2}\right) \right. \\ - \ & \left. \left. \left(\frac{n-n'}{n+n'}\right)^2 {}_2F_1\left(-n+l-1, -n'+l, 2l, -\frac{4nn'}{(n-n')^2}\right) \right] \right\}^2 \end{aligned} \tag{5.32}$$

where ${}_2F_1$ is the hypergeometric function given by (5.18). The evaluation of the hypergeometric functions swaps from a cancellation to a recursive solution for n or n' greater than 200, since above 200 cancellation starts to lose precision. Hydrogenic transition probabilities were calculated for all states with $l, l' \geq 4$.

5.2.4 Below-threshold Photoionisation Cross-section Interpolation

For all states $n \leq 5$, the photoionisation cross-sections detailed in chapter 3, were extended below threshold, giving effectively bound-bound cross-sections. For transitions from all states, $n \geq 16$ to $n' \leq 5$, the transition probabilities were obtained by interpolating in these cross-sections at the final state energy. This was done using Lagrange interpolation. The transition probabilities will include the affects of configuration interaction and give much more accurate results than using either hydrogenic or coulomb approximations.

The relationship between the bound-bound oscillator strength and the bound-free oscillator strength at threshold is given, using effective quantum numbers, by Burgess and Seaton (1960),

$$(\nu l|r|\nu' l') = \frac{\nu^2}{z} \left[\frac{2}{\pi \xi(\nu', l') \nu'^3}\right]^{1/2} (-1)^{n'+l'+1} g\left(\nu l; \frac{1}{\nu'^2}, l'\right) \tag{5.33}$$

For large values of ν, it is usual to put $\xi(\nu) = 1$. Writing $g(\nu l; \epsilon', l')$ in terms of bound state and final state radial functions,

$$g(\nu l; \epsilon', l') = \frac{z^2}{\nu^2} \int_0^\infty P_{\nu l}(r) r G_{k'l'}(r) dr \tag{5.34}$$

where $\epsilon' = (k'/z)^2$. The generalized line strength S for a single transition is given by,

$$\frac{\mathbf{S}}{\omega} = C_{l'} \left| \int_0^\infty P_{\nu l}(r) r G_{k'l'}(r) dr \right|^2 \tag{5.35}$$

where ω is the statistical weight of the initial state of the atom and $C_{l'}$ are algebraic factors obtained from the integrations over spin and angular coordinates. Squaring (5.33) and substituting for (5.34) in (5.35) gives,

$$(\nu l|r|\nu' l')^2 = \frac{2z^2}{\pi \nu'^3} \frac{\mathbf{S}}{\omega} \frac{1}{C_{l'}} \tag{5.36}$$

The photoionisation cross-section at threshold, $a_{\tilde{\nu}}$ where $\tilde{\nu}$ is the frequency, may be written in terms of the generalised line strength as follows.

$$a_{\tilde{\nu}} = \frac{4\pi\alpha a_0^2}{3} \frac{z^2}{\nu^2} \frac{\mathbf{S}}{\omega} \tag{5.37}$$

The bound-bound oscillator strength can be written, in terms of the threshold cross-section,

$$(\nu l|r|\nu' l')^2 = \frac{3\nu^2 a_{\tilde{\nu}}}{2\pi^2 \nu'^3 \alpha a_0^2 C_{l'}} \tag{5.38}$$

By analogy to equation (5.35), a bound-bound line strength can also be written,

$$\frac{\mathbf{S}}{\omega} = C_{l'} \left| \int_0^\infty P_{\nu l}(r) r P_{\nu' l'}(r) dr \right|^2 \tag{5.39}$$

Equating (5.37) and (5.38), putting $f = (\nu l|r|\nu' l')^2$ and using (5.3), the bound-bound oscillator strength written in terms of the photoionisation cross-section is given by,

$$f = \frac{z^2}{\nu'^3} \frac{mc}{\pi a_0 h} a_{\tilde{\nu}} \tag{5.40}$$

This relationship is assumed to hold generally. The spontaneous radiative transition probability is then given by (5.8).

5.3 Collisional Transition Rates

Collisional transition rates are required between all states, $n \leq NLIM$. Rates are evaluated for energy and angular momentum changing collisions and for collisional ionisation and three body recombination. Account must also be taken of collisions to and from states for which $n > NLIM$. Energy changing collision rates are divided into two regions which are evaluated separately. These are firstly, collisions for which $|n' - n| = 1$ and secondly collisions for which $|n' - n| > 1$.

5.3.1 Angular Momentum Changing Collisions

A collision rate for the redistribution of angular momentum, $C_{l,l'}$ is defined such that

$$C(l,l') = \int Q(l,l')vf(v)dv \tag{5.41}$$

where $f(v)$ is the Maxwellian velocity distribution and $Q(l,l')$ is the collision cross-section. From detailed balancing considerations,

$$g_l C(l,l') = g_{l'} C(l',l) \tag{5.42}$$

where g is the statistical weight of the state.

The collision cross-section is evaluated in two approximations. For transitions up to and including $l = 4$, the semi-classical impact parameter method of Seaton (1962), which is suited to calculating reaction rates between states of small energy separation, is used.

The cross-section for excitation by a particle of charge Z and velocity v in the Born approximation is given by

$$Q_1(l,l') = \int_0^\infty P_{l'l}(R_l) 2\pi R_l dR_l \tag{5.43}$$

where R_l is the impact parameter of the state l and is the classical distance of closest approach and $P_{ll'}(R_l)$ is the probability that the $l \rightarrow l'$ transition occurs.

The assumptions made in the Born approximation, will be valid at all energies for $R_l \gg r_\alpha$ where r_α is comparable with atomic energies but will overestimate the low energy contributions from small impact parameters $R_l \lesssim r_\alpha$.

The impact parameter approximation considers only optically allowed transitions for which the cross-sections will come from quite large impact parameters. In this region the Born approximation is valid and so a cut-off is introduced into (5.43) to obtain

$$Q_1(l,l') = \int_{R_0}^\infty P_{l'l}(R_l) 2\pi R_l dR_l \tag{5.44}$$

Expressions for $P_{l'l}(R_l)$ can be simplified in the limit of R_l large, corresponding to the Bethe approximation (Seaton, 1955). Simpler expressions are obtained using the semi-classical impact parameter method and the two methods give good agreement at high energies. At lower energies, the semi-classical theory will be in error since it gives large departures from the reciprocity condition, $P_{l'l}(R_l) = P_{ll'}(R_{l'})$. A symmetrized semi-classical expression is used which gives good agreement with the Bethe approximation. Thus two parameters are used in the calculation of $Q(l,l')$ in the impact parameter approximation.

In the first equation (5.43), $P_{l'l}$ is evaluated using the symmetrized semi-classical theory and R_0 is taken to be independent of energy and agrees with the Bethe approximation in the limit of high energies. R_0 is comparable with atomic dimensions. For $R \geq R_0$

$$P(R) = \frac{4Z^2e^2}{3\hbar^2}\frac{\mathbf{S}}{R^2v^2}\xi(\beta) \tag{5.45}$$

where

$$\mathbf{S} = e^2|(l|\mathbf{r}|l')|^2 \tag{5.46}$$

is the line strength of the optically allowed transition and

$$\beta = \frac{R\Delta E}{\hbar v} \tag{5.47}$$

ΔE is the energy difference between the initial and final states. $\xi(\beta)$ is tabulated in Seaton (1962). For $R_l > R_0$, the values of $P_{l'l}(R_l)$ should be fairly accurate assuming the coupling is weak. A necessary condition is that $P_{l'l} \leq 1$. In the regime of stronger coupling, the $P_{l'l}$, calculated assuming weak coupling, are taken to be adequate, so long as they give $P_{l'l} \leq \frac{1}{2}$ (Seaton, 1961). When the coupling is strong, a value of R_1=R_l is used so that the weak coupling theory gives

$$P_{l'l}(R_1) = \frac{1}{2} \tag{5.48}$$

For $R_l < R_1$, $P_{l'l}$ is considered to be an oscillatory function with a mean value of $\frac{1}{2}$ and the cross-section is taken to be,

$$Q(l,l') = \frac{1}{2}\pi R_1^2 + \int_{R_1}^{\infty} P_{l'l}(R_l)2\pi R_l dR_l \tag{5.49}$$

Both cross-sections, given by (5.43) and (5.49) are calculated and the smaller of the two adopted, in the calculation of the collision rate.

For degenerate states, $\Delta E = 0$ and the integral in (5.44) varies as R^{-1} and is therefore divergent, which would give an infinite value for the cross-section in this case. The method of Pengelly and Seaton (1964) is used, which introduces an upper cut-off in the impact parameter to obtain finite cross-sections. In the degenerate case and in cases where ΔE is very small, it is plausible to neglect the contribution from $R \gtrsim \tau v$ where τ is the radiative lifetime. This gives

$$Q_1 \simeq \frac{8\pi Z^2e^2\mathbf{S}}{3\hbar}\ln(\tau v/R_1) \tag{5.50}$$

At large impact parameters,

$$Q_1 = \frac{8\pi Z^2e^2\mathbf{S}}{3\hbar v^2}\ln(R_c/R_1) \tag{5.51}$$

where it is assumed that $R_c \gg R_1$ and the following procedures are used to determine the cut-off, R_c.

If the initial and final states have an energy difference that is wide compared to the line widths, $\hbar/\tau$,

$$R_c = \frac{1.12\hbar\tau}{\Delta E} \tag{5.52}$$

For $\Delta E \ll \hbar/\tau$, there is a possibility that the collisional process will be interrupted by the target electron radiating. In this case the cut-off is taken to be,

$$R_c = 0.72v\tau \tag{5.53}$$

In an ionised gas, the particle positions are not entirely uncorrelated. The electrons tend to cluster around positive ions and the effective range of the Coulomb field of the ions is then determined by the Debye radius,

$$R_D = \left[\frac{kT_e}{4\pi e^2 N_e}\right]^{\frac{1}{2}} \tag{5.54}$$

In practice, all cut-offs were evaluated and the smallest expression for R_c was adopted. At very low densities, the cut off will be determined by the radiative lifetime of the excited states. At higher densities, it will be determined by the Debye radius.

For small impact parameters, $R_1 \leq R \leq R_c$,

$$P(R) = \frac{4Z^2e^2\mathrm{S}}{3\hbar^2 R_1^2 v^2} \tag{5.55}$$

The conservation condition is $P(R) \ll 1$. R_1 is defined by

$$\frac{4Z^2e^2\mathrm{S}}{3\hbar^2 R_1^2 v^2} = \frac{1}{2} \tag{5.56}$$

This is valid if R_1 is large compared to atomic dimensions. For $R < R_1$, $P(R)$ will be an oscillatory function with a mean value close to $\frac{1}{2}$. Taking $P(R) = \frac{1}{2}$ for $R \leq R_1$,

$$Q = \pi R_1^2\{\frac{1}{2} + ln(R_c/R_1)\} \tag{5.57}$$

where

$$R_1^2 = \frac{8Z^2e^2\mathrm{S}}{3\hbar^2 v^2} \tag{5.58}$$

The lifetime of each state is calculated in the evaluation of the radiative transition probabilities to lower states and passed to the routines calculating collisional rate coefficients. The impact parameter method is used for collisions involving states for which quantum defect data exists and the method of Pengelly and Seaton (1964) otherwise.

5.3.2 Energy Changing Collisions: $\Delta n = 1$

For transitions of the type $n \rightarrow n \pm 1$, the energy differences will be small and a large contribution to the the cross-sections will come from impact parameters $R > R_1$. This lends itself to calculation using the impact parameter approximation. The cross-sections generated are very accurate in this case and the approximation was used for all l.

It should be noted that the codes used to generate rates using the impact parameter approximation, did so only for transitions $l \rightarrow l + 1$. In the case of angular momentum changing collisions, the principle of detailed balance was used to obtain the reverse rates. For energy changing collisions, the rates were calculated for $l \rightarrow l+1$ and $n \rightarrow n+1$ and the reverse rates again obtained from detailed balance. The code as it stands cannot calculate the cross rates. Other work has approximated these rates by means of a fixed ratio to the $l \rightarrow l + 1$, $n \rightarrow n + 1$ rates, but the assignment of the ratio seems to be arbitrary. One possible means of obtaining these rates is to compare the oscillator strengths for the various transitions, since the collisional cross-sections are proportional to the line strengths. However this was not done, since it was found that at high l the rates are small in comparison to the $l \rightarrow l + 1$ rates and that at densities where $\Delta n = 1$ transitions are important, full collisional redistribution of a particular level will have occurred via the angular momentum changing collisions. In such a case is not important which l value the population is deposited in since the states will be populated according to their statistical equilibrium. The error in neglecting the cross rates is not significant.

5.3.3 Energy Changing Collisions: $\Delta n > 1$

For collisions $|n' - n| > 1$, electron impact rates were evaluated from semi-empirical cross-sections using the methods described by Percival and Richards (1978) who give the cross-section in the form,

$$\frac{Z^2 \bar{E} \sigma(n \rightarrow n')}{n^4 \pi a_0^2} = ADL + FGH \tag{5.59}$$

where $\bar{E}$ is the incident electron energy per Rydberg, and Z is the effective charge. ADL is the high energy term, $\bar{E} > 2Z/n$ and contains quantal effects, in particular the logarithmic dependence of the cross-section on energy. The factor A is proportional to the optical oscillator strength which scales as Z^{-2}, but A itself is unchanged. The factor D is simply a cut-off, which removes the quantal energy terms, which will be negligible in the region where the cross-section is an increasing function of energy and where the dominant contribution to the rate arises.

The function L has the form

$$L(\bar{E}) = \ln\left[\frac{1+(\bar{E}/E_1)^2}{1+(\bar{E}/E_2)}\right] \tag{5.60}$$

and E_1, E_2 are chosen to ensure the cross-section has the correct form in the high energy region, $\mathcal{A}$, which is $\bar{E} > 1$ and in the intermediate region $\mathcal{B}$, where $2Z/n < \bar{E} < 1$.

The second term, FGH has no logarithmic dependence on energy and is purely a classical term. The factor F is related to the charge, through the cut-off factor D, and remains unchanged in form. The factors G and H come from Percival (1973) and from the density of states correspondence principle. Hence the various factors given in equation (5.59) are,

$$\begin{aligned}
A &= \frac{8}{3s}\left(\frac{n'}{sn}\right)^3 (0.184 - 0.04/s^{\frac{2}{3}})\left(1-\frac{0.2s}{nn'}\right)^{1+2s} \\
s &= n' - n > 0 \\
D &= \exp[-Z^2/(nn'\bar{E}^2)] \\
L(\bar{E}) &= \ln\left[\frac{1+0.53\bar{E}^2 nn'/Z}{1+0.4\bar{E}}\right] \\
F &= [1-0.3sD/(nn')]^{1+2s} \\
G &= \frac{1}{2}\left(\frac{\bar{E}n^2}{Zn'}\right)^3 \\
H &= C_2(x_-,y) - C_2(x_+,y) \\
C_2(x,y) &= \frac{x^2\ln(1+2x/3)}{2y+3x/2} \\
x_\pm &= 2Z/[n^2\bar{E}(\sqrt{2-n^2/n'^2} \pm 1)] \\
y &= \left[1-\frac{D\ln(18s)}{4s}\right]^{-1}
\end{aligned} \tag{5.61}$$

The de-excitation rates are given by detailed balance arguments. Percival and Richards (1978) give the condition that the range of quantum numbers are limited such that,

$$s = n' - n > 0, \qquad n', n \geq 5 \tag{5.62}$$

In this thesis this limit of n, n' is extended down to include $n \geq 3$ levels. The errors that might arise from including transitions to $n, n' = 3$ are less than the error in not including any approximation for these levels, particularly at high density. However, Percival and Richards (1978) noted that at low temperatures their may be as much as a 20% error in the rate. For this reason at temperatures of less that 1000 K, the original limits were applied.

5.3.4 Collisional Ionisation / 3-body Recombination

The binary encounter method (Burgess and Percival, 1968) is used to evaluate collisional ionisation and three body recombination coefficients. Storey (1972) gives the following result for the differential cross-section,

$$\begin{aligned}\frac{\partial Q}{\partial \varepsilon} &= \frac{\pi e^4}{E}\left[\left(\frac{1}{\varepsilon^2}+\frac{4}{3}\frac{E_2}{\varepsilon^3}\right)+\left(\frac{1}{(E+U-\varepsilon)^2}+\frac{4}{3}\frac{E_2}{(E+U-\varepsilon)^3}\right)\right.\\ &- \left.\frac{1}{(E+U)}\left(\frac{1}{\varepsilon}+\frac{1}{E+U-\varepsilon}\right)\right] \qquad (5.63)\end{aligned}$$

where E_2 is the initial kinetic energy of the target electron, $U = I_n$ is the binding energy of the target electron and a focusing factor to allow for the effect of the ion field has been incorporated. The cross-sections for energy transfers in the range $\varepsilon_1 < \varepsilon < \varepsilon_2$ is then given by,

$$Q(E) = \int_{\varepsilon_1}^{\varepsilon_2} \frac{\partial Q}{\partial \varepsilon}(\varepsilon) d\varepsilon \qquad (5.64)$$

The ionisation cross-section is obtained from equations (5.63) and (5.64), by putting $\varepsilon_1 = U$ and $\varepsilon_2 = \frac{E+U}{2}$. This gives

$$Q_i(E) = \frac{\pi e^4}{E}\left[\left(\frac{1}{U}-\frac{1}{E}\right)+\frac{2U}{3}\left(\frac{1}{U^2}-\frac{1}{E^2}\right)+\frac{\ln(E/U)}{E+U}\right] \qquad (5.65)$$

The ionisation coefficient is then given by,

$$\begin{aligned}\gamma(n,c) &= \frac{8\pi^2 e^4}{m^2}\left(\frac{m}{2\pi kT}\right)^{\frac{3}{2}}\left[\frac{\exp(-U/kT)}{U/kT}\left(\frac{5}{3}-\frac{2}{3}\frac{U}{kT}\right)\right.\\ &+ \left. E_1\left(\frac{U}{kT}\right)\left(\frac{2U}{kT}-1\right)-\frac{1}{2}\left(E_1\left(\frac{U}{kT}\right)\right)^2 \exp(U/kt)\right] \qquad (5.66)\end{aligned}$$

This expression was used to generate collisional ionisation and three body recombination coefficients for all states based on their principal quantum number. Quantum defect data was used where available.

5.4 The Relative Importance of Collisional Processes

The relative importance of collisional processes on the population of a state is primarily dependent on the density. It will also be dependent, to varying degrees, on the principle quantum number and more especially the angular momentum of the state. For states with high L, collisional processes become important at relatively low densities since the radiative decay rates from the state will be small. This is illustrated by figure (5.3), where the relative importance of radiative processes and the primary collisional processes,

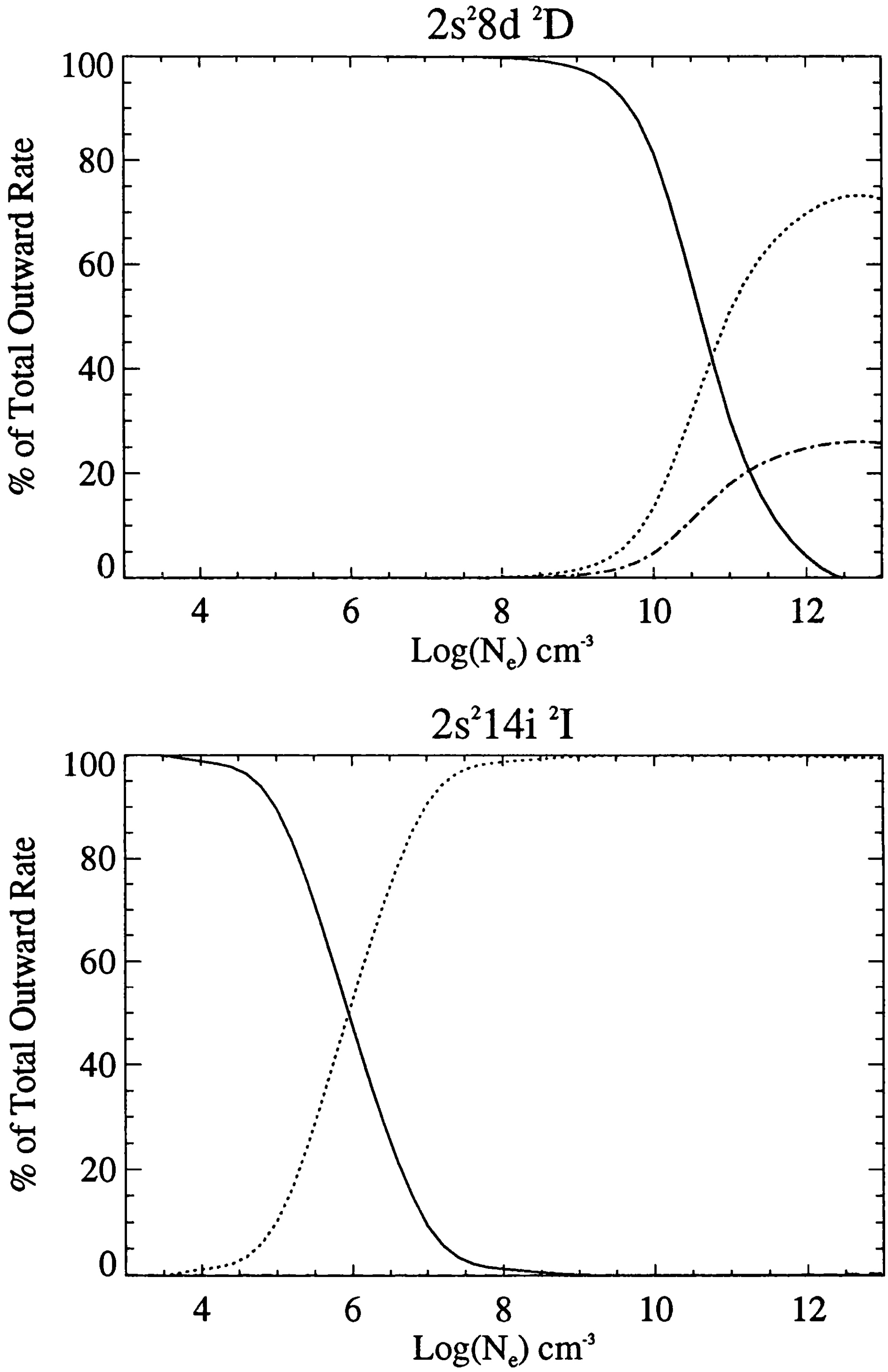

Figure 5.3: The relative importance of radiative and collisional processes in the depopulation of the $2s^28d\ ^2D$ and $2s^214i\ ^2I$ states as a function of density. The solid line represents the total radiative decay rate from the state, the dotted line the angular momentum depopulation rate and the dashed line the energy changing collision rate for $\Delta n = 1$.

angular momentum changing and energy changing ($\Delta n = 1$) collisions, are given as a percentage of the total outgoing rate from a state versus density.

Figure (5.3) shows that the $2s^28d\ ^2D$ depopulation is dominated by radiative decay up to a density of $\sim 10^9$ cm^{-3}. However for the $2s^214i\ ^2I$ state, the point at which radiative decay no longer dominates the depopulation is at a density of $\sim 10^5$ cm^{-3}. In the two cases there is also a marked difference in the importance of $\Delta n = 1$ changing collisions though this is not surprising since the oscillator strengths for the transitions at low L will be much larger.

The collisional ionisation and three body recombination rates are small in comparison to the angular momentum and energy changing ($\Delta n = 1$) rates, but importantly link a state to the continuum. At high density collisional ionisation will be the dominant ionising rate.

5.5 Equilibrium Level Population Equations

Consider an excited state nl. In a radiative equilibrium, the state will be populated by radiative recombination and by radiative cascade from higher levels, and depopulated by radiative decay to lower levels. The rate of population is given by

$$N_eN_+\alpha_{nl} + \sum_{n'=n+1}^{\infty} \sum_{l'=l\pm1} N_{n'l'}A_{n'l';nl} \tag{5.67}$$

where N_e and N_+ are the electron and ion densities respectively, α_{nl}, is the total radiative recombination coefficient to the state, $A_{n'l';nl}$ is the spontaneous radiative transition probability from the higher state and $N_{n'l'}$ is its population. The depopulation rate, due to radiative cascade, is given by

$$N_{nl} \sum_{n'=n_{min}}^{n'=n-1} \sum_{l'=l\pm1} A_{nl;n'l'} \tag{5.68}$$

Equating (5.67) and (5.68), a radiative equilibrium equation is obtained, given by

$$N_{nl} \sum_{n'=n_{min}}^{n'=n-1} \sum_{l'=l\pm1} A_{nl;n'l'} = N_eN_+\alpha_{nl} + \sum_{n'=n+1}^{\infty} \sum_{l'=l\pm1} N_{n'l'}A_{n'l';nl} \tag{5.69}$$

In a region of increased density, the population of a state will be affected by collisional process. The collisional population rate is given by,

$$N_+N_e\alpha^3_{nl} + \sum_{l'=l\pm1} N_{nl'}C_{l'l} + \sum_{\substack{n'=n\pm1 \\ l'=l\pm1}} N_{n'l'}C_{n'l';nl} + \sum_{n'=n_{min}}^{\infty} N_{n',l+1}C_{n';nl}\delta_{nn'} \tag{5.70}$$

$$\delta_{nn'} = \begin{cases} 1 & |n' - n| \geq 2 \\ 0 & |n' - n| < 2 \end{cases} \tag{5.71}$$

where $C_{l'l}$ is a l-changing collision rate ($\Delta n = 0$), $C_{n'l';nl}$ is an energy changing collision rate ($\Delta n = 1$) and α^3_{nl} is the three-body recombination coefficient. $C_{n';nl}$ is an energy changing collision rate ($\Delta n \geq 2$) which is independent of l. For equilibrium purposes these collisions are assumed to be to $l + 1$ for $n'_{>}$ and to $l - 1$ for $n'_{<}$. Similarly, the rate of collisional depopulation is given by,

$$N_{nl}\left(\sum_{l'=l\pm1} C_{ll'} + \sum_{\substack{n'=n\pm1\\ l'=l\pm1}} C_{nl;n'l'} + \sum_{n'=n_{min}}^{\infty} C_{nl;n'}\delta_{nn'} + C^I_{nl}\right) \tag{5.72}$$

where C^I_{nl} is the collisional ionisation rate. Equating (5.70) and (5.72) the density dependent equilibrium equation is written,

$$N_{nl}\left(\sum_{l'=l\pm1} C_{ll'} + \sum_{\substack{n'=n\pm1\\ l'=l\pm1}} C_{nl;n'l'} + \sum_{n'=n_{min}}^{\infty} C_{nl;n'}\delta_{nn'} + C^I_{nl}\right) =$$

$$N_+N_e\alpha^3_{nl} + \sum_{l'=l\pm1} N_{nl'}C_{l'l} + \sum_{\substack{n'=n\pm1\\ l'=l\pm1}} N_{n'l'}C_{n'l';nl} + \sum_{n'=n_{min}}^{\infty} N_{n',l+1}C_{n';nl}\delta_{nn'} \tag{5.73}$$

Combining equations (5.69) and (5.73) the population of a state accounting for both radiative and collisional processes is given by the equilibrium equation,

$$N_{nl}\left(\sum_{n'=n_{min}}^{n'=n-1}\sum_{l'=l\pm1} A_{nl;n'l'} + \sum_{l'=l\pm1} C_{ll'} + \sum_{\substack{n'=n\pm1\\ l'=l\pm1}} C_{nl;n'l'} + \right.$$

$$\left.\sum_{n'=n_{min}}^{\infty} C_{nl;n'}\delta_{nn'} + C^I_{nl}\right) = N_eN_+\alpha_{nl} + \sum_{n'=n+1}^{\infty}\sum_{l'=l\pm1} N_{n'l'}A_{n'l';nl} +$$

$$N_+N_e\alpha^3_{nl} + \sum_{l'=l\pm1} N_{nl'}C_{l'l} + \sum_{\substack{n'=n\pm1\\ l'=l\pm1}} N_{n'l'}C_{n'l';nl} + \sum_{n'=n_{min}}^{\infty} N_{n',l+1}C_{n'nl}\delta_{nn'} \tag{5.74}$$

It is useful to rewrite the true population in terms of the Local Thermodynamic Equilibrium (LTE) population, N^s_{nl}.

$$N_{nl} = N^s_{nl}b_{nl} \tag{5.75}$$

Here, b_{nl} is a dimensionless parameter which measures the departure of the state, from its LTE population, obtained from the Saha equation.

$$\frac{N^s_{nl}}{N_eN_+} = \frac{g_{nl}}{2g_+}\left(\frac{h^2}{2\pi mkT}\right)^{\frac{3}{2}} e^{\chi_n} \tag{5.76}$$

where $g_{nl} = (2S+1)(2l+1)$ and χ_n is the ionisation energy of the state. Writing $S(T) = 2.0706470 \times 10^{-16} T^{-\frac{3}{2}}$, the Saha equation can be written,

$$\frac{N^s_{nl}}{N_e N_+} = g_{nl}\, S(T)\, e^{\chi_n} \tag{5.77}$$

Using equations (5.75) and (5.77) and writing

$$A^T_{nl} = \sum_{n'=n_{min}}^{n'=n-1} \sum_{l'=l\pm1} A_{nl;n'l'} \tag{5.78}$$

the equilibrium equation (5.74) can be rewritten,

$$\begin{aligned}
g_{nl} S(T) e^{\chi_n} b_{nl} & \left(A^T_{nl} + \sum_{l'=l\pm1} C_{ll'} + \sum_{\substack{n'=n\pm1 \\ l'=l\pm1}} C_{nl;n'l'} + \sum_{n'=n_{min}}^{\infty} C_{nl;n'} \delta_{nn'} + C^I_{nl} \right) \\
&= \alpha_{nl} + \alpha^3_{nl} \\
&+ \sum_{n'=n+1}^{\infty} \sum_{l'=l\pm1} g_{n'l'} S(T) e^{\chi_{n'}} b_{n'l'} A_{n'l';nl} + \sum_{l'=l\pm1} g_{nl'} S(T) e^{\chi_n} b_{nl'} C_{l'l} \\
&+ \sum_{\substack{n'=n\pm1 \\ l'=l\pm1}} g_{n'l'} S(T) e^{\chi_{n'}} b_{n'l'} C_{n'l';nl} + \sum_{n'=n_{min}}^{\infty} g_{n'l'} S(T) e^{\chi_{n'}} b_{n'l'} C_{n';nl} \delta_{nn'}
\end{aligned} \tag{5.79}$$

Dividing by $g_{nl} S(T) e^{\chi_n}$ and writing

$$\alpha'_{nl} = \frac{\alpha_{nl}}{g_{nl} S(T) e^{\chi_n}}, \quad \alpha^{3'}_{nl} = \frac{\alpha^3_{nl}}{g_{nl} S(T) e^{\chi_n}}, \quad \text{and } T^{exp}_{nl} = g_{nl} e^{\chi_n} \tag{5.80}$$

then

$$\begin{aligned}
b_{nl} & \left(A^T_{nl} + \sum_{l'=l\pm1} C_{ll'} + \sum_{\substack{n'=n\pm1 \\ l'=l\pm1}} C_{nl;n'l'} + \sum_{n'=n_{min}}^{\infty} C_{nl;n'} \delta_{nn'} + C^I_{nl} \right) \\
&= \alpha'_{nl} + \alpha^{3'}_{nl} \\
&+ \sum_{n'=n+1}^{\infty} \sum_{l'=l\pm1} \frac{T^{exp}_{n'l'}}{T^{exp}_{nl}} b_{n'l'} A_{n'l';nl} + \sum_{l'=l\pm1} \frac{T^{exp}_{n'l'}}{T^{exp}_{nl}} b_{nl'} C_{l'l} \\
&+ \sum_{\substack{n'=n\pm1 \\ l'=l\pm1}} \frac{T^{exp}_{n'l'}}{T^{exp}_{nl}} b_{n'l'} C_{n'l';nl} + \sum_{n'=n_{min}}^{\infty} \frac{T^{exp}_{n'l'}}{T^{exp}_{nl}} b_{n'l'} C_{n';nl} \delta_{nn'}
\end{aligned} \tag{5.81}$$

and the value of the departure coefficient for the state can be obtained. Re-inserting b_{nl} into (5.75), gives the true population which will include the effects of radiative cascade. The T^{exp}_{nl} functions are only temperature dependent, so for each value of the temperature, the functions are calculated for all states and stored.

5.6 Evaluation of the Asymptotic Sums

Equation (5.81) contains asymptotic sums over incoming transition probabilities and both incoming and outgoing collisional rates for which $\Delta n > 1$. Consider the asymptotic sum $\sum_{n'=n+1}^{\infty} f(n')$. This can be written,

$$\sum_{n'=n+1}^{\infty} f(n') = \frac{1}{2} f(n+1) + \int_{n+1}^{\infty} f(n') dn' \tag{5.82}$$

Defining the function $f(n')$ such that,

$$f(n') = g_{n'l'} e^{\chi_{n'}} h(n'l'; nl) \tag{5.83}$$

where $h(n'l'; nl)$ is an arbitrary transition probability, $g_{n'l'}$ is a statistical weight and χ is the ionisation energy. Using $g_{n'l'} = 2(2l' + 1)$

$$\sum_{n'=n+1}^{\infty} f(n') = (2l' + 1) e^{\chi_{n+1}} h(n+1, l; nl) + \int_{n+1}^{\infty} g_{n'l'} e^{\chi_{n'}} h(n'l'; nl) dn' \tag{5.84}$$

Putting I equal to the integral part,

$$I = 2(2l' + 1) \int_{n+1}^{\infty} e^{\chi_{n'}} h(n'l'; nl) dn' \tag{5.85}$$

Transforming I, to be an integral over the energy variable ε where

$$\varepsilon = \frac{1}{n'^2}, \quad d\varepsilon = -\frac{2}{n'^3} dn' \quad \text{and} \quad dn' = \frac{n'^3}{2} d\varepsilon \tag{5.86}$$

then

$$I = -(2l' + 1) \int_{\varepsilon_{n+1}}^{0} n'^3 e^{\chi_{n'}} h(n'l'; nl) d\varepsilon \tag{5.87}$$

Converting to the range -1 to +1, i.e. putting

$$u = \frac{2\varepsilon}{\varepsilon_{n+1}} - 1, \quad \text{then} \quad du = \frac{2}{\varepsilon_{n+1}} d\varepsilon \quad \text{and} \quad d\varepsilon = \frac{\varepsilon_{n+1}}{2} du \tag{5.88}$$

Hence,

$$I = -\frac{(2l' + 1)}{2} \varepsilon_{n+1} \int_{1}^{-1} n'^3 e^{\chi_{n'}} h(n'l'; nl) du \tag{5.89}$$

and is in a form suitable for evaluation using Gauss-Laguerre quadrature. The asymptotic sum is given by

$$\begin{aligned} \sum_{n'n+1}^{\infty} f(n') &= (2l' + 1) e^{\chi_{n+1}} h(n+1, l'; nl) \\ &+ \frac{(2l' + 1)}{2} \int_{-1}^{+1} n'^3 e^{\chi_{n'}} h(n'l'; nl) du \end{aligned} \tag{5.90}$$

This form is used in the evaluation of radiative decays from states above NLIM onto a lower state. Since the main contribution will come from the first few states, the first ten are summed directly and the asymptotic sum evaluated for the rest.

Similarly Gauss-Laguerre quadrature is used for evaluating both outward and inward asymptotic collision integrals. In these cases the first fifty terms are evaluated directly and the remainder obtained by integration.

5.7 Solving the Equilibrium Level Population Equations

The notation of (5.81) assumes that each state can be uniquely described by its principal quantum number and its total angular momentum. For states of $2s^2(^1S)$ parents, this is true. However for states of other parents, ie. $2s2p(^3P^0,^1P^0)$ and $2p^2(^3P,\ ^1D,^1S)$, such a representation would not be unique, since the total angular momentum of the state is not equal to the angular momentum of the added electron.

In order to solve the problem of the unique identification of states, the region of solution was divided into two sections. These were the upper or high state region, which used an indexing scheme based on the principal quantum number and total angular momentum of a state, and the low state region where a list of states in energy order was created, and a unique state index, based on this list, determined.

5.7.1 The High State Region

The advantage of an indexing scheme based on the principle quantum number and the total angular momentum is its ability to directly relate calculated quantities to individual states. In this region only states with ^1S parents were considered. The approximations used were mainly hydrogenic or coulomb, and in the case of coulomb approximations, used values of quantum defects extrapolated from values at the boundary of the two regions.

5.7.2 The Low State Region

In the low state region an energy ordered list was created for all states, up to the boundary between the two regions, irrespective of their parent state. The input to the codes, generated to solve the level population equations, specified the parent states and their experimental energies, the energies of the lowest states in the series and all available quantum defect data. Quantum defect data was extrapolated, where it was missing, in the region $l \leq 4$. For states $L \geq 5$, hydrogenic (degenerate) energies were used. Related to the energy ordered index, was a cross reference to the OP indexes for CII. This enabled OP data, or data calculated using the OP suite of codes, such as weighted oscillator strengths to be easily incorporated into the program, with only the minimum need for reformatting. Use was made of both the existing OP data and subsequently, data recalculated using the OP suite of programs.

5.7.3 The Boundary Value: NMAX

NMAX was the chosen value of the principal quantum number, which divided the high and low state regions. Initially the value of NMAX was set at $n = 10$. All states higher in energy were taken to be representable by an nl indexing scheme, or neglected. However on testing, an anomaly was noted in the value of the departure coefficients for the 12s and 13s states. This was traced to very large transition probabilities for these states to lower lying ones ($n \leq 5$). The approximation used for calculating transition probabilities in this case, involved interpolation in below threshold photoionisation cross-sections (§5.2.4). The energy at which the interpolations in the appropriate cross-sections were being carried out, lay very close to the centre of a large resonance. This was subsequently identified as arising from the 2s2p3p ^{2}S state. This state had a far greater interaction through configuration mixing than was initially thought. A physically meaningful calculation would need to explicitly include this state. This was done by raising the boundary of the high/low state division to $n = 15$. This necessitated extending the photoionisation cross-section calculations for states in the region $11 \leq n \leq 15, L \leq 4$ and hence generating new recombination coefficients. New bound energy levels and oscillator strengths were also calculated. In order to facilitate testing, the program was designed so that the value of NMAX could be changed, so that high state methods of solution could be used all the way to the ground state, or as low a value of NMAX as required and similarly the low state methods could be used up to as high a value of NMAX as required. This was useful, not only in testing the accuracy of the code against known results, but also as an independent check on the consistency of the values calculated in the two regions. Tests were carried out on He^+ in order to fulfill these aims.

5.7.4 First Guess Hydrogenic Solutions

The determination of the population of states for which $n \leq NLIM$, will depend in part upon the evaluation of radiative decays on to the states from states above $NLIM$, and also collisional population and depopulation from and to states above $NLIM$.

In order to do this, some knowledge is required of the populations of the states above $NLIM$. First guess solutions to states, $N \leq NLIM$ and final solutions to states above $NLIM$ were made using hydrogenic b_{nl} values. These were obtained by solving the level population problem for the hydrogenic case using separate codes, (Storey, 1993). The codes are based on Hummer and Storey (1987), who gave definitive results for hydrogenic ions. All radiative and collisional processes were included, giving hydrogenic b_{nl} (departure coefficient) values at the appropriate temperature and density. For states up to a given principal quantum number, b_{nl} values were obtained for each value of l, at that value of n. Above this and up to $n = 500$ the population was assumed to be fully collisionally redistributed and $b_{nl} = b_n$. Above $n = 500$, b_n was taken to be one. Hydrogenic b_{nl} values will only exist for states of ^{1}S parents. For other states, an initial value of 0 was assumed.

5.7.5 Solutions in the High State Region

The equilibrium level population equation (5.81) is solved in the high state region, for all states from NLIM down to NMAX+1. We define an $n \times n$ array, P such that the diagonal elements are given by the sum of the total outgoing radiative and collisional rates. i.e.

$$P(l,l) = A^T_{nl} + \sum_{l'=l\pm1} C_{ll'} + \sum_{n'=n\pm1} \sum_{l'=l\pm1} C_{nl;n'l'} + \sum_{n'=n_{min}}^{\infty} C_{nn'}\delta_{nn'} + C^I_{nl} \tag{5.91}$$

and the adjacent off-diagonal elements, $P(l, l-1)$ and $P(l, l+1)$ are given by,

$$P(l,l-1) = \frac{2l-1}{2l+1}C(l-1,l) \text{ and } P(l,l+1) = \frac{2l+3}{2l+1}C(l+1,l) \tag{5.92}$$

Also, defining a one dimensional array Y of n elements, to be the sum of all incoming radiative and collisional rates to a state, the equilibrium equation can be written,

$$b_{nl}P(l,l) - b_{nl-1}P(l,l-1) - b_{nl+1}P(l,l+1) = Y_{nl} \tag{5.93}$$

or in matrix form

$$\underline{Pb} = \underline{Y} \tag{5.94}$$

This gives a band diagonal matrix from which solutions for b_{nl} in the high state region were obtained. The calculated b_{nl} values replaced the hydrogenic b_{nl} values in the first instance and then updated the values that were calculated in subsequent passes. These values were immediately used in the calculation of the next value of n. After solving for all high states, the radiative rates to lower states were evaluated and stored for passing to the low state region routine.

5.7.6 Solutions in the Low State Region

In the low state region, solutions for b_{IT}, where IT is the low state index, were obtained for all states simultaneously. The equilibrium equation is arranged in matrix form, where $P(IT, IT)$ contains the sum of all outgoing rates and $Y(IT)$ the sum of all incoming rates, as in the high state case. Because of the nature of the indexing scheme, in the low state region however, it is not only the adjacent off diagonal terms which may be non-zero. The off diagonal terms are defined such that

$$\begin{aligned} P(IT, JT) &= -\frac{T_{JT}^{exp}}{T_{IT}^{exp}} A_{JT,IT} - \frac{T_{JT}^{exp}}{T_{IT}^{exp}} C_{JT,IT}^{\Delta n=0} \\ &- \frac{T_{JT}^{exp}}{T_{IT}^{exp}} C_{JT,IT}^{\Delta n=1} - \frac{T_{JT}^{exp}}{T_{IT}^{exp}} C_{JT,IT}^{\Delta n>1} \end{aligned} \tag{5.95}$$

The first term will be zero if the energy of the state JT is less than that of IT, or $A_{JT,IT}$ is not an allowed transition. The other three terms will be zero if $|l_{IT} - l_{JT}| \neq 1$ or the conditions on Δn are not fulfilled.

The matrix formed was inverted and a set of simultaneous equations formed which were then solved for B(IT). These were then substituted for the previous values and the process of solving the level population equation repeated, starting at the high state solutions for $n = NLIM$, and continuing until the required degree of convergence was reached.

5.8 Effective Recombination Coefficients and the Flux in a Line

Having determined the population of the state, the b_{nl} values can be used to calculate effective recombination coefficients, useful for theoretical comparisons and for evaluating the effective flux in a given wavelength, which can be directly applied to astrophysical plasmas as this is the quantity that is obtained from observations.

The effective recombination coefficient, $\alpha_{nl}^{\text{eff}}(\lambda)$, may be calculated for a given line of wavelength λ, by the relation,

$$\alpha_{nl}^{\text{eff}}(\lambda) = b_{nl} \frac{g_{nl}}{2g_+} e^{\chi_n} \left(\frac{h^2}{2\pi mkT} \right)^{\frac{3}{2}} A_\lambda \quad \text{cm}^{-3}\ \text{s}^{-1} \tag{5.96}$$

where A_λ is the transition probability and g_+ is the statistical weight of the ion. The effective flux in a line is then given by

$$F(\lambda) = N_e N_+ \alpha_{nl}^{\text{eff}}(\lambda) \frac{hc}{\lambda} \quad \text{erg cm}^{-3}\ \text{s}^{-1} \tag{5.97}$$

5.9 Results

Results and comparison with previous calculations are presented in this section. Tables of wavelengths are given for all transitions for which probabilities have been calculated in the course of this work. Where the values of the principal quantum number are such that hydrogenic transition probabilities were used for high l, this value is also given for comparison. Tables of case A and case B effective recombination coefficients are also given, applicable to the planetary nebular density and temperature range, for transitions between all states for which high accuracy is prescribed, ($n \leq 8$).

5.9.1 Wavelengths (Å) for Transitions in the Low State Region

Wavelengths for all low state allowed transitions are presented, up to and including transitions to and from $l = 3$ states. Tables (5.2) to (5.5) give wavelengths arising from transitions between ^{1}S parent states. Tables (5.6) to (5.9) give wavelengths from transitions involving states of 2s2p ^{3}P^0 and 2p^2 ^{3}P parentage. These are give in two forms for convenience. The first is sorted by the lower state and the second by wavelength. For states up to and including $n = 7$ the values are expected to be very accurate as the experimental energies from Moore (1970) were used. These wavelengths are given to two decimal places. Above $n = 7$, theoretically calculated energies from STGB are used which will be less accurate and so the values are only given to the nearest integer. It is assumed that the $n = 8$ series will be of high accuracy since the quantum defect will have changed little from the $n = 7$ transitions. Some care though, must be taken because their is configuration interaction between the 2s2p3p ^{2}D state and the 2s^{2}8d ^{2}D state. These values are also given to two decimal places. For $g \rightarrow f$ transitions where the quantum defects are small a high degree of accuracy may be assumed even though one or more states involved may use theoretically calculated energies. These tables are of use in the line identification in all regions of the spectrum. Wavelengths below 2000Å are given in vacuo. Wavelengths above 2000Å are air wavelengths.

Table 5.2: Wavelengths (Å), for transitions up to and including $L = 2$ of states with ^{1}S parents, in the range $n = 15 - 12$.

		$l \rightarrow l'$			
n	n'	0-1	1-0	1-2	2-1
15	14	409355	265639	466827	257035
15	13	158313	145205	173347	128795
15	12	89053	71011	96704	78884
15	11	56858	48014	61671	52534
15	10	38433	33321	41795	36408
15	9	26645	23393	29177	25656
15	8	18583	16377	20862	18096
15	7	12807	11251	13845	12574
15	6	8649	7486	9482	8542
15	5	5191	4700	6201	5152
15	4	3121	2674	3773	3107
15	3	1592	1281	2037	1588
15	2	514	—	—	514
14	13	310794	264658	375881	206613
14	12	122998	91124	138266	102537
14	11	69020	56437	76297	62069
14	10	43630	37171	48035	40746
14	9	29044	25228	32087	27737
14	8	19718	17255	22308	19107
14	7	13336	11659	14468	13054
14	6	8887	7665	9770	8761
14	5	5276	4770	6322	5231
14	4	3152	2697	3818	3136
14	3	1600	1286	2050	1596
14	2	515	—	—	515
13	12	199684	140839	297732	163240
13	11	87979	72227	108307	80100
13	10	50511	43424	59017	47811
13	9	31940	27960	36641	30839
13	8	21012	18491	24419	20529
13	7	13916	12210	15327	13703
13	6	9141	7899	10154	9048
13	5	5364	4859	6481	5332
13	4	3183	2725	3875	3172
13	3	1608	1292	2067	1605
13	2	516	—	—	516
12	11	239765	111950	231463	126385
12	10	79351	55200	83115	61185
12	9	41471	32412	44685	35900
12	8	24754	20338	27747	22656
12	7	15464	12989	16575	14618
12	6	9784	8218	10687	9439
12	5	5579	4978	6694	5465
12	4	3258	2762	3951	3218
12	3	1627	1301	2088	1617
12	2	518	—	—	517

Table 5.3: Wavelengths (Å), for transitions up to and including $L = 2$ of states with $^1\mathrm{S}$ parents, in the range $n = 11 - 3$.

		$l \rightarrow l'$			
n	n′	0-1	1-0	1-2	2-1
11	10	170726	85051	176268	95515
11	9	57576	40826	62420	45494
11	8	29716	23359	33691	26134
11	7	17265	14159	18528	15992
11	6	10476	8671	11466	9993
11	5	5797	5141	6992	5647
11	4	3331	2811	4052	3280
11	3	1645	1311	2116	1632
11	2	520	—	—	518
10	9	122177	62256	131768	70080
10	8	40868	29088	47059	32730
10	7	20518	16078	21958	18241
10	6	11591	9355	12694	10827
10	5	6123	5374	7430	5904
10	4	3436	2880	4196	3366
10	3	1670	1326	2154	1653
10	2	522	—	—	520
9	8	85237	43730	102681	49491
9	7	27778	19730	29386	22485
9	6	13599	10484	14866	12193
9	5	6642	5728	8125	6288
9	4	3593	2978	4409	3487
9	3	1706	1347	2209	1682
9	2	526	—	—	523
8	7	56546.20	29069.20	56349.60	32453.62
8	6	18108.81	12642.27	19613.81	14630.51
8	5	7561.31	6317.70	9363.70	6878.48
8	4	3846.32	3130.17	4749.75	3661.43
8	3	1761.12	1376.75	2291.73	1721.33
8	2	530.72	—	—	527.05
7	6	36490.25	18237.69	37430.37	22696.89
7	5	9575.34	7461.73	12117.23	8258.37
7	4	4307.18	3387.51	5368.59	4018.88
7	3	1851.81	1424.33	2426.70	1796.43
7	2	538.67	—	—	533.88
6	5	16740.40	10364.86	22227.17	11382.91
6	4	5334.17	3881.02	6723.54	4638.51
6	3	2018.23	1504.76	2669.94	1910.47
6	2	551.96	—	—	543.52
5	4	9234.94	5536.12	13946.90	6258.82
5	3	2402.19	1701.98	3361.28	2137.74
5	2	577.18	—	—	560.52
4	3	3920.11	2173.94	5890.37	2747.02
4	2	636.36	—	—	595.12
3	2	858.76	—	—	687.48

Table 5.4: Wavelengths (Å), for transitions in the angular momentum range $L = 2 - 4$, of states with ^{1}S parents, in the range $n = 15 - 12$. Also included is the wavelength of the hydrogenic $l = 5 \rightarrow 4$ transition

		$l \rightarrow l'$				
n	n′	2-3	3-2	3-4	4-3	Hyd.
15	14	357924	329831	352101	338798	346360
15	13	156454	150184	155692	152686	154657
15	12	91513	89043	91419	90211	91106
15	11	59673	58463	59731	59116	59624
15	10	40938	40297	41031	40675	40998
15	9	28737	28439	28831	28607	28827
15	8	20282	20482	20347	20217	20372
15	7	14170	13677	14249	14139	14268
15	6	9687	9403	9746	9672	9761
15	5	6351	6167	6394	6345	6392
15	4	3887	3761	—	3885	—
15	3	—	2034	—	—	—
15	2	—	—	—	—	—
14	13	288402	266166	283970	273288	279426
14	12	124952	120061	124421	122028	123624
14	11	72287	70406	72254	71299	72023
14	10	46505	45632	46576	46094	46503
14	9	31373	30996	31463	31186	31444
14	8	21560	21776	21624	21472	21645
14	7	14783	14242	14864	14741	14881
14	6	9969	9666	10029	9950	10045
14	5	6471	6279	6515	6463	6512
14	4	3932	3802	—	3929	—
14	3	—	2046	—	—	—
14	2	—	—	—	—	—
13	12	228496	211358	225254	216826	221716
13	11	97971	94290	97634	95761	97033
13	10	55939	54595	55952	55212	55786
13	9	35401	34887	35479	35109	35430
13	8	23389	23627	23448	23261	23462
13	7	15620	15011	15703	15563	15718
13	6	10343	10015	10405	10318	10419
13	5	6627	6424	6672	6617	6667
13	4	3989	3855	—	3985	—
13	3	—	2061	—	—	—
13	2	—	—	—	—	—
12	11	177460	164749	175234	168721	172547
12	10	75163	72563	74980	73549	74541
12	9	42238	41445	42283	41723	42169
12	8	26190	26463	26239	25991	26239
12	7	16822	16108	16908	16739	16917
12	6	10856	10491	10920	10822	10933
12	5	6834	6617	6880	6820	6874
12	4	4063	3924	—	4058	—
12	3	—	2080	—	—	—
12	2	—	—	—	—	—

Table 5.5: Wavelengths (Å), for transitions in the angular momentum range $L = 2 - 4$, of states with ^{1}S parents, in the range $n = 11 - 3$. Also included is the wavelength of the hydrogenic $l = 5 \rightarrow 4$ transition

				l → l′		
n	n′	2-3	3-2	3-4	4-3	Hyd.
11	10	134585	125780	133223	128313	131236
11	9	56176	54651	56118	55053	55808
11	8	30952	31290	30978	30608	30944
11	7	18666	17778	18757	18540	18756
11	6	11596	11175	11663	11547	11672
11	5	7120	6882	7167	7101	7159
11	4	4162	4015	—	4156	—
11	3	—	2106	—	—	—
11	2	—	—	—	—	—
10	9	99108	94088	98520	94929	97100
10	8	40655	41171	40632	39934	40492
10	7	21805	20584	21908	21595	21883
10	6	12735	12222	12808	12663	12812
10	5	7533	7266	7584	7508	7572
10	4	4300	4143	—	4292	—
10	3	—	2140	—	—	—
10	2	—	—	—	—	—
9	8	70177	71848	70224	67898	69455
9	7	28157	26171	28350	27783	28250
9	6	14667	13996	14770	14565	14759
9	5	8170	7858	8232	8138	8213
9	4	4500	4329	—	4491	—
9	3	—	2189	—	—	—
9	2	—	—	—	—	—
8	7	45758.44	42189.85	48154.62	46442.59	47618.09
8	6	18342.53	17562.19	18798.08	18451.48	18741.81
8	5	9196.71	8869.06	9348.09	9224.02	9314.19
8	4	4795.27	4619.08	—	4802.68	—
8	3	—	2260.86	—	—	—
8	2	—	—	—	—	—
7	6	33083.30	28030.37	31316.54	30154.38	30905.97
7	5	11842.29	10930.58	11667.42	11444.39	11579.09
7	4	5427.49	5122.21	—	5342.36	—
7	3	—	2375.06	—	—	—
7	2	—	—	—	—	—
6	5	19529.37	17000.39	18852.11	18198.86	18516.37
6	4	6622.14	6151.45	—	6461.94	—
6	3	—	2574.84	—	—	—
6	2	—	—	—	—	—
5	4	10504.49	9229.63	—	9903.43	—
5	3	—	2992.63	—	—	—
5	2	—	—	—	—	—
4	3	—	4267.18	—	—	—
4	2	—	—	—	—	—
3	2	—	—	—	—	—

Table 5.6: Wavelengths (Å) for transitions including states with 2s2p and $2p^2$ parents, in the region $n \leq 15, L \leq 4$, sorted by lower state.

Transition			Wavelength Å	Transition			Wavelength Å
$2s^28s\ ^2S$	—	$2s2p3s\ ^2P^0$	9274.64	$2s^214p\ ^2P^0$	—	$2s2p3p\ ^2D$	17360
$2s^28d\ ^2D$	—	$2s2p3s\ ^2P^0$	8267.91	$2s^214f\ ^2F^0$	—	$2s2p3p\ ^2D$	17036
$2s^29s\ ^2S$	—	$2s2p3s\ ^2P^0$	7928	$2s^215p\ ^2P^0$	—	$2s2p3p\ ^2D$	16471
$2s^29d\ ^2D$	—	$2s2p3s\ ^2P^0$	7429	$2s^215f\ ^2F^0$	—	$2s2p3p\ ^2D$	16233
$2s^210s\ ^2S$	—	$2s2p3s\ ^2P^0$	7201	$2s^28p\ ^2P^0$	—	$2s2p3p\ ^2D$	160439.7
$2s^210d\ ^2D$	—	$2s2p3s\ ^2P^0$	6899	$2s^23p\ ^2P^0$	—	$2s2p^2\ ^2S$	2840.90
$2s^211s\ ^2S$	—	$2s2p3s\ ^2P^0$	6754	$2s^24p\ ^2P^0$	—	$2s2p^2\ ^2S$	1515.60
$2s^211d\ ^2D$	—	$2s2p3s\ ^2P^0$	6550	$2p^3\ ^2P^0$	—	$2s2p^2\ ^2S$	1384.12
$2s^212s\ ^2S$	—	$2s2p3s\ ^2P^0$	6460	$2s^25p\ ^2P^0$	—	$2s2p^2\ ^2S$	1269.84
$2s^212d\ ^2D$	—	$2s2p3s\ ^2P^0$	6307	$2s^26p\ ^2P^0$	—	$2s2p^2\ ^2S$	1156.72
$2s^213s\ ^2S$	—	$2s2p3s\ ^2P^0$	6173	$2s^27p\ ^2P^0$	—	$2s2p^2\ ^2S$	1108.60
$2s^213d\ ^2D$	—	$2s2p3s\ ^2P^0$	6131	$2s^28p\ ^2P^0$	—	$2s2p^2\ ^2S$	1080
$2s^214s\ ^2S$	—	$2s2p3s\ ^2P^0$	6056	$2s^29p\ ^2P^0$	—	$2s2p^2\ ^2S$	1061
$2s^214d\ ^2D$	—	$2s2p3s\ ^2P^0$	5997	$2s^210p\ ^2P^0$	—	$2s2p^2\ ^2S$	1048
$2s^215s\ ^2S$	—	$2s2p3s\ ^2P^0$	5945	$2s^211p\ ^2P^0$	—	$2s2p^2\ ^2S$	1039
$2s^215d\ ^2D$	—	$2s2p3s\ ^2P^0$	5894	$2s^212p\ ^2P^0$	—	$2s2p^2\ ^2S$	1032
$2s^26s\ ^2S$	—	$2s2p3s\ ^2P^0$	28324.89	$2s^213p\ ^2P^0$	—	$2s2p^2\ ^2S$	1027
$2s^26d\ ^2D$	—	$2s2p3s\ ^2P^0$	15767.93	$2s^214p\ ^2P^0$	—	$2s2p^2\ ^2S$	1022
$2s^25d\ ^2D$	—	$2s2p3s\ ^2P^0$	131421.8	$2s^215p\ ^2P^0$	—	$2s2p^2\ ^2S$	1020
$2s^27s\ ^2S$	—	$2s2p3s\ ^2P^0$	12499.42	$2s^23p\ ^2P^0$	—	$2s2p^2\ ^2P$	4753.40
$2s^27d\ ^2D$	—	$2s2p3s\ ^2P^0$	10345.75	$2p^3\ ^2D^0$	—	$2s2p^2\ ^2P$	2511.06
$2s^213p\ ^2P^0$	—	$2s2p3p\ ^2S$	402785	$2s^24p\ ^2P^0$	—	$2s2p^2\ ^2P$	1929.67
$2s^214p\ ^2P^0$	—	$2s2p3p\ ^2S$	157321	$2p^3\ ^2P^0$	—	$2s2p^2\ ^2P$	1721.46
$2s^215p\ ^2P^0$	—	$2s2p3p\ ^2S$	105655	$2s^25p\ ^2P^0$	—	$2s2p^2\ ^2P$	1548.18
$2s^26p\ ^2P^0$	—	$2s2p3p\ ^2P$	99125.34	$2s^26p\ ^2P^0$	—	$2s2p^2\ ^2P$	1383.26
$2s^212p\ ^2P^0$	—	$2s2p3p\ ^2P$	8735	$2s^28p\ ^2P^0$	—	$2s2p^2\ ^2P$	1274.34
$2s^213p\ ^2P^0$	—	$2s2p3p\ ^2P$	8376	$2s^29p\ ^2P^0$	—	$2s2p^2\ ^2P$	1248
$2s^214p\ ^2P^0$	—	$2s2p3p\ ^2P$	8112.61	$2s^210p\ ^2P^0$	—	$2s2p^2\ ^2P$	1231
$2s^215p\ ^2P^0$	—	$2s2p3p\ ^2P$	7913	$2s^211p\ ^2P^0$	—	$2s2p^2\ ^2P$	1218
$2s^27p\ ^2P^0$	—	$2s2p3p\ ^2P$	20997.24	$2s^212p\ ^2P^0$	—	$2s2p^2\ ^2P$	1209
$2s^28p\ ^2P^0$	—	$2s2p3p\ ^2P$	13909.46	$2s^213p\ ^2P^0$	—	$2s2p^2\ ^2P$	1202
$2s^29p\ ^2P^0$	—	$2s2p3p\ ^2P$	11341	$2s^214p\ ^2P^0$	—	$2s2p^2\ ^2P$	1196
$2s^210p\ ^2P^0$	—	$2s2p3p\ ^2P$	10031	$2s^215p\ ^2P^0$	—	$2s2p^2\ ^2P$	1192
$2s^28f\ ^2F^0$	—	$2s2p3p\ ^2D$	82041.88	$2s^25p\ ^2P^0$	—	$2s2p^2\ ^2D$	996.88
$2s^29p\ ^2P^0$	—	$2s2p3p\ ^2D$	44411	$2s^25f\ ^2F^0$	—	$2s2p^2\ ^2D$	961.76
$2s^29f\ ^2F^0$	—	$2s2p3p\ ^2D$	37459	$2s^28p\ ^2P^0$	—	$2s2p^2\ ^2D$	875.71
$2s^210p\ ^2P^0$	—	$2s2p3p\ ^2D$	29388	$2s^26p\ ^2P^0$	—	$2s2p^2\ ^2D$	925.81
$2s^210f\ ^2F^0$	—	$2s2p3p\ ^2D$	26978	$2s^26f\ ^2F^0$	—	$2s2p^2\ ^2D$	914.11
$2s^211p\ ^2P^0$	—	$2s2p3p\ ^2D$	23552	$2s^27p\ ^2P^0$	—	$2s2p^2\ ^2D$	894.72
$2s^211f\ ^2F^0$	—	$2s2p3p\ ^2D$	22353	$2s^28f\ ^2F^0$	—	$2s2p^2\ ^2D$	871.17
$2s^212p\ ^2P^0$	—	$2s2p3p\ ^2D$	20484	$2s^27f\ ^2F^0$	—	$2s2p^2\ ^2D$	887.61
$2s^212f\ ^2F^0$	—	$2s2p3p\ ^2D$	19776	$2s^29p\ ^2P^0$	—	$2s2p^2\ ^2D$	863
$2s^213p\ ^2P^0$	—	$2s2p3p\ ^2D$	18611	$2s^29f\ ^2F^0$	—	$2s2p^2\ ^2D$	860
$2s^213f\ ^2F^0$	—	$2s2p3p\ ^2D$	18148	$2s^210p\ ^2P^0$	—	$2s2p^2\ ^2D$	855

Table 5.7: Wavelengths (Å) for transitions including states with 2s2p and $2p^2$ parents, in the region $n \leq 15, L \leq 4$, sorted by lower state.

Transition			Wavelength Å	Transition			Wavelength Å
$2s^210f$ $^2F^0$	—	$2s2p^2$ ^2D	853	$2s2p3p$ ^2P	—	$2s^22p$ $^2P^0$	549.77
$2s^211p$ $^2P^0$	—	$2s2p^2$ ^2D	849	$2s2p^2$ ^2D	—	$2s^22p$ $^2P^0$	1335.31
$2s^211f$ $^2F^0$	—	$2s2p^2$ ^2D	847	$2s2p^2$ ^2S	—	$2s^22p$ $^2P^0$	1036.79
$2s^212p$ $^2P^0$	—	$2s2p^2$ ^2D	844	$2s2p3p$ ^2S	—	$2s^212p$ $^2P^0$	411537
$2s^212f$ $^2F^0$	—	$2s2p^2$ ^2D	843	$2s2p3p$ ^2S	—	$2s^211p$ $^2P^0$	113787
$2s^213p$ $^2P^0$	—	$2s2p^2$ ^2D	841	$2s2p3p$ ^2S	—	$2s^210p$ $^2P^0$	58073
$2s^213f$ $^2F^0$	—	$2s2p^2$ ^2D	840	$2s^26s$ ^2S	—	$2p^3$ $^2P^0$	8014.54
$2s^214p$ $^2P^0$	—	$2s2p^2$ ^2D	838	$2s2p3p$ ^2P	—	$2p^3$ $^2P^0$	7576.94
$2s^214f$ $^2F^0$	—	$2s2p^2$ ^2D	837	$2s^26d$ ^2D	—	$2p^3$ $^2P^0$	6540.71
$2s^215f$ $^2F^0$	—	$2s2p^2$ ^2D	835	$2s^27s$ ^2S	—	$2p^3$ $^2P^0$	5900.66
$2s^215p$ $^2P^0$	—	$2s2p^2$ ^2D	836	$2s^27d$ ^2D	—	$2p^3$ $^2P^0$	5372.67
$2s^23p$ $^2P^0$	—	$2s2p^2$ ^2D	1762.04	$2s^28s$ ^2S	—	$2p^3$ $^2P^0$	5068.67
$2p^3$ $^2D^0$	—	$2s2p^2$ ^2D	1323.93	$2s2p3p$ ^2D	—	$2p^3$ $^2P^0$	5059.68
$2s^24p$ $^2P^0$	—	$2s2p^2$ ^2D	1142.30	$2s^28d$ ^2D	—	$2p^3$ $^2P^0$	4752.42
$2p^3$ $^2P^0$	—	$2s2p^2$ ^2D	1065.97	$2s^29s$ ^2S	—	$2p^3$ $^2P^0$	4638
$2s^24f$ $^2F^0$	—	$2s2p^2$ ^2D	1063.84	$2s^29d$ ^2D	—	$2p^3$ $^2P^0$	4463
$2s2p3p$ ^2S	—	$2s^29p$ $^2P^0$	34806	$2s^210s$ ^2S	—	$2p^3$ $^2P^0$	4379
$2s2p3p$ ^2S	—	$2s^28p$ $^2P^0$	22214.96	$2s^210d$ ^2D	—	$2p^3$ $^2P^0$	4266
$2s2p3p$ ^2D	—	$2s^27p$ $^2P^0$	55446.75	$2s^211s$ ^2S	—	$2p^3$ $^2P^0$	4210
$2s2p3p$ ^2S	—	$2s^27p$ $^2P^0$	14433.57	$2s^211d$ ^2D	—	$2p^3$ $^2P^0$	4130
$2s2p3p$ ^2D	—	$2s^27f$ $^2F^0$	110180.6	$2s^212s$ ^2S	—	$2p^3$ $^2P^0$	4094
$2s2p3p$ ^2D	—	$2s^26p$ $^2P^0$	17994.54	$2s^212d$ ^2D	—	$2p^3$ $^2P^0$	4032
$2s2p3p$ ^2S	—	$2s^26p$ $^2P^0$	9361.53	$2s2p3p$ ^2S	—	$2p^3$ $^2P^0$	4017.84
$2s2p3p$ ^2D	—	$2s^26f$ $^2F^0$	23957.71	$2s^213s$ ^2S	—	$2p^3$ $^2P^0$	3977
$2s2p3s$ $^2P^0$	—	$2s^25s$ ^2S	22789.07	$2s^213d$ ^2D	—	$2p^3$ $^2P^0$	3959
$2s2p3p$ ^2D	—	$2s^25p$ $^2P^0$	7541.32	$2s^214s$ ^2S	—	$2p^3$ $^2P^0$	3927
$2s2p3p$ ^2S	—	$2s^25p$ $^2P^0$	5439.19	$2s^214d$ ^2D	—	$2p^3$ $^2P^0$	3903
$2s2p3p$ ^2P	—	$2s^25p$ $^2P^0$	14938.32	$2s^215s$ ^2S	—	$2p^3$ $^2P^0$	3881
$2s2p3p$ ^2D	—	$2s^25f$ $^2F^0$	10421.37	$2s^215d$ ^2D	—	$2p^3$ $^2P^0$	3859
$2p^3$ $^2P^0$	—	$2s^24s$ ^2S	8650.96	$2s^25s$ ^2S	—	$2p^3$ $^2P^0$	21935.78
$2s2p3s$ $^2P^0$	—	$2s^24s$ ^2S	4876.54	$2s^25d$ ^2D	—	$2p^3$ $^2P^0$	10301.05
$2s2p3p$ ^2S	—	$2s^24p$ $^2P^0$	3209.36	$2s^24d$ ^2D	—	$2p^3$ $^2D^0$	5676.29
$2s2p3p$ ^2P	—	$2s^24p$ $^2P^0$	5136.72	$2s^25d$ ^2D	—	$2p^3$ $^2D^0$	3572.52
$2s2p3p$ ^2D	—	$2s^24p$ $^2P^0$	3841.14	$2s2p3p$ ^2P	—	$2p^3$ $^2D^0$	3176.44
$2s2p3p$ ^2D	—	$2s^24f$ $^2F^0$	5108.28	$2s^26d$ ^2D	—	$2p^3$ $^2D^0$	2978.60
$2p^3$ $^2P^0$	—	$2s^24d$ ^2D	150076.8	$2s^27d$ ^2D	—	$2p^3$ $^2D^0$	2710.26
$2s2p3s$ $^2P^0$	—	$2s^24d$ ^2D	10402.40	$2s2p3p$ ^2D	—	$2p^3$ $^2D^0$	2628.24
$2p^3$ $^2P^0$	—	$2s^23s$ ^2S	1913.76	$2s^28d$ ^2D	—	$2p^3$ $^2D^0$	2542.83
$2s2p3s$ $^2P^0$	—	$2s^23s$ ^2S	1634.06	$2s^29d$ ^2D	—	$2p^3$ $^2D^0$	2457
$2s2p3p$ ^2S	—	$2s^23p$ $^2P^0$	1614.45	$2s^210d$ ^2D	—	$2p^3$ $^2D^0$	2397
$2s2p3p$ ^2P	—	$2s^23p$ $^2P^0$	1989.94	$2s^211d$ ^2D	—	$2p^3$ $^2D^0$	2353
$2s2p3p$ ^2D	—	$2s^23p$ $^2P^0$	1760.03	$2s^212d$ ^2D	—	$2p^3$ $^2D^0$	2321
$2p^3$ $^2P^0$	—	$2s^23d$ ^2D	4301.70	$2s^213d$ ^2D	—	$2p^3$ $^2D^0$	2297
$2p^3$ $^2D^0$	—	$2s^23d$ ^2D	20148.85	$2s^214d$ ^2D	—	$2p^3$ $^2D^0$	2278
$2s2p3s$ $^2P^0$	—	$2s^23d$ ^2D	3106.19	$2s^215d$ ^2D	—	$2p^3$ $^2D^0$	2263
$2s2p^2$ ^2P	—	$2s^22p$ $^2P^0$	904.08				

Table 5.8: Wavelengths (Å) for transitions including states with 2s2p and 2p^2 parents, in the region $n \leq 15, L \leq 4$, sorted by wavelength.

Transition			Wavelength Å	Transition			Wavelength Å
2s2p3p ^{2}P	—	2s^{2}2p ^{2}P^0	549.77	2s^{2}5p ^{2}P^0	—	2s2p^2 ^{2}S	1269.84
2s^{2}15f ^{2}F^0	—	2s2p^2 ^{2}D	835	2s^{2}8p ^{2}P^0	—	2s2p^2 ^{2}P	1274.34
2s^{2}15p ^{2}P^0	—	2s2p^2 ^{2}D	836	2s^{2}7p ^{2}P^0	—	2s2p^2 ^{2}P	1315.00
2s^{2}14f ^{2}F^0	—	2s2p^2 ^{2}D	837	2p^3 ^{2}D^0	—	2s2p^2 ^{2}D	1323.93
2s^{2}14p ^{2}P^0	—	2s2p^2 ^{2}D	838	2s2p^2 ^{2}D	—	2s^{2}2p ^{2}P^0	1335.31
2s^{2}13f ^{2}F^0	—	2s2p^2 ^{2}D	840	2s^{2}6p ^{2}P^0	—	2s2p^2 ^{2}P	1383.26
2s^{2}13p ^{2}P^0	—	2s2p^2 ^{2}D	841	2p^3 ^{2}P^0	—	2s2p^2 ^{2}S	1384.12
2s^{2}12f ^{2}F^0	—	2s2p^2 ^{2}D	843	2s^{2}4p ^{2}P^0	—	2s2p^2 ^{2}S	1515.60
2s^{2}12p ^{2}P^0	—	2s2p^2 ^{2}D	844	2s^{2}5p ^{2}P^0	—	2s2p^2 ^{2}P	1548.18
2s^{2}11f ^{2}F^0	—	2s2p^2 ^{2}D	847	2s2p3p ^{2}S	—	2s^{2}3p ^{2}P^0	1614.45
2s^{2}11p ^{2}P^0	—	2s2p^2 ^{2}D	849	2s2p3s ^{2}P^0	—	2s^{2}3s ^{2}S	1634.06
2s^{2}10f ^{2}F^0	—	2s2p^2 ^{2}D	853	2p^3 ^{2}P^0	—	2s2p^2 ^{2}P	1721.46
2s^{2}10p ^{2}P^0	—	2s2p^2 ^{2}D	855	2s2p3p ^{2}D	—	2s^{2}3p ^{2}P^0	1760.03
2s^{2}9f ^{2}F^0	—	2s2p^2 ^{2}D	860	2s^{2}3p ^{2}P^0	—	2s2p^2 ^{2}D	1762.04
2s^{2}9p ^{2}P^0	—	2s2p^2 ^{2}D	863	2p^3 ^{2}P^0	—	2s^{2}3s ^{2}S	1913.76
2s^{2}8f ^{2}F^0	—	2s2p^2 ^{2}D	871.17	2s^{2}4p ^{2}P^0	—	2s2p^2 ^{2}P	1929.67
2s^{2}8p ^{2}P^0	—	2s2p^2 ^{2}D	875.71	2s2p3p ^{2}P	—	2s^{2}3p ^{2}P^0	1989.94
2s^{2}7f ^{2}F^0	—	2s2p^2 ^{2}D	887.61	2s^{2}15d ^{2}D	—	2p^3 ^{2}D^0	2263
2s^{2}7p ^{2}P^0	—	2s2p^2 ^{2}D	894.72	2s^{2}14d ^{2}D	—	2p^3 ^{2}D^0	2278
2s2p^2 ^{2}P	—	2s^{2}2p ^{2}P^0	904.08	2s^{2}13d ^{2}D	—	2p^3 ^{2}D^0	2297
2s^{2}6f ^{2}F^0	—	2s2p^2 ^{2}D	914.11	2s^{2}12d ^{2}D	—	2p^3 ^{2}D^0	2321
2s^{2}6p ^{2}P^0	—	2s2p^2 ^{2}D	925.81	2s^{2}11d ^{2}D	—	2p^3 ^{2}D^0	2353
2s^{2}5f ^{2}F^0	—	2s2p^2 ^{2}D	961.76	2s^{2}10d ^{2}D	—	2p^3 ^{2}D^0	2397
2s^{2}5p ^{2}P^0	—	2s2p^2 ^{2}D	996.88	2s^{2}9d ^{2}D	—	2p^3 ^{2}D^0	2457
2s^{2}15p ^{2}P^0	—	2s2p^2 ^{2}S	1020	2p^3 ^{2}D^0	—	2s2p^2 ^{2}P	2511.06
2s^{2}14p ^{2}P^0	—	2s2p^2 ^{2}S	1023	2s^{2}8d ^{2}D	—	2p^3 ^{2}D^0	2542.83
2s^{2}13p ^{2}P^0	—	2s2p^2 ^{2}S	1027	2s2p3p ^{2}D	—	2p^3 ^{2}D^0	2628.24
2s^{2}12p ^{2}P^0	—	2s2p^2 ^{2}S	1032	2s^{2}7d ^{2}D	—	2p^3 ^{2}D^0	2710.26
2s2p^2 ^{2}S	—	2s^{2}2p ^{2}P^0	1036.79	2s^{2}3p ^{2}P^0	—	2s2p^2 ^{2}S	2840.90
2s^{2}11p ^{2}P^0	—	2s2p^2 ^{2}S	1039	2s^{2}6d ^{2}D	—	2p^3 ^{2}D^0	2978.60
2s^{2}10p ^{2}P^0	—	2s2p^2 ^{2}S	1048	2s2p3s ^{2}P^0	—	2s^{2}3d ^{2}D	3106.19
2s^{2}9p ^{2}P^0	—	2s2p^2 ^{2}S	1061	2s2p3p ^{2}P	—	2p^3 ^{2}D^0	3176.44
2s^{2}4f ^{2}F^0	—	2s2p^2 ^{2}D	1063.84	2s2p3p ^{2}S	—	2s^{2}4p ^{2}P^0	3209.36
2p^3 ^{2}P^0	—	2s2p^2 ^{2}D	1065.97	2s^{2}5d ^{2}D	—	2p^3 ^{2}D^0	3572.52
2s^{2}8p ^{2}P^0	—	2s2p^2 ^{2}S	1080	2s2p3p ^{2}D	—	2s^{2}4p ^{2}P^0	3841.14
2s^{2}7p ^{2}P^0	—	2s2p^2 ^{2}S	1108.60	2s^{2}15d ^{2}D	—	2p^3 ^{2}P^0	3859
2s^{2}4p ^{2}P^0	—	2s2p^2 ^{2}D	1142.30	2s^{2}15s ^{2}S	—	2p^3 ^{2}P^0	3881
2s^{2}6p ^{2}P^0	—	2s2p^2 ^{2}S	1156.72	2s^{2}14d ^{2}D	—	2p^3 ^{2}P^0	3903
2s^{2}15p ^{2}P^0	—	2s2p^2 ^{2}P	1192	2s^{2}14s ^{2}S	—	2p^3 ^{2}P^0	3927
2s^{2}14p ^{2}P^0	—	2s2p^2 ^{2}P	1196	2s^{2}13d ^{2}D	—	2p^3 ^{2}P^0	3959
2s^{2}13p ^{2}P^0	—	2s2p^2 ^{2}P	1202	2s^{2}13s ^{2}S	—	2p^3 ^{2}P^0	3977
2s^{2}12p ^{2}P^0	—	2s2p^2 ^{2}P	1209	2s2p3p ^{2}S	—	2p^3 ^{2}P^0	4017.84
2s^{2}11p ^{2}P^0	—	2s2p^2 ^{2}P	1218	2s^{2}12d ^{2}D	—	2p^3 ^{2}P^0	4032
2s^{2}10p ^{2}P^0	—	2s2p^2 ^{2}P	1231	2s^{2}12s ^{2}S	—	2p^3 ^{2}P^0	4094
2s^{2}9p ^{2}P^0	—	2s2p^2 ^{2}P	1248	2s^{2}11d ^{2}D	—	2p^3 ^{2}P^0	4130

Table 5.9: Wavelengths (Å) for transitions including states with 2s2p and 2p^2 parents, in the region $n \leq 15, L \leq 4$, sorted by wavelength

Transition			Wavelength Å	Transition			Wavelength Å
2s^{2}11s ^{2}S	—	2p^3 ^{2}P^0	4210	2s^{2}7d ^{2}D	—	2s2p3s ^{2}P^0	10345.75
2s^{2}10d ^{2}D	—	2p^3 ^{2}P^0	4266	2s2p3s ^{2}P^0	—	2s^{2}4d ^{2}D	10402.40
2p^3 ^{2}P^0	—	2s^{2}3d ^{2}D	4301.70	2s2p3p ^{2}D	—	2s^{2}5f ^{2}F^0	10421.37
2s^{2}10s ^{2}S	—	2p^3 ^{2}P^0	4379	2s^{2}9p ^{2}P^0	—	2s2p3p ^{2}P	11341
2s^{2}9d ^{2}D	—	2p^3 ^{2}P^0	4463	2s^{2}7s ^{2}S	—	2s2p3s ^{2}P^0	12499.42
2s^{2}9s ^{2}S	—	2p^3 ^{2}P^0	4638	2s^{2}8p ^{2}P^0	—	2s2p3p ^{2}P	13909.46
2s^{2}8d ^{2}D	—	2p^3 ^{2}P^0	4752.42	2s2p3p ^{2}S	—	2s^{2}7p ^{2}P^0	14433.57
2s^{2}3p ^{2}P^0	—	2s2p^2 ^{2}P	4753.40	2s2p3p ^{2}P	—	2s^{2}5p ^{2}P^0	14938.32
2s2p3s ^{2}P^0	—	2s^{2}4s ^{2}S	4876.54	2s^{2}6d ^{2}D	—	2s2p3s ^{2}P^0	15767.93
2s2p3p ^{2}D	—	2p^3 ^{2}P^0	5059.68	2s^{2}15f ^{2}F^0	—	2s2p3p ^{2}D	16233
2s^{2}8s ^{2}S	—	2p^3 ^{2}P^0	5068.67	2s^{2}15p ^{2}P^0	—	2s2p3p ^{2}D	16471
2s2p3p ^{2}D	—	2s^{2}4f ^{2}F^0	5108.28	2s^{2}14f ^{2}F^0	—	2s2p3p ^{2}D	17036
2s2p3p ^{2}P	—	2s^{2}4p ^{2}P^0	5136.72	2s^{2}14p ^{2}P^0	—	2s2p3p ^{2}D	17360
2s^{2}7d ^{2}D	—	2p^3 ^{2}P^0	5372.67	2s2p3p ^{2}D	—	2s^{2}6p ^{2}P^0	17994.54
2s2p3p ^{2}S	—	2s^{2}5p ^{2}P^0	5439.19	2s^{2}13f ^{2}F^0	—	2s2p3p ^{2}D	18148
2s^{2}4d ^{2}D	—	2p^3 ^{2}D^0	5676.29	2s^{2}13p ^{2}P^0	—	2s2p3p ^{2}D	18611
2s^{2}15d ^{2}D	—	2s2p3s ^{2}P^0	5894	2s^{2}12f ^{2}F^0	—	2s2p3p ^{2}D	19776
2s^{2}7s ^{2}S	—	2p^3 ^{2}P^0	5900.66	2p^3 ^{2}D^0	—	2s^{2}3d ^{2}D	20148.85
2s^{2}15s ^{2}S	—	2s2p3s ^{2}P^0	5945	2s^{2}12p ^{2}P^0	—	2s2p3p ^{2}D	20484
2s^{2}14d ^{2}D	—	2s2p3s ^{2}P^0	5997	2s^{2}7p ^{2}P^0	—	2s2p3p ^{2}P	20997.24
2s^{2}14s ^{2}S	—	2s2p3s ^{2}P^0	6056	2s^{2}5s ^{2}S	—	2p^3 ^{2}P^0	21935.78
2s^{2}13d ^{2}D	—	2s2p3s ^{2}P^0	6131	2s2p3p ^{2}S	—	2s^{2}8p ^{2}P^0	22214.96
2s^{2}13s ^{2}S	—	2s2p3s ^{2}P^0	6173	2s^{2}11f ^{2}F^0	—	2s2p3p ^{2}D	22353
2s^{2}12d ^{2}D	—	2s2p3s ^{2}P^0	6307	2s2p3s ^{2}P^0	—	2s^{2}5s ^{2}S	22789.07
2s^{2}12s ^{2}S	—	2s2p3s ^{2}P^0	6460	2s^{2}11p ^{2}P^0	—	2s2p3p ^{2}D	23552
2s^{2}6d ^{2}D	—	2p^3 ^{2}P^0	6540.71	2s2p3p ^{2}D	—	2s^{2}6f ^{2}F^0	23957.71
2s^{2}11d ^{2}D	—	2s2p3s ^{2}P^0	6550	2s^{2}10f ^{2}F^0	—	2s2p3p ^{2}D	26978
2s^{2}11s ^{2}S	—	2s2p3s ^{2}P^0	6754	2s^{2}6s ^{2}S	—	2s2p3s ^{2}P^0	28324.89
2s^{2}10d ^{2}D	—	2s2p3s ^{2}P^0	6899	2s^{2}10p ^{2}P^0	—	2s2p3p ^{2}D	29388
2s^{2}10s ^{2}S	—	2s2p3s ^{2}P^0	7201	2s2p3p ^{2}S	—	2s^{2}9p ^{2}P^0	34806
2s^{2}9d ^{2}D	—	2s2p3s ^{2}P^0	7429	2s^{2}9f ^{2}F^0	—	2s2p3p ^{2}D	37459
2s2p3p ^{2}D	—	2s^{2}5p ^{2}P^0	7541.32	2s^{2}9p ^{2}P^0	—	2s2p3p ^{2}D	44411
2s2p3p ^{2}P	—	2p^3 ^{2}P^0	7576.94	2s2p3p ^{2}D	—	2s^{2}7p ^{2}P^0	55446.75
2s^{2}15p ^{2}P^0	—	2s2p3p ^{2}P	7913	2s2p3p ^{2}S	—	2s^{2}10p ^{2}P^0	58073
2s^{2}9s ^{2}S	—	2s2p3s ^{2}P^0	7928	2s^{2}8f ^{2}F^0	—	2s2p3p ^{2}D	82041.88
2s^{2}6s ^{2}S	—	2p^3 ^{2}P^0	8014.54	2s^{2}6p ^{2}P^0	—	2s2p3p ^{2}P	99125.34
2s^{2}14p ^{2}P^0	—	2s2p3p ^{2}P	8112.61	2s^{2}15p ^{2}P^0	—	2s2p3p ^{2}S	105655
2s^{2}8d ^{2}D	—	2s2p3s ^{2}P^0	8267.91	2s2p3p ^{2}D	—	2s^{2}7f ^{2}F^0	110180.6
2s^{2}13p ^{2}P^0	—	2s2p3p ^{2}P	8376	2s2p3p ^{2}S	—	2s^{2}11p ^{2}P^0	113787
2p^3 ^{2}P^0	—	2s^{2}4s ^{2}S	8650.96	2s^{2}5d ^{2}D	—	2s2p3s ^{2}P^0	131421.8
2s^{2}12p ^{2}P^0	—	2s2p3p ^{2}P	8735	2p^3 ^{2}P^0	—	2s^{2}4d ^{2}D	150076.8
2s^{2}11p ^{2}P^0	—	2s2p3p ^{2}P	9249	2s^{2}14p ^{2}P^0	—	2s2p3p ^{2}S	157321
2s^{2}8s ^{2}S	—	2s2p3s ^{2}P^0	9274.64	2s^{2}8p ^{2}P^0	—	2s2p3p ^{2}D	160439.7
2s2p3p ^{2}S	—	2s^{2}6p ^{2}P^0	9361.53	2s^{2}13p ^{2}P^0	—	2s2p3p ^{2}S	402785
2s^{2}10p ^{2}P^0	—	2s2p3p ^{2}P	10031	2s2p3p ^{2}S	—	2s^{2}12p ^{2}P^0	411537
2s^{2}5d ^{2}D	—	2p^3 ^{2}P^0	10301.05				

5.9.2 Effective Recombination Coefficients at Nebular Temperatures and Density

Effective recombination coefficients $\alpha^{\text{eff}}(\lambda)$ are presented for states, $n, n' < 8$ and $l, l' \leq 5$. Calculations were performed at the standard nebular density of 10^4 cm^{-3} and at temperatures ranging from 5000 to 15000 K. The values are tabulated as multiples of 10^{12}, and only transitions where the coefficients are larger than 10^{-15} at some value of the temperature are included. The unified treatment of dielectronic and radiative recombination coefficients leads to highly accurate effective recombination coefficients, when combined with transition probabilities that are of the same high order. The application of the CII recombination spectrum can be used to investigate planetary nebulae and other astrophysical plasmas in a similar fashion to the application of the work on the recombination spectrum of OII (Storey, 1994) to NGC 7009 (Liu *et al.*, in press). Both case A and case B calculations are given. In case B, transitions to the ground state are assumed to be optically thick and are not evaluated. The decay to the ground state is however included in the lifetime of the state, passed to routines using the impact parameter method to calculate angular momentum and energy changing collisions where, it is used as one of the cut-offs.

5.9.3 The Dielectronic Component of the Total Recombination Coefficient to a State

Storey (1981) calculated dielectronic recombination coefficients for recombination to a variety of ions including CII at nebular temperatures. It has been previously noted that for low lying resonance states the effective dielectronic recombination coefficients obtained are substantially larger than the corresponding radiative recombination coefficients, calculated neglecting resonances. Comparison is made here with the results of Storey (1981) for which the dielectronic recombination rate is expected to be much larger than the radiative one.

Table 5.10: Case A: Effective recombination coefficients ($\times\ 10^{12}$ cm^{3}s^{-1}) for low state transitions, $n, n' \leq 8$, at density of 10^4 cm^{-3}

Transition			Wavelength	Temperature (K)				
			Å	5000	7500	10000	12500	15000
2s2p3p ^{2}S	—	2s^{2}2p ^{2}P^0	516.58	0.00098	0.00106	0.00106	0.00106	0.00108
2s^{2}8d ^{2}D	—	2s^{2}2p ^{2}P^0	527.05	0.00465	0.00367	0.00310	0.00273	0.00251
2s2p3p ^{2}D	—	2s^{2}2p ^{2}P^0	530.62	0.05718	0.04775	0.04173	0.03800	0.03554
2s^{2}7d ^{2}D	—	2s^{2}2p ^{2}P^0	533.88	0.04168	0.03283	0.02745	0.02388	0.02158
2s^{2}6d ^{2}D	—	2s^{2}2p ^{2}P^0	543.52	0.06331	0.04902	0.04051	0.03486	0.03118
2s2p3p ^{2}P	—	2s^{2}2p ^{2}P^0	549.77	0.00502	0.00871	0.01103	0.01220	0.01267
2s^{2}6s ^{2}S	—	2s^{2}2p ^{2}P^0	551.96	0.00135	0.00120	0.00110	0.00104	0.00101
2s^{2}5d ^{2}D	—	2s^{2}2p ^{2}P^0	560.52	0.11745	0.08986	0.07364	0.06298	0.05608
2s^{2}5s ^{2}S	—	2s^{2}2p ^{2}P^0	577.18	0.00244	0.00216	0.00198	0.00189	0.00192
2s^{2}4d ^{2}D	—	2s^{2}2p ^{2}P^0	595.12	0.26958	0.20056	0.16103	0.13588	0.12041
2s^{2}4s ^{2}S	—	2s^{2}2p ^{2}P^0	636.36	0.00913	0.00789	0.00721	0.00716	0.00782
2s^{2}3d ^{2}D	—	2s^{2}2p ^{2}P^0	687.48	1.00383	0.69551	0.53483	0.44417	0.39625
2s^{2}3s ^{2}S	—	2s^{2}2p ^{2}P^0	858.76	0.23532	0.23648	0.24950	0.26197	0.26987
2s^{2}8f ^{2}F^0	—	2s2p^2 ^{2}D	871.17	0.00540	0.00395	0.00312	0.00259	0.00225
2s^{2}7f ^{2}F^0	—	2s2p^2 ^{2}D	887.61	0.00801	0.00580	0.00455	0.00376	0.00326
2s2p^2 ^{2}P	—	2s^{2}2p ^{2}P^0	904.08	0.03491	0.04513	0.05823	0.06991	0.07946
2s^{2}6f ^{2}F^0	—	2s2p^2 ^{2}D	914.11	0.01224	0.00874	0.00679	0.00556	0.00480
2s^{2}5f ^{2}F^0	—	2s2p^2 ^{2}D	961.76	0.02037	0.01417	0.01081	0.00873	0.00744
2s2p3s ^{2}P^0	—	2s2p^2 ^{2}D	973.19	0.00214	0.00178	0.00163	0.00155	0.00152
2s^{2}5p ^{2}P^0	—	2s2p^2 ^{2}D	996.88	0.00576	0.00492	0.00451	0.00429	0.00419
2s2p^2 ^{2}S	—	2s^{2}2p ^{2}P^0	1036.79	0.86321	0.81909	0.73955	0.67173	0.61785
2s^{2}4f ^{2}F^0	—	2s2p^2 ^{2}D	1063.84	0.03659	0.02405	0.01765	0.01387	0.01155
2p^3 ^{2}P^0	—	2s2p^2 ^{2}D	1065.97	0.03400	0.02748	0.02387	0.02176	0.02056
2s^{2}4p ^{2}P^0	—	2s2p^2 ^{2}D	1142.30	0.04079	0.03402	0.03014	0.02763	0.02597
2s^{2}6p ^{2}P^0	—	2s2p^2 ^{2}S	1156.72	0.00402	0.00338	0.00301	0.00277	0.00260
2s2p3s ^{2}P^0	—	2s2p^2 ^{2}S	1231.64	0.02127	0.01773	0.01619	0.01546	0.01509
2s^{2}5p ^{2}P^0	—	2s2p^2 ^{2}S	1269.84	0.00456	0.00390	0.00357	0.00340	0.00331
2p^3 ^{2}D^0	—	2s2p^2 ^{2}D	1323.93	0.00315	0.00328	0.00386	0.00458	0.00532
2s2p^2 ^{2}D	—	2s^{2}2p ^{2}P^0	1335.31	7.14816	5.40682	4.23927	3.47729	2.95944
2s^{2}8p ^{2}P^0	—	2s^{2}3s ^{2}S	1376.75	0.00228	0.00192	0.00171	0.00157	0.00147
2s^{2}7p ^{2}P^0	—	2s^{2}3s ^{2}S	1424.33	0.00333	0.00281	0.00251	0.00231	0.00218
2s2p3s ^{2}P^0	—	2s2p^2 ^{2}P	1491.77	0.00307	0.00256	0.00233	0.00223	0.00218
2s^{2}6p ^{2}P^0	—	2s^{2}3s ^{2}S	1504.76	0.00509	0.00428	0.00382	0.00351	0.00330
2s^{2}5p ^{2}P^0	—	2s2p^2 ^{2}P	1548.18	0.00429	0.00366	0.00336	0.00319	0.00312
2p^3 ^{2}P^0	—	2s2p^2 ^{2}P	1721.46	0.00697	0.00563	0.00489	0.00446	0.00422
2s2p3p ^{2}D	—	2s^{2}3p ^{2}P^0	1760.03	0.00439	0.00367	0.00320	0.00292	0.00273
2s^{2}3p ^{2}P^0	—	2s2p^2 ^{2}D	1762.04	0.09225	0.07750	0.07312	0.07408	0.07731
2s^{2}7d ^{2}D	—	2s^{2}3p ^{2}P^0	1796.43	0.00316	0.00249	0.00208	0.00181	0.00164
2s^{2}6d ^{2}D	—	2s^{2}3p ^{2}P^0	1910.47	0.00450	0.00348	0.00288	0.00248	0.00221
2s^{2}4p ^{2}P^0	—	2s2p^2 ^{2}P	1929.67	0.00302	0.00252	0.00223	0.00205	0.00193
2s^{2}5d ^{2}D	—	2s^{2}3p ^{2}P^0	2137.74	0.00724	0.00554	0.00454	0.00388	0.00346
2s^{2}4p ^{2}P^0	—	2s^{2}3s ^{2}S	2173.94	0.00569	0.00474	0.00420	0.00385	0.00362
2s^{2}8f ^{2}F^0	—	2s^{2}3d ^{2}D	2260.86	0.01409	0.01031	0.00814	0.00675	0.00587
2s^{2}8p ^{2}P^0	—	2s^{2}3d ^{2}D	2291.73	0.00114	0.00096	0.00086	0.00079	0.00074
2s^{2}7f ^{2}F^0	—	2s^{2}3d ^{2}D	2375.06	0.02503	0.01812	0.01422	0.01174	0.01020
2s^{2}5s ^{2}S	—	2s^{2}3p ^{2}P^0	2402.19	0.00133	0.00117	0.00108	0.00103	0.00104
2s^{2}7p ^{2}P^0	—	2s^{2}3d ^{2}D	2426.70	0.00181	0.00153	0.00137	0.00126	0.00118
2s^{2}8d ^{2}D	—	2p^3 ^{2}D^0	2542.83	0.00198	0.00156	0.00132	0.00116	0.00107
2s^{2}6f ^{2}F^0	—	2s^{2}3d ^{2}D	2574.84	0.05007	0.03575	0.02778	0.02276	0.01963
2s^{2}6p ^{2}P^0	—	2s^{2}3d ^{2}D	2669.94	0.00314	0.00264	0.00236	0.00217	0.00204

Table 5.11: Case A: Effective recombination coefficients ($\times\ 10^{12}$ cm^{3}s^{-1}) for low state transitions, $n, n' \leq 8$, at density of 10^4 cm^{-3}

			Wavelength	Temperature (K)				
Transition			Å	5000	7500	10000	12500	15000
2s^{2}4d ^{2}D	—	2s^{2}3p ^{2}P^0	2747.02	0.01068	0.00794	0.00638	0.00538	0.00477
2s^{2}3p ^{2}P^0	—	2s2p^2 ^{2}S	2840.90	0.07853	0.06597	0.06224	0.06306	0.06581
2s^{2}5f ^{2}F^0	—	2s^{2}3d ^{2}D	2992.63	0.12968	0.09016	0.06878	0.05556	0.04736
2s^{2}5p ^{2}P^0	—	2s^{2}3d ^{2}D	3361.28	0.00103	0.00088	0.00080	0.00076	0.00074
2s2p3p ^{2}D	—	2s^{2}4p ^{2}P^0	3841.14	0.00236	0.00197	0.00172	0.00157	0.00147
2s^{2}4s ^{2}S	—	2s^{2}3p ^{2}P^0	3920.11	0.00572	0.00494	0.00452	0.00449	0.00490
2s2p3p ^{2}S	—	2p^3 ^{2}P^0	4017.84	0.00115	0.00124	0.00124	0.00124	0.00126
2s^{2}4f ^{2}F^0	—	2s^{2}3d ^{2}D	4267.18	0.56548	0.37157	0.27274	0.21427	0.17854
2s^{2}8f ^{2}F^0	—	2s^{2}4d ^{2}D	4619.08	0.00920	0.00672	0.00531	0.00440	0.00383
2s^{2}8p ^{2}P^0	—	2s^{2}4d ^{2}D	4749.75	0.00101	0.00085	0.00075	0.00069	0.00065
2s^{2}8d ^{2}D	—	2p^3 ^{2}P^0	4752.42	0.01778	0.01404	0.01184	0.01044	0.00959
2s^{2}8g ^{2}G	—	2s^{2}4f ^{2}F^0	4802.68	0.01898	0.01298	0.00975	0.00776	0.00650
2s2p3p ^{2}D	—	2p^3 ^{2}P^0	5059.68	0.00338	0.00282	0.00247	0.00225	0.00210
2s^{2}7f ^{2}F^0	—	2s^{2}4d ^{2}D	5122.21	0.01582	0.01145	0.00899	0.00742	0.00645
2s^{2}7g ^{2}G	—	2s^{2}4f ^{2}F^0	5342.36	0.03656	0.02466	0.01836	0.01449	0.01196
2s^{2}7p ^{2}P^0	—	2s^{2}4d ^{2}D	5368.59	0.00168	0.00142	0.00127	0.00116	0.00110
2s^{2}4p ^{2}P^0	—	2s^{2}3d ^{2}D	5890.37	0.00853	0.00711	0.00630	0.00578	0.00543
2s^{2}6f ^{2}F^0	—	2s^{2}4d ^{2}D	6151.45	0.02994	0.02137	0.01661	0.01361	0.01174
2s^{2}6g ^{2}G	—	2s^{2}4f ^{2}F^0	6461.94	0.08884	0.05854	0.04290	0.03348	0.02744
2s^{2}3p ^{2}P^0	—	2s^{2}3s ^{2}S	6579.50	0.07824	0.06573	0.06201	0.06282	0.06557
2s^{2}6p ^{2}P^0	—	2s^{2}4d ^{2}D	6723.54	0.00325	0.00273	0.00244	0.00224	0.00210
2s^{2}3d ^{2}D	—	2s^{2}3p ^{2}P^0	7234.73	0.01484	0.01029	0.00791	0.00657	0.00586
2s^{2}8d ^{2}D	—	2s2p3s ^{2}P^0	8267.91	0.00635	0.00502	0.00423	0.00373	0.00343
2s^{2}8f ^{2}F^0	—	2s^{2}5d ^{2}D	8869.06	0.00512	0.00375	0.00296	0.00245	0.00213
2s^{2}8g ^{2}G	—	2s^{2}5f ^{2}F^0	9224.02	0.01621	0.01108	0.00833	0.00663	0.00555
2s^{2}5f ^{2}F^0	—	2s^{2}4d ^{2}D	9229.63	0.06759	0.04700	0.03585	0.02896	0.02469
2s^{2}8h ^{2}H^0	—	2s^{2}5g ^{2}G	9314.19	0.02215	0.01428	0.01029	0.00790	0.00634
2s^{2}5g ^{2}G	—	2s^{2}4f ^{2}F^0	9903.43	0.34394	0.21698	0.15453	0.11824	0.09558
2s^{2}7f ^{2}F^0	—	2s^{2}5d ^{2}D	10930.58	0.00850	0.00616	0.00483	0.00399	0.00346
2s^{2}7g ^{2}G	—	2s^{2}5f ^{2}F^0	11444.39	0.03047	0.02055	0.01530	0.01208	0.00997
2s^{2}7h ^{2}H^0	—	2s^{2}5g ^{2}G	11579.09	0.05329	0.03367	0.02395	0.01823	0.01452
2s^{2}7p ^{2}P^0	—	2s^{2}5d ^{2}D	12117.23	0.00146	0.00123	0.00110	0.00101	0.00095
2s^{2}6f ^{2}F^0	—	2s^{2}5d ^{2}D	17000.39	0.01446	0.01032	0.00802	0.00657	0.00567
2s^{2}8f ^{2}F^0	—	2s^{2}6d ^{2}D	17562.19	0.00290	0.00212	0.00168	0.00139	0.00121
2s^{2}4d ^{2}D	—	2s^{2}4p ^{2}P^0	17846.51	0.00230	0.00171	0.00137	0.00116	0.00103
2s^{2}6g ^{2}G	—	2s^{2}5f ^{2}F^0	18198.86	0.06875	0.04530	0.03320	0.02591	0.02124
2s^{2}8g ^{2}G	—	2s^{2}6f ^{2}F^0	18451.48	0.01140	0.00779	0.00586	0.00466	0.00390
2s^{2}6h ^{2}H^0	—	2s^{2}5g ^{2}G	18516.37	0.20014	0.12241	0.08529	0.06402	0.05044
2s^{2}8h ^{2}H^0	—	2s^{2}6g ^{2}G	18661.50	0.02442	0.01574	0.01134	0.00871	0.00699
2s^{2}4p ^{2}P^0	—	2s^{2}4s ^{2}S	18904.57	0.00165	0.00138	0.00122	0.00112	0.00105
2s^{2}6p ^{2}P^0	—	2s^{2}5d ^{2}D	22227.17	0.00326	0.00274	0.00244	0.00225	0.00211
2s^{2}7f ^{2}F^0	—	2s^{2}6d ^{2}D	28030.37	0.00432	0.00313	0.00246	0.00203	0.00176
2s^{2}7g ^{2}G	—	2s^{2}6f ^{2}F^0	30154.38	0.02008	0.01354	0.01008	0.00796	0.00657
2s^{2}7h ^{2}H^0	—	2s^{2}6g ^{2}G	30688.20	0.05576	0.03523	0.02506	0.01908	0.01519
2s^{2}7p ^{2}P^0	—	2s^{2}6d ^{2}D	37430.37	0.00145	0.00122	0.00109	0.00101	0.00095
2s^{2}8f ^{2}F^0	—	2s^{2}7d ^{2}D	42189.85	0.00133	0.00098	0.00077	0.00064	0.00056
2s^{2}8g ^{2}G	—	2s^{2}7f ^{2}F^0	46442.59	0.00745	0.00510	0.00383	0.00305	0.00255
2s^{2}8h ^{2}H^0	—	2s^{2}7g ^{2}G	47268.44	0.01982	0.01277	0.00920	0.00707	0.00567

Table 5.12: Case B: Effective recombination coefficients ($\times\ 10^{12}$ cm^{3}s^{-1}) for low state transitions, $n, n' \leq 8$, at density of 10^4 cm^{-3}

Transition			Wavelength	Temperature (K)				
			Å	5000	7500	10000	12500	15000
2s^{2}8f ^{2}F^0	—	2s2p^2 ^{2}D	871.17	0.00554	0.00406	0.00321	0.00266	0.00232
2s^{2}7f ^{2}F^0	—	2s2p^2 ^{2}D	887.61	0.00815	0.00591	0.00464	0.00383	0.00333
2s^{2}6f ^{2}F^0	—	2s2p^2 ^{2}D	914.11	0.01245	0.00890	0.00693	0.00568	0.00491
2s^{2}5f ^{2}F^0	—	2s2p^2 ^{2}D	961.76	0.02067	0.01440	0.01100	0.00890	0.00759
2s2p3s ^{2}P^0	—	2s2p^2 ^{2}D	973.19	0.00348	0.00283	0.00251	0.00232	0.00222
2s^{2}5p ^{2}P^0	—	2s2p^2 ^{2}D	996.88	0.01081	0.00889	0.00788	0.00736	0.00718
2s^{2}4f ^{2}F^0	—	2s2p^2 ^{2}D	1063.84	0.03691	0.02429	0.01785	0.01404	0.01171
2p^3 ^{2}P^0	—	2s2p^2 ^{2}D	1065.97	0.06866	0.05605	0.04873	0.04421	0.04154
2s^{2}4p ^{2}P^0	—	2s2p^2 ^{2}D	1142.30	0.10330	0.08239	0.07025	0.06246	0.05757
2s^{2}6p ^{2}P^0	—	2s2p^2 ^{2}S	1156.72	0.00510	0.00423	0.00372	0.00341	0.00322
2s2p3s ^{2}P^0	—	2s2p^2 ^{2}S	1231.64	0.03458	0.02819	0.02495	0.02312	0.02210
2s^{2}5p ^{2}P^0	—	2s2p^2 ^{2}S	1269.84	0.00856	0.00704	0.00624	0.00583	0.00569
2p^3 ^{2}D^0	—	2s2p^2 ^{2}D	1323.93	0.00897	0.00979	0.01079	0.01168	0.01242
2s^{2}8p ^{2}P^0	—	2s^{2}3s ^{2}S	1376.75	0.00254	0.00212	0.00187	0.00172	0.00162
2s^{2}7p ^{2}P^0	—	2s^{2}3s ^{2}S	1424.33	0.00391	0.00327	0.00290	0.00266	0.00251
2s2p3s ^{2}P^0	—	2s2p^2 ^{2}P	1491.77	0.00499	0.00407	0.00360	0.00333	0.00319
2s^{2}6p ^{2}P^0	—	2s^{2}3s ^{2}S	1504.76	0.00646	0.00535	0.00472	0.00432	0.00408
2s^{2}5p ^{2}P^0	—	2s2p^2 ^{2}P	1548.18	0.00805	0.00662	0.00587	0.00548	0.00535
2s^{2}5p ^{2}P^0	—	2s^{2}3s ^{2}S	1701.98	0.00172	0.00142	0.00126	0.00117	0.00114
2p^3 ^{2}P^0	—	2s2p^2 ^{2}P	1721.46	0.01407	0.01149	0.00999	0.00906	0.00852
2s2p3p ^{2}D	—	2s^{2}3p ^{2}P^0	1760.03	0.02570	0.02146	0.01875	0.01707	0.01597
2s^{2}3p ^{2}P^0	—	2s2p^2 ^{2}D	1762.04	1.03535	0.78817	0.66346	0.59517	0.55956
2s^{2}7d ^{2}D	—	2s^{2}3p ^{2}P^0	1796.43	0.03255	0.02563	0.02143	0.01864	0.01685
2s^{2}6d ^{2}D	—	2s^{2}3p ^{2}P^0	1910.47	0.05181	0.04012	0.03315	0.02854	0.02554
2s^{2}4p ^{2}P^0	—	2s2p^2 ^{2}P	1929.67	0.00766	0.00611	0.00521	0.00463	0.00427
2s2p3p ^{2}P	—	2s^{2}3p ^{2}P^0	1989.94	0.00193	0.00335	0.00425	0.00470	0.00488
2s^{2}6s ^{2}S	—	2s^{2}3p ^{2}P^0	2018.23	0.00148	0.00131	0.00119	0.00112	0.00109
2s^{2}5d ^{2}D	—	2s^{2}3p ^{2}P^0	2137.74	0.09960	0.07622	0.06248	0.05346	0.04766
2s^{2}4p ^{2}P^0	—	2s^{2}4s ^{2}S	2173.94	0.01441	0.01149	0.00980	0.00871	0.00803
2s^{2}8f ^{2}F^0	—	2s^{2}3d ^{2}D	2260.86	0.01446	0.01058	0.00837	0.00695	0.00604
2s^{2}8p ^{2}P^0	—	2s^{2}3d ^{2}D	2291.72	0.00127	0.00106	0.00094	0.00086	0.00081
2s^{2}7f ^{2}F^0	—	2s^{2}3d ^{2}D	2375.06	0.02547	0.01846	0.01450	0.01198	0.01042
2s^{2}5s ^{2}S	—	2s^{2}3p ^{2}P^0	2402.19	0.00299	0.00263	0.00240	0.00228	0.00231
2s^{2}7p ^{2}P^0	—	2s^{2}3d ^{2}D	2426.70	0.00213	0.00178	0.00158	0.00145	0.00137
2p^3 ^{2}D^0	—	2s2p^2 ^{2}P	2511.06	0.00101	0.00110	0.00122	0.00132	0.00140
2s^{2}8d ^{2}D	—	2p^3 ^{2}D^0	2542.83	0.00231	0.00182	0.00154	0.00136	0.00124
2s^{2}6f ^{2}F^0	—	2s^{2}3d ^{2}D	2574.84	0.05094	0.03643	0.02834	0.02325	0.02008
2s2p3p ^{2}D	—	2p^3 ^{2}D^0	2628.24	0.00372	0.00311	0.00272	0.00247	0.00231
2s^{2}6p ^{2}P^0	—	2s^{2}3d ^{2}D	2669.93	0.00399	0.00330	0.00291	0.00266	0.00252
2s^{2}4d ^{2}D	—	2s^{2}3p ^{2}P^0	2747.02	0.23657	0.17614	0.14152	0.11952	0.10602
2s^{2}3p ^{2}P^0	—	2s2p^2 ^{2}S	2840.90	0.88133	0.67092	0.56476	0.50663	0.47632
2s^{2}5f ^{2}F^0	—	2s^{2}3d ^{2}D	2992.63	0.13159	0.09165	0.07001	0.05663	0.04832
2s2p3p ^{2}P	—	2p^3 ^{2}D^0	3176.44	0.00240	0.00416	0.00526	0.00582	0.00604
2s^{2}5p ^{2}P^0	—	2s^{2}3d ^{2}D	3361.28	0.00192	0.00158	0.00140	0.00131	0.00128
2s2p3p ^{2}D	—	2s^{2}4p ^{2}P^0	3841.14	0.01381	0.01153	0.01008	0.00918	0.00858
2s^{2}4s ^{2}S	—	2s^{2}3p ^{2}P^0	3920.11	0.01809	0.01535	0.01382	0.01348	0.01440
2s2p3p ^{2}S	—	2p^3 ^{2}P^0	4017.84	0.00189	0.00202	0.00203	0.00203	0.00206
2s^{2}7d ^{2}D	—	2s^{2}4p ^{2}P^0	4018.88	0.00838	0.00660	0.00552	0.00480	0.00434

Table 5.13: Case B: Effective recombination coefficients (× 10^{12} cm^{3}s^{-1}) for low state transitions, $n, n' \leq 8$, at density of 10^4 cm^{-3}

Transition	Wavelength	Temperature (K)				
	Å	5000	7500	10000	12500	15000
$2s^24f\ ^2F^0$ — $2s^23d\ ^2D$	4267.18	0.57042	0.37538	0.27588	0.21696	0.18096
$2s^28f\ ^2F^0$ — $2s^24d\ ^2D$	4619.08	0.00943	0.00691	0.00546	0.00453	0.00394
$2s^26d\ ^2D$ — $2s^24p\ ^2P^0$	4638.51	0.00861	0.00666	0.00551	0.00474	0.00424
$2s^28p\ ^2P^0$ — $2s^24d\ ^2D$	4749.75	0.00112	0.00093	0.00083	0.00076	0.00071
$2s^28d\ ^2D$ — $2p^3\ ^2P^0$	4752.42	0.02075	0.01639	0.01381	0.01219	0.01119
$2s^23p\ ^2P^0$ — $2s2p^2\ ^2P$	4753.40	0.00175	0.00133	0.00112	0.00100	0.00094
$2s^28g\ ^2G$ — $2s^24f\ ^2F^0$	4802.68	0.01899	0.01298	0.00976	0.00777	0.00650
$2s2p3p\ ^2D$ — $2p^3\ ^2P^0$	5059.68	0.01979	0.01653	0.01444	0.01315	0.01230
$2s^27f\ ^2F^0$ — $2s^24d\ ^2D$	5122.21	0.01610	0.01167	0.00917	0.00757	0.00659
$2s^27g\ ^2G$ — $2s^24f\ ^2F^0$	5342.36	0.03656	0.02466	0.01836	0.01449	0.01196
$2s^27p\ ^2P^0$ — $2s^24d\ ^2D$	5368.59	0.00197	0.00165	0.00146	0.00134	0.00126
$2s^24p\ ^2P^0$ — $2s^23d\ ^2D$	5890.37	0.02160	0.01723	0.01469	0.01306	0.01204
$2s^26f\ ^2F^0$ — $2s^24d\ ^2D$	6151.44	0.03046	0.02178	0.01695	0.01390	0.01200
$2s^25d\ ^2D$ — $2s^24p\ ^2P^0$	6258.82	0.00795	0.00608	0.00498	0.00427	0.00380
$2s^26g\ ^2G$ — $2s^24f\ ^2F^0$	6461.94	0.08885	0.05854	0.04290	0.03349	0.02744
$2s^26d\ ^2D$ — $2p^3\ ^2P^0$	6540.71	0.00113	0.00087	0.00072	0.00062	0.00055
$2s^23p\ ^2P^0$ — $2s^24s\ ^2S$	6579.50	0.87805	0.66842	0.56266	0.50475	0.47454
$2s^26d\ ^2D$ — $2s^24f\ ^2F^0$	6622.14	0.00106	0.00082	0.00068	0.00059	0.00052
$2s^26p\ ^2P^0$ — $2s^24d\ ^2D$	6723.54	0.00412	0.00341	0.00301	0.00275	0.00260
$2s^23d\ ^2D$ — $2s^23p\ ^2P^0$	7234.73	1.04360	0.72509	0.55874	0.46464	0.41478
$2s2p3p\ ^2D$ — $2s^25p\ ^2P^0$	7541.31	0.00280	0.00234	0.00205	0.00186	0.00174
$2s^27d\ ^2D$ — $2s^25p\ ^2P^0$	8258.37	0.00139	0.00109	0.00091	0.00080	0.00072
$2s^28d\ ^2D$ — $2s2p3s\ ^2P^0$	8267.91	0.00741	0.00585	0.00494	0.00435	0.00400
$2s^28f\ ^2F^0$ — $2s^25d\ ^2D$	8869.06	0.00526	0.00385	0.00304	0.00253	0.00220
$2s^28g\ ^2G$ — $2s^25f\ ^2F^0$	9224.02	0.01621	0.01109	0.00833	0.00663	0.00555
$2s^25f\ ^2F^0$ — $2s^24d\ ^2D$	9229.63	0.06859	0.04777	0.03649	0.02952	0.02519
$2s^25s\ ^2S$ — $2s^24p\ ^2P^0$	9234.94	0.00182	0.00160	0.00146	0.00139	0.00141
$2s2p3p\ ^2D$ — $2s2p3s\ ^2P^0$	9244.57	0.00234	0.00195	0.00171	0.00155	0.00145
$2s^28h\ ^2H^0$ — $2s^25g\ ^2G$	9314.19	0.02215	0.01428	0.01029	0.00790	0.00634
$2s^25g\ ^2G$ — $2s^24f\ ^2F^0$	9903.43	0.34396	0.21699	0.15454	0.11825	0.09559
$2s^25d\ ^2D$ — $2p^3\ ^2P^0$	10301.05	0.00800	0.00612	0.00502	0.00429	0.00383
$2s^25d\ ^2D$ — $2s^24f\ ^2F^0$	10504.49	0.00338	0.00258	0.00212	0.00181	0.00162
$2s^27f\ ^2F^0$ — $2s^25d\ ^2D$	10930.58	0.00865	0.00627	0.00493	0.00407	0.00354
$2s^27g\ ^2G$ — $2s^25f\ ^2F^0$	11444.39	0.03048	0.02056	0.01530	0.01208	0.00997
$2s^27h\ ^2H^0$ — $2s^25g\ ^2G$	11579.09	0.05329	0.03367	0.02395	0.01823	0.01452
$2s^27p\ ^2P^0$ — $2s^25d\ ^2D$	12117.23	0.00172	0.00143	0.00127	0.00117	0.00110
$2s^25p\ ^2P^0$ — $2s^24d\ ^2D$	13946.90	0.00165	0.00136	0.00120	0.00112	0.00110
$2s^26d\ ^2D$ — $2s2p3s\ ^2P^0$	15767.93	0.00434	0.00336	0.00277	0.00239	0.00214
$2s^26f\ ^2F^0$ — $2s^25d\ ^2D$	17000.39	0.01471	0.01052	0.00818	0.00671	0.00580
$2s^28f\ ^2F^0$ — $2s^26d\ ^2D$	17562.19	0.00297	0.00218	0.00172	0.00143	0.00124
$2s^24d\ ^2D$ — $2s^24p\ ^2P^0$	17846.51	0.05093	0.03792	0.03047	0.02573	0.02283
$2s^26g\ ^2G$ — $2s^25f\ ^2F^0$	18198.85	0.06876	0.04531	0.03320	0.02592	0.02124
$2s^28g\ ^2G$ — $2s^26f\ ^2F^0$	18451.48	0.01140	0.00780	0.00586	0.00466	0.00390
$2s^26h\ ^2H^0$ — $2s^25g\ ^2G$	18516.37	0.20015	0.12241	0.08530	0.06402	0.05044
$2s^28h\ ^2H^0$ — $2s^26g\ ^2G$	18661.50	0.02442	0.01574	0.01134	0.00872	0.00699
$2s^26d\ ^2D$ — $2s^25f\ ^2F^0$	19529.37	0.00177	0.00137	0.00113	0.00098	0.00087
$2s^26p\ ^2P^0$ — $2s^25d\ ^2D$	22227.17	0.00414	0.00343	0.00302	0.00276	0.00261
$2s^27f\ ^2F^0$ — $2s^26d\ ^2D$	28030.37	0.00440	0.00319	0.00250	0.00207	0.00180

Table 5.14: Case B: Effective recombination coefficients ($\times\ 10^{12}$ cm^{3}s^{-1}) for low state transitions, $n, n' \leq 8$, at density of 10^4 cm^{-3}

Transition			Wavelength Å	Temperature (K) 5000	7500	10000	12500	15000
2s^{2}7g ^{2}G	—	2s^{2}6f ^{2}F^0	30154.38	0.02008	0.01355	0.01008	0.00796	0.00657
2s^{2}7h ^{2}H^0	—	2s^{2}6g ^{2}G	30688.20	0.05576	0.03523	0.02506	0.01908	0.01519
2s^{2}5d ^{2}D	—	2s^{2}5p ^{2}P^0	31210.82	0.01011	0.00773	0.00634	0.00542	0.00484
2s^{2}7p ^{2}P^0	—	2s^{2}6d ^{2}D	37430.37	0.00170	0.00142	0.00126	0.00116	0.00109
2s^{2}8f ^{2}F^0	—	2s^{2}7d ^{2}D	42189.85	0.00137	0.00100	0.00079	0.00066	0.00057
2s^{2}8g ^{2}G	—	2s^{2}7f ^{2}F^0	46442.59	0.00745	0.00510	0.00383	0.00305	0.00255
2s^{2}8h ^{2}H^0	—	2s^{2}7g ^{2}G	47268.44	0.01982	0.01277	0.00920	0.00707	0.00567
2s^{2}6p ^{2}P^0	—	2s^{2}6s ^{2}S	57822.12	0.00111	0.00092	0.00081	0.00074	0.00070

Table 5.15: Comparison of effective dielectronic recombination coefficients for λ1335, λ1037 and λ904, from this work, with effective dielectronic recombination coefficients from Storey (1981) as a function of electron temperature. Values given are $\alpha^{\rm eff}_{nl}(\lambda) \times 10^{12}$ cm^{3}s^{-1}.

Temperature (K)	λ1335 Storey	This Work	λ1037 Storey	This Work	λ904 Storey	This Work
7000	6.06	5.70	0.84	0.83	0.44	0.04(2)
8000	5.45	5.13	0.81	0.80	0.42	0.04(8)
9000	4.93	4.64	0.78	0.77	0.41	0.05(3)
10000	4.50	4.24	0.76	0.74	0.39	0.05(8)
11000	4.14	3.90	0.73	0.71	0.38	0.06(3)
12000	3.83	3.61	0.71	0.68	0.36	0.06(8)
13000	3.56	3.14	0.69	0.66	0.35	0.07(2)
14000	3.33	2.96	0.67	0.64	0.34	0.07(6)
15000	3.13	2.96	0.65	0.62	0.33	0.07(9)

The effective dielectronic coefficients arise from transitions from the first excited complex to the ground state 2s2p^2(^{2}D, ^{2}S, ^{2}P) $\rightarrow$ 2s^{2}2p ^{2}P^0 at λ1335, λ1037 and λ904 respectively. These are given in table (5.9.3). For transitions from ^{2}D and ^{2}S the results are in good agreement. The differences are explainable in view of the different approximations used in the evaluation of the radiative decay rates. The result for λ904 is more problematic. A comparison with Badnell (1988) who determined low temperature dielectronic recombination coefficients in intermediate coupling would seem to indicate that the results of Storey (1981) are of the right order of magnitude. The recombination coefficients for this state were reevaluated and the photoionisation cross-section checked, but no error could be found. The cross-section contains no large resonances (in terms of area) and the raw recombination coefficients are small. This discrepancy needs further investigation.

5.9.4 Total Recombination Coefficients of CII

Péquignot *et al.* (1991) calculated total recombination coefficients for several ions, including CII. They mostly used detailed photoionisation cross-sections, where available, for the ground and $n = 2$ excited states and cubic spline fits to the systematic cross-sections of Hofsaess (1979) for $n = 3$ levels. Scaled hydrogenic values were evaluated for all levels $n > 3$.

They gave a fit to the total recombination coefficient for each ion and expected an error of less that 10% in their values. Using the parameters to their fit, total recombination coefficients were calculated in the temperature range, 500 – 20000 K.

The comparison with Péquignot *et al.* (1991) is not directly meaningful since there is only a limited dielectronic component in their recombination coefficients. Total dielectronic recombination rates to CII were calculated by Storey (1981). These were combined with the Péquignot *et al.* (1991) results and the comparison is give in figure (5.4) The combined result of Storey (1981) and Péquignot *et al.* (1991) is larger that this work by ~15% at 7000 K, the lowest value at which Storey (1981) tabulates his total recombination coefficients. This difference is not unexpected in view of the differences in radiative transition probabilities between the works. Péquignot *et al.* (1991) make some, but not full, allowance for resonances formed by dielectronic recombination. Combining the two results may be an over estimate of the total recombination coefficient.

5.9.5 Effective Recombination Coefficients for Selected Lines

Effective recombination coefficients were calculated for a range of temperatures for the following lines:

Transition			Wavelength Å
4f $^2F^0$	→	5g ^2G	9903
3d ^2D	→	4f $^2F^0$	4267
3p $^2P^0$	→	3d ^2D	7231
3s ^2S	→	3p $^2P^0$	6581
2s2p^2 ^2S	→	3p $^2P^0$	2837
2s2p^2 ^2D	→	3p $^2P^0$	1761
2p $^2P^0$	→	2s2p^2 ^2D	1335

Comparison is made with Péquignot *et al.* (1991), who calculated effective recombination coefficients based mainly on scaled hydrogenic coefficients, with certain corrections

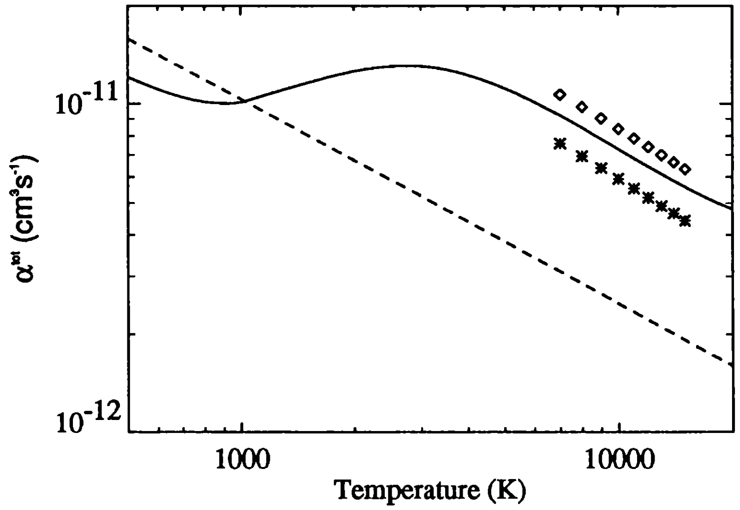

Figure 5.4: Total recombination coefficients for CII as a function of temperature. Comparison with Péquignot *et al.* (1991) (dashed line) and this work (solid line). ⋆ are the dielectronic values of Storey (1981) and the ◇ represents the combined value of Péquignot *et al.* (1991) and Storey (1981).

applied. Figures (5.5) and (5.6) illustrate the differences between their work and the results calculated here.

For $\lambda 4267$ and $\lambda 9903$, both of which are near hydrogenic transitions the agreement is excellent. For non-hydrogenic transitions where the principle quantum number changes, Péquignot *et al.* (1991) are much larger, particularly for $\lambda 1761$.

For allowed transitions within a given principle quantum number the results of Péquignot *et al.* (1991) are too small. This is particularly the case for $\lambda 6581$ which is a $^2P^0 \rightarrow {}^2S$ transition for $n = 3$, where the quantum defects are large and there are perturbations from non-hydrogenic states.

For $\lambda 1335$, the dielectronic component of Nussbaumer and Storey (1984) is combined with the radiative result of Péquignot *et al.* (1991) in order to gauge the accuracy of the values calculated here. As was expected, the combined rate is larger than this work. For transitions, other than those that are near hydrogenic, Péquignot *et al.* (1991) estimate their accuracy only to be in the 20 to 40 % range. This is reflected in the comparisons. One noticeable feature of the effective recombination coefficients is the appearance of the process of high temperature dielectronic recombination. In some cases it would appear to

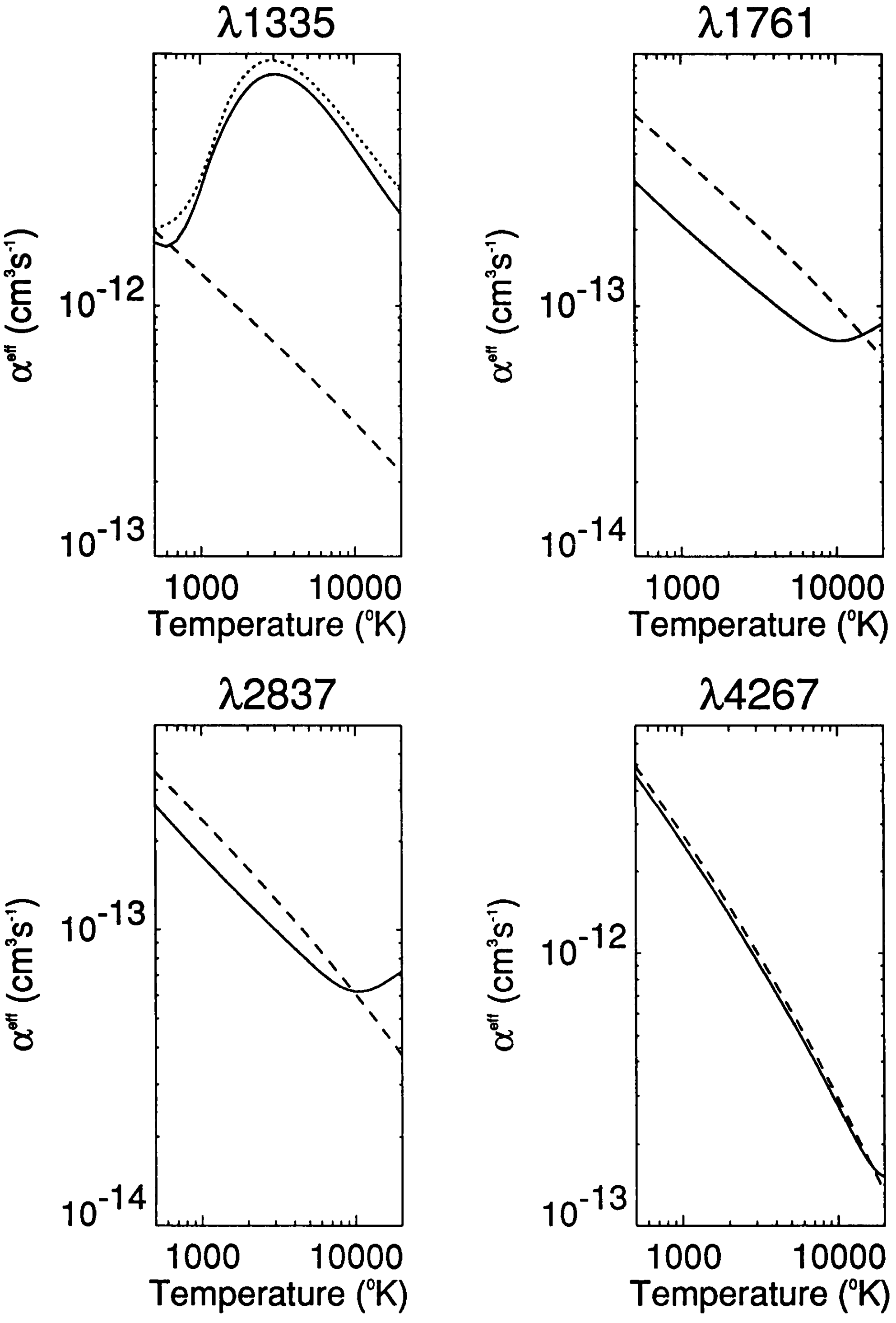

Figure 5.5: Effective recombination coefficients for λ1335, λ1761, λ2837 and λ4267 as a function of temperature. Comparison between Péquignot *et al.* (1991) (dashed line) and this work. The dotted line, for λ1335, represents the sum of the Péquignot *et al.* (1991) and Nussbaumer and Storey (1984) values.

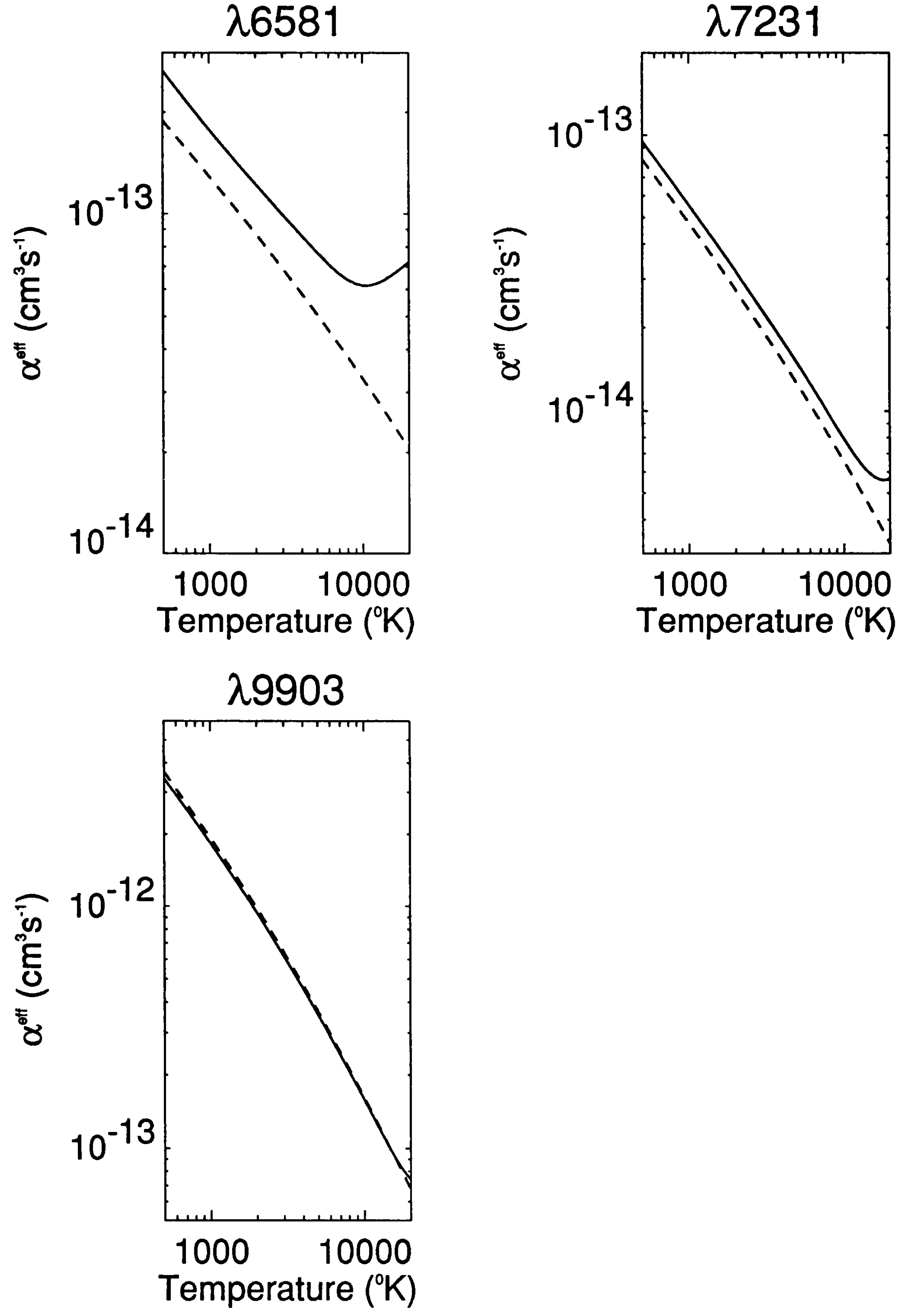

Figure 5.6: Effective recombination coefficients for $\lambda6581$, $\lambda7321$ and $\lambda9903$ as a function of temperature. Comparison between Péquignot *et al.* (1991) (dashed line) and this work.

be important at lower temperatures than was first estimated.

No attempt is made to more fully account for this process in these calculations and this places an upper limit on the validity of the calculations of ~17000 K.

5.10 Conclusions

This chapter presented solutions for the level population problems and an explanation of various approximations to the radiative and collisional rates used to describe the physical processes. In doing so new recombination coefficients and transition probabilities have been used. This chapter presented results in the form of wavelength tables for all low state transitions and generated effective recombination coefficients for those lines, for which a high degree of accuracy can be assumed. Comparison was made with previous work and the agreement found to be good in cases where it is expected to be so. In other cases it was shown that the approach of evaluating the radiative and dielectronic components of the recombination coefficient in a unified manner, led to accurate recombination coefficients which will differ from previously published values. For accurate results, the need for explicitly evaluating the photoionisation cross-sections for non hydrogenic states above the ground and first few excited states, was clearly demonstrated.

Chapter 6

Application to Observations

6.1 Introduction

In the previous chapter, a detailed listing of calculated wavelengths and case B effective recombination coefficients, applicable to nebular temperatures and density was given. The accuracy of the calculations was demonstrated by comparison to previous results. In this chapter, the application of the theoretical CII recombination spectra to the observations of two widely differing astrophysical plasmas is considered. Several regimes in which the use of a theoretically determined CII spectra could be applied were given in the introduction to this thesis. Two of the regimes mentioned in detail, are explored here. Firstly the results were applied to determining the temperature in the cold nova, DQ Herculis. Secondly, the density in the winds of the WC10 star CPD $-56^0 8032$ was determined, by modeling the observed fluxes of several lines obtained by Barlow and Storey (1994).

6.2 1934 Nova DQ Herculis

The nebula ejected in 1934 by the classical nova DQ Her is remarkable for its low temperature and relatively high ionisation state (Williams *et al.*, 1978). The temperature was determined from the width of the broad spectral feature attributed to hydrogen Balmer continuum emission by Williams *et al.* (1978). They argued, that the presence of Balmer lines requires continuum emission, however an emission line spectrum of this type generally originates in a gas of 10^4K, so the Balmer continuum is normally spread out over a much larger wavelength interval. The emission coefficient for Balmer emission above the threshold (λ3648) has a frequency dependence given by $j_\nu \propto \exp(-h\nu/kT_e)$, where T_e is the electron temperature. At low temperatures, the Balmer continuum radiation is confined to the relatively small wavelength interval and the width of the observed feature constrained the temperature to be ~500 K.

Ferland *et al.* (1984) combined previous and new IUE emission-line spectra and emission-line spectra taken using the Steward Observatory 2.3m telescope, to deduce several physical parameters, characterizing the cold nova DQ Her. They obtained the density and mass of the ionized gas and used the carbon recombination spectrum to deduce a low temperature and fairly high level of ionisation for the envelope.

Ferland *et al.* (1984) calculated effective recombination coefficients for the lines $2s^2 3d$ (^2D) - $2s^2 4f$ $(^2F^0)$ $\lambda4267$ and $2s^2 2p$ $(^2P^0)$ - $2s2p^2$ (^2D) $\lambda1335$. They noted that the 4267Å line is formed mainly by radiative recombination over the entire temperature range, while the 1335Å line is formed largely by dielectronic recombination for $T \gtrsim 400$ K. Over certain temperature ranges, the intensity ratio, $I(1335)/I(4267)$ can be used to estimate T_e. The intensity ratio will fall dramatically when $T < 10^3$K, because the allowed autoionizing 3d $^2F^0$ and 3d $^2P^0$ states, which decay to produce the $\lambda1335$ line, lie 3301 cm^{-1} and 5523 cm^{-1} above the ionization limit and would become inaccessible to the free electrons. The observed ratio is ~9(± 0.5 dex). Ferland *et al.* (1984) calculated the ratio, $I(1335)/I(4267)$ over a range of temperatures and by applying it to the observed intensity ratio, deduced a temperature of $T_e \simeq 700$ K. This value they argued, was sufficiently close to Williams *et al.*, 1978), whose temperature of ~500 K they adopted. Their effective recombination coefficients are reproduced in figure (6.1) for comparison.

Smits (1991), also considers the recombination spectra of CII in DQ Her using improved atomic data and more fully accounting for dielectronic recombination. His results differ significantly from Ferland *et al.* (1984). He found that the ratio of measured fluxes, $F(1335)/F(4267)$ supported a cool-gas interpretation but at a temperature of ~1300 K rather that 500 K.

6.2.1 Results

Effective recombination coefficients were generated in the course of comparisons with other results and applied to this problem. The effective recombination coefficients of the two lines and the ratio of the flux in the two lines are given graphically in figure (6.2) and in the table show over the page. The broad shape of the effective recombination lines is the same as given by Ferland *et al.* (1984). The ratio of intensities though differs considerably

Table 6.1: Effective recombination coefficients for the Carbon II lines, $\lambda4267$ and $\lambda1335$, and the theoretical flux ratio $F(1335)/F(4267)$ calculated in this work.

Temperature	$\alpha^{\mathrm{eff}}(\mathrm{cm}^3\mathrm{s}^{-1})$		$\frac{F(1335)}{F(4267)}$
K	$\lambda4267$	$\lambda1335$	
400	5.50210E-12	1.98946E-12	1.16
450	4.99608E-12	1.85913E-12	1.19
500	4.58149E-12	1.77113E-12	1.24
550	4.23476E-12	1.72098E-12	1.30
600	3.93993E-12	1.70744E-12	1.39
650	3.68576E-12	1.73660E-12	1.51
700	3.46411E-12	1.80255E-12	1.66
750	3.26890E-12	1.90761E-12	1.87
800	3.09551E-12	2.04727E-12	2.11
900	2.80064E-12	2.41499E-12	2.76
1000	2.55883E-12	2.87043E-12	3.59
1100	2.35653E-12	3.37816E-12	4.58
1200	2.18463E-12	3.90758E-12	5.72
1300	2.03657E-12	4.43481E-12	6.96
1400	1.90760E-12	4.94259E-12	8.28
1450	1.84912E-12	5.18538E-12	8.96
1500	1.79416E-12	5.41938E-12	9.65
1600	1.69355E-12	5.85820E-12	11.06
1800	1.52285E-12	6.61004E-12	13.87
2000	1.38333E-12	7.19455E-12	16.62
2500	1.12474E-12	8.03973E-12	22.85
3000	9.46317E-13	8.27645E-12	27.95
3500	8.15536E-13	8.17209E-12	32.03
4000	7.15467E-13	7.89227E-12	35.26
5000	5.72327E-13	7.14315E-12	39.89
6000	4.74861E-13	6.38166E-12	42.95
7500	3.75812E-13	5.40435E-12	45.96
9000	3.09061E-13	4.64419E-12	48.03
10000	2.75621E-13	4.23779E-12	49.14
11000	2.48400E-13	3.89538E-12	50.12
12000	2.26024E-13	3.60505E-12	50.98
12500	2.16353E-13	3.47630E-12	51.36
13000	2.07575E-13	3.35709E-12	51.69
14000	1.92422E-13	3.14371E-12	52.22
15000	1.80123E-13	2.95875E-12	52.50
17500	1.59861E-13	2.59089E-12	51.80
20000	1.51864E-13	2.31920E-12	48.81

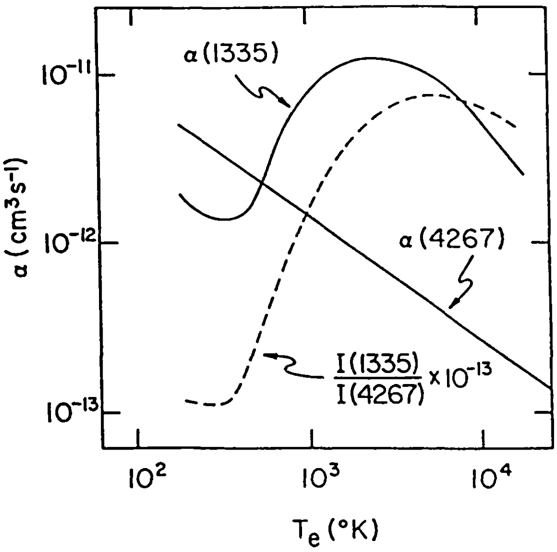

Figure 6.1: Carbon II recombination spectrum (Ferland *et al.*, 1984). Recombination coefficients for the Carbon II lines, λ4267 and λ1335 are shown as a function of temperature. The intensity ratio $I(1335)/I(4267)$ is also shown.

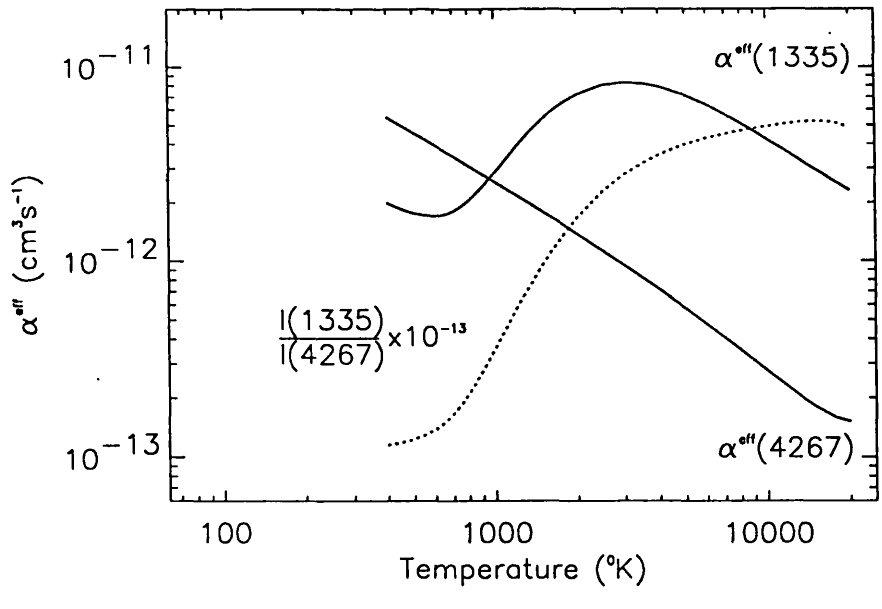

Figure 6.2: Effective recombination coefficients for the Carbon II lines, λ4267 and λ1335, and the flux ratio $I(1335)/I(4267)$ calculated in this work.

and seems to lean towards the higher temperature interpretation of Smits (1991). Using the observed ratio, the temperature derived is ~1450 K.

6.2.2 Discussion

The difference between the value of the temperature calculated here and that of Ferland *et al.* (1984) is large. This can be attributed almost wholly to the difference in the computed values of the effective recombination coefficients for λ1335, as the values for λ4267 were in good agreement. The value for λ1335, calculated by Ferland *et al.* (1984) at peak was ~15% larger the value calculated here. Some of the discrepancy will be due to the improved radiative data calculated in this thesis, but this alone is not enough to explain the difference. More likely, is that Ferland *et al.* (1984) have over estimated the contribution from the 2s2p3d $^2D^0$ state which lies very close to threshold. In LS-coupling, this state is forbidden to autoionise. However, in intermediate coupling, there will be weak interaction with the 2s2p3d $^2F^0$ and $^2P^0$ states. It is assumed that the autoionisation width is very much larger than the radiative width, so that although the interaction is weak, there may be a significant contribution arising from the $^2D^0$ state. Comparison was made with Badnell (1988) who calculated effective dielectronic recombination coefficients in intermediate coupling. His results are very close to those of this thesis for λ1335. This is shown in figure (6.6). They confirm that the rates of Ferland *et al.* (1984) are a substantial overestimate.

Smits (1991) also performed the comparison with Ferland *et al.* (1984) in LS-coupling, using more accurate radiative data. His result proved much closer to the value calculated here. The differences are explainable in terms of the improved approximations to recombination coefficients and transition probabilities, and the more complete description of the system, for instance, the inclusion of transitions from $n > 4$ into core excited states, which Smits (1991) omitted.

There maybe though a case for not trying to over-analyze the difference. The accuracy of using the width of the Balmer continuum to estimate the temperature may be difficult to gauge, particularly in this case as the observational uncertainties are large. Previous UV observations of DQ Her by Hartmann and Raymond (1981) derived a flux of half the Ferland *et al.* (1984) value for λ1335 and Ferland *et al.* (1984) state that their optical lines are only accurate to 10%-15%. Furthermore, the optical/UV ratios are based on spectra taken 2 years apart. Though the observed flux ratio points to a temperature of around

1450 K, this may be slightly misleading because of the observational uncertainties. It is apparent that more precise observations would be necessary before the discrepancies could be clearly addressed.

6.3 CPD $-56^0 8032$

CPD $-56^0 8032$ was first recognised as a cool carbon Wolf-Rayet star by Bidelman *et al.* (1968). Webster and Glass (1974) noted that it and three other similar late WC stars all had spectra in which CII dominated CIII, implying spectral types later than the latest type (WC9) of WC Wolf-Rayet stars, that had been defined up to that point.

The majority of CII lines in the optical spectrum are formed by recombination of C^{2+}. Many of the recombinations lines arise from the radiative decay and subsequent cascade, of strongly autoionising resonance states near the ionisation limit of C^+. These lines will be dominated by the low temperature dielectronic recombination component of the recombination coefficient as has been previously described. The populations of such resonance states are determined by the balance between autoionisation and radiative decay. Autoionisation usually dominates and the populations are then given by the Saha equation. The emissivity per electron and per recombining ion of a line originating from a resonance state will depend on its energy relative to the C^+ (^1S) ionisation limit, the probability for the transition in question and the electron temperature. The measured fluxes of such lines can be used to infer the electron temperature based on the assumptions that they are emitted from a region of uniform temperature and that the wind is optically thin to them.

CPD $-56^0 8032$ was observed with the 3.9m AAT on July 22 1981 using the RGO Spectrograph 25cm camera with an IPCS as detector. In their analysis, Barlow and Storey (1994) assumed the region of formation of the CII recombination lines to be of a consistent electron temperature and density and based on the relative intensities of four multiplets, derived a temperature of $T_e = 12800 \pm 1000$ K. This value was used to derive ratios of theoretical intensities, normalised to a line, which were then used to fit the measured fluxes to determine the density in the wind of CPD $-56^0 8032$.

6.3.1 Results

Ten lines from the spectrum of CPD $-56^0 8032$ were investigated in order to determine the density of the wind and these are illustrated overleaf. Using the temperature determined

Table 6.2: Case B ratios of theoretical fluxes, normalised to λ4267, for CPD $-56^0 8032$. The observed fluxes and their errors are also given.

Density	Flux_λ Ratios (normalised to λ4267)									
(cm^{-3})	λ2750	λ2992	λ4267	λ4802	λ5122	λ5342	λ6151	λ6258	λ6460	λ7235
Obs.	0.71	0.27	1.00	0.07	0.07	0.10	0.16	0.07	0.15	1.89
Err.	±0.10	±0.05	—	±0.01	±0.02	±0.01	±0.03	±0.01	±0.03	±0.26
1.0×10^6	0.57	0.27	1.00	0.04	0.04	0.07	0.07	0.02	0.16	2.19
1.0×10^7	0.58	0.27	1.00	0.04	0.04	0.07	0.07	0.02	0.16	2.20
1.0×10^8	0.60	0.28	1.00	0.04	0.04	0.07	0.07	0.02	0.16	2.25
1.0×10^9	0.62	0.28	1.00	0.04	0.04	0.07	0.07	0.02	0.16	2.28
1.0×10^{10}	0.63	0.28	1.00	0.04	0.04	0.07	0.09	0.02	0.16	2.36
5.0×10^{10}	0.65	0.29	1.00	0.04	0.05	0.07	0.08	0.02	0.16	2.33
1.0×10^{11}	0.66	0.30	1.00	0.04	0.06	0.07	0.09	0.02	0.16	2.41
2.0×10^{11}	0.66	0.32	1.00	0.05	0.07	0.08	0.10	0.02	0.17	2.39
5.0×10^{11}	0.66	0.37	1.00	0.05	0.08	0.08	0.12	0.02	0.18	2.42
8.0×10^{11}	0.64	0.41	1.00	0.05	0.08	0.08	0.14	0.02	0.19	2.42
1.0×10^{12}	0.63	0.43	1.00	0.05	0.08	0.08	0.14	0.02	0.20	2.41
5.0×10^{12}	0.53	0.52	1.00	0.03	0.06	0.06	0.12	0.02	0.16	2.16
1.0×10^{13}	0.46	0.45	1.00	0.02	0.04	0.04	0.09	0.02	0.12	1.94
5.0×10^{13}	0.29	0.24	1.00	0.01	0.02	0.02	0.04	0.01	0.05	1.53

by Barlow and Storey (1984), calculations were done at a range of densities from 10^6 – 5×10^{13} cm^{-3}. Both case A and B solutions were considered, and case B results are given in table (6.2), since these are generally more applicable to the observations.

In general for a state, though not for all states, there will be a region in which the population is sensitive to changes in density and the flux in the line will vary rapidly. The effects of density changes on the lines are considered individually.

λ2750 $2s^2 4d\ ^2D \rightarrow 2s^2 3p\ ^2P^0$: The observation of λ2750 probably falls at the high end of the range of sensitivity to density changes. The peak of the theoretical value falls within the error on the observation and can be used to infer a density of between 1.0×10^{11} and 5.0×10^{11} cm^{-3}.

λ2992 $2s^2 5f\ ^2F^0 \rightarrow 2s^2 3d\ ^2D$: The theoretical flux ratio exceeds the observational one for λ2992. However, by using the maximum error on the observation an upper limit of 2.0×10^{11} cm^{-3} is suggested. It can be assumed that in this case the theoretical value is in quite good agreement with the observed.

λ4267 $2s^2 4f\ ^2F^0 \rightarrow 2s^2 3d\ ^2D$: This is the line to which the others were normalised.

λ4802 $2s^2 8g\ ^2G \rightarrow 2s^2 4f\ ^2F^0$: The theoretical ratio of fluxes is again smaller in all cases than the observed. The line does not seem to be overly sensitive to density. The maximum value of the theoretical ratio puts it within two intervals of the error of the observed value.

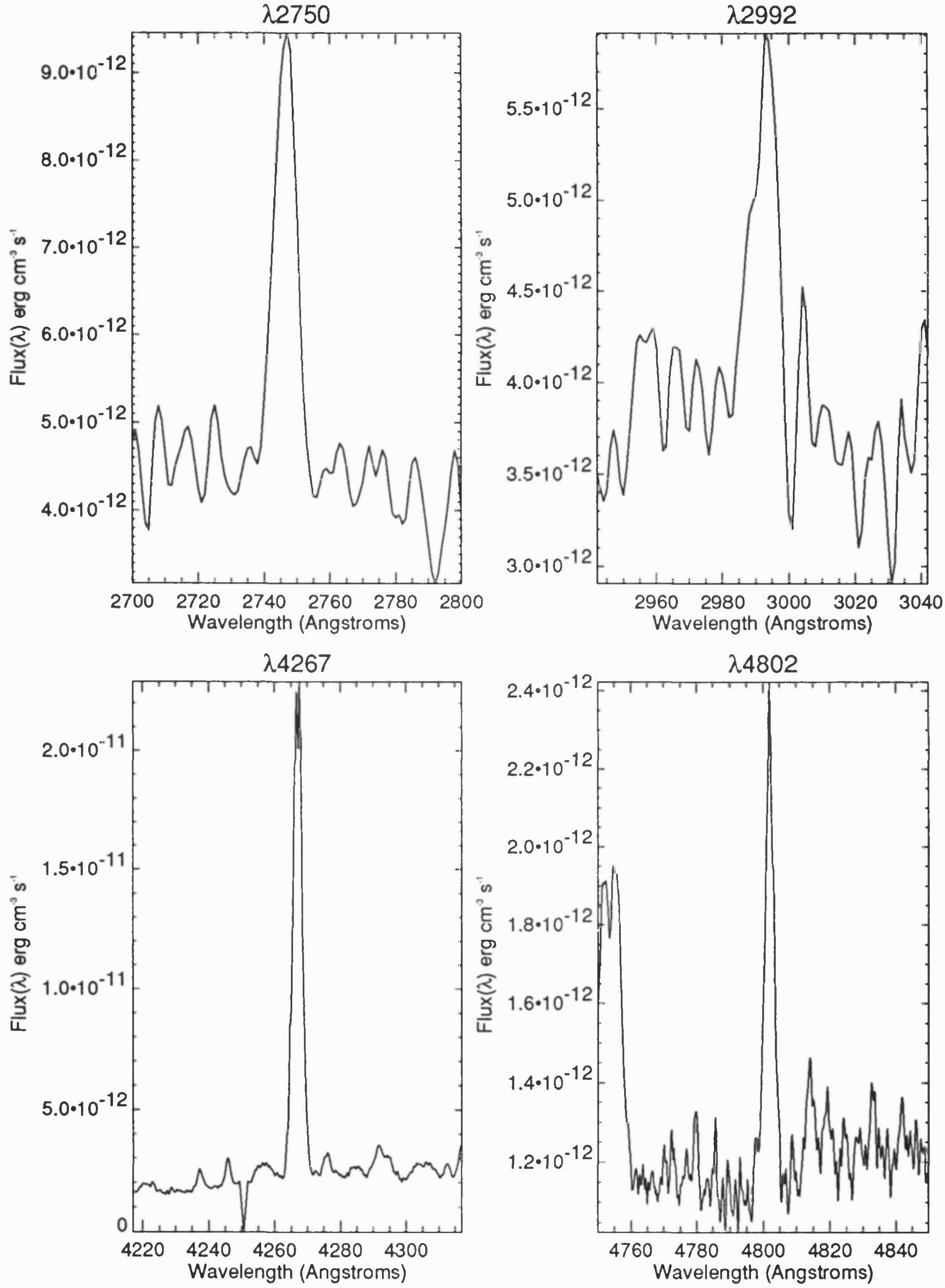

Figure 6.3: Lines in the spectrum of CPD $-56^{0}8032$ used to determine the density of its wind.

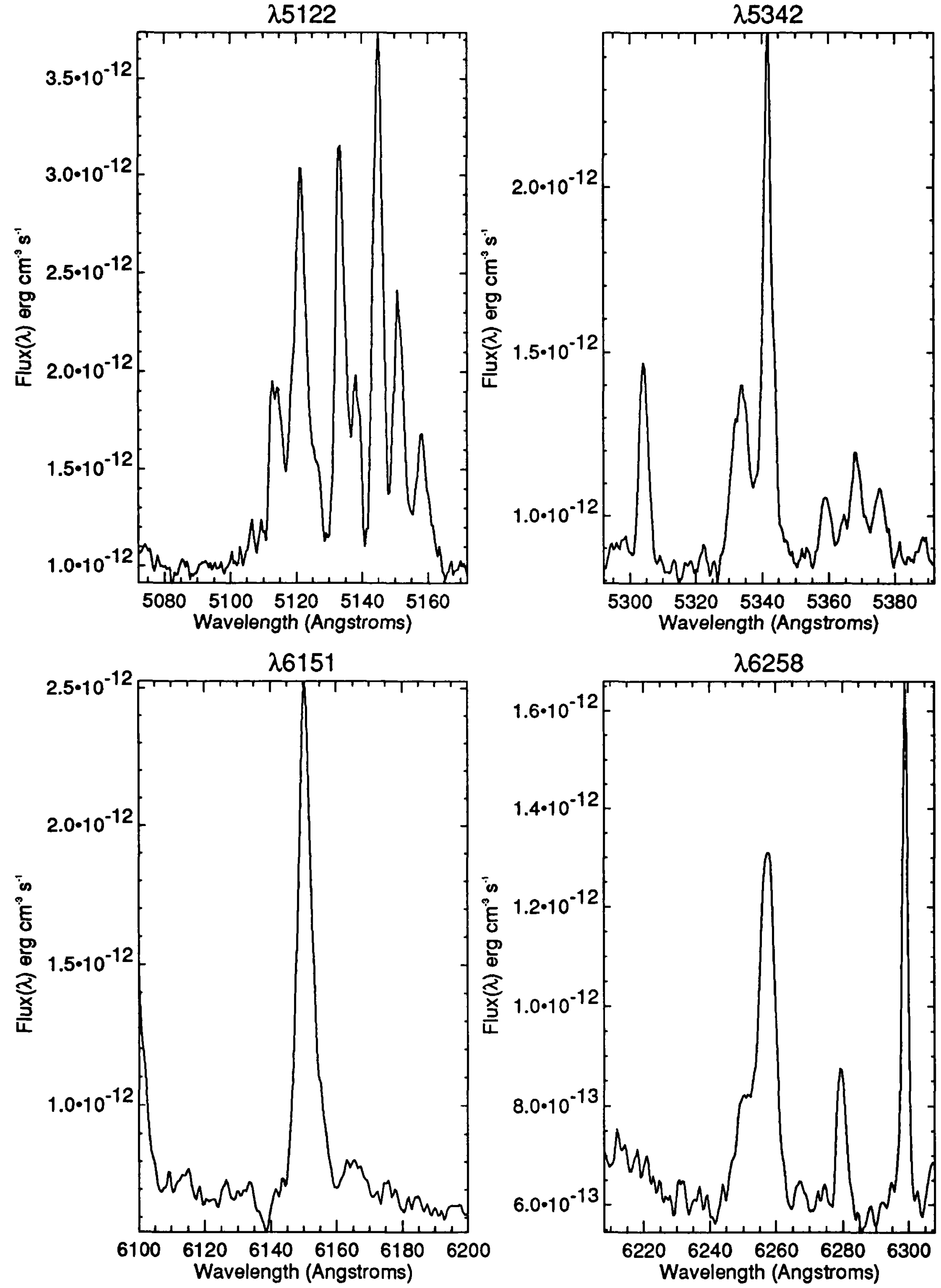

Figure 6.4: Lines in the spectrum of CPD $-56^{0}8032$ used to determine the density of its wind.

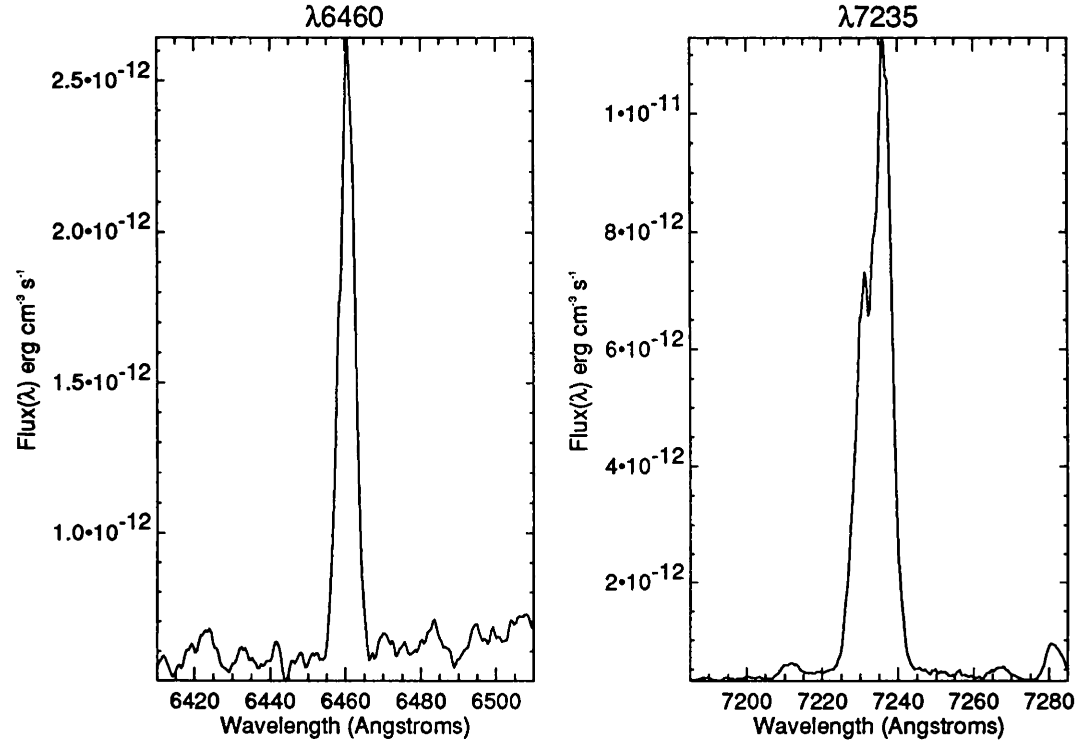

Figure 6.5: Lines in the spectrum of CPD $-56^0 8032$ used to determine the density of its wind.

This would give a boundary to the density of between 2.0×10^{11} and 1.0×10^{12} cm^{-3}.

λ5122 $2s^2 7f\ ^2F^0 \rightarrow 2s^2 4d\ ^2D$: The agreement between theoretical and observed flux ratios was very good. The observation falls at the high end, of the range at which changes in density have the most effect. A value of between 2.0 – 3.0×10^{11} cm^{-3} gives a ratio which matches the observation exactly.

λ5342 $2s^2 7g\ ^2G \rightarrow 2s^2 4f\ ^2F^0$: This line is not particularly sensitive to changes in the density. The theoretical flux ratio is slightly smaller than the observed. The closest values to the observed imply a density of between 2.0×10^{11} and 1.0×10^{12} cm^{-3}.

λ6151 $2s^2 6f\ ^2F^0 \rightarrow 2s^2 4d\ ^2D$: The theoretical flux ratios for this line are generally smaller than the observed value. However the observed flux for this line is actually larger than for λ6460. It is believed that this measurement is in error or that the true value lies at the extreme of the error on the measurement. The departure coefficient calculated for the 6f state is smaller than for 6g, so it will be less populated, and the transition probability will be smaller so the measured flux should be smaller. The flux ratios for λ6151 and λ6460, would be expected to be close since the difference in effective quantum number between 6f and 6g is not that great and this is what is seen in the theoretical calculations. Using the maximum error on the measurement a density range of between 6.0×10^{11} and 1.0×10^{12} cm^{-3} is inferred. The reason for the discrepancy is unclear, as the line does not appear to be significantly blended. The differences between the predicted and observed flux ratios make it unlikely that the error could be due to using a wrong value of the continuum in this region.

λ6258 2s^{2}5d ^{2}D → 2s^{2}4p ^{2}P^0: The theoretical ratio is much smaller than the observed seems stable to density changes. Examination of the observed line, figure (6.4), shows blending which has been accounted for. However it is possible that there are blends with other lines which have not been considered. This would seems the most likely explanation. There is also a possibility that the decay to the ground state is not entirely optically thick. This would however make the result worse not better. No information on the density could be obtained from this line.

λ6460 2s^{2}6g ^{2}G → 2s^{2}4f ^{2}F^0: The range of sensitivity to changes in density for this line are between 10^{11} and 10^{12} cm^{-3} as indicated by the theoretical calculations. The theoretical ratio is slightly larger than the observed value. Using the maximum error on the observed flux, the density is constrained to be not larger than 8.0×10^{11} cm^{-3}.

λ7235 2s^{2}3d ^{2}D → 2s^{2}3p ^{2}P^0: The theoretical ratio for this line exceeds that observed by approximately 25% in the case B calculations. However in the case A calculations, the theoretical ratio was too low by a factor of two. It can be inferred from this that the decay to the ground state is not completely optically thick. The values determined here represent an upper limit for the flux in the line. It is therefore not possible to use this line for density determination.

A summary of the values of density determined from fitting the ratios of theoretical and observed fluxes is given in table (6.3).

The general trend of the results would seem to indicate a value of the density of $\sim 2.0 \times 10^{11}$ cm^{-3}. In order to refine this result and obtain a measure of its accuracy χ^2 fits were obtained using the observed values and their errors. This was done using seven lines. λ6258 and λ7235 were excluded because no meaningful value of the density could be estimated from them. λ4267 was also excluded as this was the value against which the fluxes were normalised. The value of the density was changed to minimise χ^2. In this way a value of the density was obtained consistent with the observed fluxes and their errors. An estimate of the error was derived by determining the densities at which χ^2 is changed

Table 6.3: Summary of density fits to lines CPD $-56^0 8032$.

Wavelength (Å)	Density (cm^{-3})	Comments
λ2750	$(1.0 - 5.0) \times 10^{11}$	Nearest range of values within observational error.
λ2992	$< 2.0 \times 10^{11}$	Upper limit derived using maximum error on observation.
λ4267		Line used for normalization.
λ4802	$2.0 \times 10^{11} - 1.0 \times 10^{12}$	Line insensitive to density changes. Density inferred from maximum error on observation.
λ5122	$(2.0 - 3.0) \times 10^{11}$	Exact match !
λ5342	$2.0 \times 10^{11} - 1.0 \times 10^{12}$	Inferred from nearest value to observed.
λ6151	$6.0 \times 10^{11} - 1.0 \times 10^{12}$	Values derived using maximum error on observation. Observational measurement in error ?
λ6258	—	No meaningful estimate of density could be obtained.
λ6460	$< 8.0 \times 10^{11}$	Limit derived using maximum error on observation.
λ7235	—	Decay to ground state, not completely optically thick. Not usable for density determination.

by unity. A value of,

$$N_e = (2.69 \pm 0.71) \times 10^{11} \quad \mathrm{cm}^{-3} \tag{6.1}$$

was derived. This value is consistent with the range of densities expected from WC10 Population II stars. Values of the temperature outside the error range given by Barlow and Storey (1984) were tested. None gave a smaller χ^2 than 12800 K and it can be assumed that their analysis of the temperature is also accurate.

It has been shown that certain lines are sensitive density diagnostics and the applicability of the theoretical fluxes calculated here, to density determination has been demonstrated.

Previous work (e.g. Kane *et al.*, 1980) noted anomalous Carbon abundances in early type stars, deduced using the CII λ4267 line. It was thought that this may be due to anomalies in the λ4267 fluxes. No such anomalies were detected in these calculations.

6.4 A Summary of Work Presented in this Thesis

The starting point for this thesis, was the accurate calculation of photoionisation cross-sections for Carbon II. This was done by making use of the Opacity Project suite of codes and the accurate target constructed by Berrington *et al.* (1987). Special care was taken to ensure that resonances in the cross-sections were accurately mapped. In the course of these calculations energy levels for all states of CII up to $n = 15$ and $L = 4$ were calculated. A comparison with the experimental energies of Moore (1970) was made where the data was available. New transition probabilities were calculated, using weighted oscillator strengths obtained by running STGBB, from the Opacity Project codes. Comparison was made, for the doublet states, with the previous work of Yu Yan *et al.* (1987) and an indication of the improvement in the calculated values was gained, by comparing the theoretically determined lifetimes, with the experimental values of Reistad *et al.* (1986). Below threshold interpolation in low state ($n \leq 5$) photoionisation cross-sections was also done to ensure accurate transition probabilities from higher states. Highly accurate recombination coefficients were calculated, taking advantage of the unified treatment of radiative and dielectronic recombination. Further accuracy was achieved by moving prominent near threshold resonances so that their contribution could be assessed at experimental energies. A complete collisional-radiative-cascade treatment of the level populations of Carbon II was solved and wavelengths and effective recombination coefficients produced The accuracy of the results was tested and comparisons with other authors given. In the last chapter, the application of the work was ably demonstrated with firstly a comparison with the work by Ferland *et al.* (1984) on temperature determination in the old, cold nova DQ Herculis. The temperature derived is significantly larger than that proposed by Ferland *et al.* (1984), a result that can largely be explained in terms of the improved atomic data. Finally, theoretically determined fluxes were used to determine the density in the wind of the cool WC10 star CPD $-56^{0}8032$, by matching the observed fluxes determined by Barlow and Storey (1994).

6.5 Conclusions, Limitations and Future Work

This thesis has demonstrated that by applying a uniform approach to the calculation of radiative data and the use of suitable approximations for collisional rates, an accurate, theoretical spectra for CII may be generated, suitable for using as an accurate diagnostic tool in the analysis of the fundamental parameters of astrophysical plasmas. The necessity of treating excited levels in a more sophisticated manner has been shown to be an integral part of this. Scaled hydrogenic rates may only differ by a few percent from rates calculated here for states with a low quantum defect, but are not good estimates for low angular momentum states.

One of the main limitations of the work carried out in this thesis is that it has been done completely in LS-coupling and therefore only includes classically allowed transitions. For

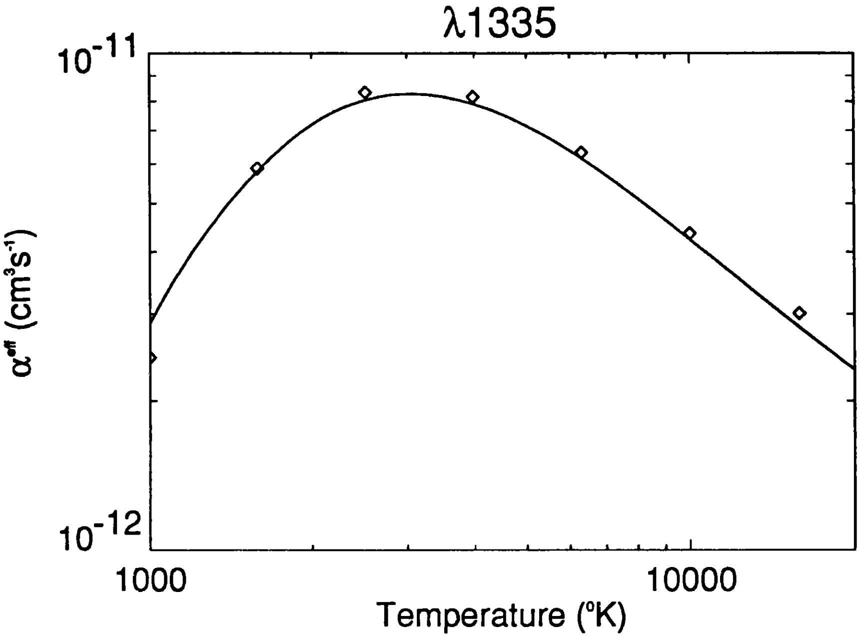

Figure 6.6: Effective recombination coefficients for λ1335. The ◇ represents the dielectronic recombination coefficients of Badnell (1988) calculated in intermediate coupling. The solid line represents this work which will include a radiative component.

low atomic mass and low effective charge ions, the departures from LS-coupling should be negligible. Storey (1994) noted, however that LS-coupling was not a good approximation for f and g states of O^+.

Badnell (1988) calculated total and effective, dielectronic recombination rate coefficients for several ions including C^+. The effective dielectronic recombination rate coefficient for λ1335, is compared here to the total effective recombination rate for λ1335, calculated previously in this work. λ1335 is suitable for comparison as it is dominated by the dielectronic component down to very low temperatures. The comparison is given in figure (6.6). For λ1335 any difference in the two results is generally small throughout the temperature range but there are discrepancies at high and low temperatures. At higher temperatures, the difference is due to high temperature dielectronic recombination. This can be used to give an upper bound on the range of application of the work in this thesis of ~17000 K, which is lower than first thought. At low temperatures the values of Badnell (1988) are smaller than this work. This is due to contributions from the background and resonance widths, which Badnell (1988) will lack. Generally, the effective recombination coefficients of Badnell (1988) are a few percent larger than this work. This is almost certainly due to the 2s2p3p $^2D^0$ resonance which lies close to threshold. Though forbidden to autoionise in LS-coupling it will be included in Badnell (1988) as his calculations were performed in intermediate coupling.

For the $2s2p^2$ ^2D state, departures from LS-coupling are not identifiable. A rough comparison of the total dielectronic recombination coefficient calculated for CII, by Badnell (1988), coupled with the total radiative coefficient, with the total recombination coefficient calculated in this work was done. This showed that the differences were generally small between the rates except above ~15000 K where the rate of Badnell (1988) increases rapidly because his calculations include the effects of high temperature dielectronic recombination. It can be concluded that LS-coupling is a good approximation for CII particularly at low temperatures. However as the ion charge increases core-fine structure interactions become stronger leading to stronger quartet-quartet lines. The quartet-quartet lines are much weaker than the doublet-doublet in CII, but should be accounted for, and would give a more complete approximation. Moving to an intermediate coupling scheme would also allow the inclusions of forbidden lines.

Much has been made of the generation of a homogeneous set of radiative data. Ideally this should be extended to the collisional rates.

It is hoped that the use of the carbon recombination spectrum as a diagnostic tool can be used in other regimes and in similar objects to those mentioned.

Aldrovandi S. M. V. & Péquignot D., 1973 *Astron. Astrophys.* **25**, 137

Badnell N. R., 1988 *J. Phys. B* **21**, 749

Barlow M. J. and Storey P. J., 1994 *Personal Communication*

Bates D. R. & Damgaard A., 1949 *Phil. Trans. A* **242**, 101

Berrington K. A., Burke P. G., Chang J. J., Chivers A. T., Robb W. D. & Taylor K. T., 1974 *Comp. Phys. Comm.* **8**, 149

Berrington K. A., Burke P. G., Dufton P. L. & Kingston A. E., 1977 *J. Phys. B* **10**, 1465

Berrington K. A., Burke P. G., Le Dorneuf M., Robb W. D., Taylor K. T. & Vo Ky Lan, 1978 *Comp. Phys. Comm.* **14**, 367

Berrington K. A., Burke P. G., Butler K., Seaton M. J., Storey P. J., Taylor K. T. & Yu Yan, 1987 *J. Phys. B* **20**, 6379

Bidelman W. P., MacConnell D. J. & Bond H. E., 1968 *IAU Circular No 2089*

Brocklehurst M., 1971 *Mon. Not. R. Astr. Soc.* **153**, 471

Burgess A. and Seaton M. J., 1960 *Mon. Not. R. Astr. Soc.* **120**, 121

Burgess A., 1963 *Proc. Phys. Soc.* **81**, 442

Burgess A., 1965 *Mem. R. Astr. Soc.* **69**, 1

Burgess A. and Percival I.C., 1968 *Adv. At. Mol. Phys.* **4**, 109

Burgess A. and Summers H. P., 1976 *Mon. Not. R. Astr. Soc.* **174**, 345

Burke P. G., Hibbert A & Robb W. D., 1971 *J. Phys. B* **4**, 153

Buttle P. J. A., 1967 *Phys. Rev* **160**, 719

Dufton P. L., Berrington K. A., Burke P. G. & Kingston A. E., 1978 *Astron. Astrophys.* **62**, 111

Eissner W., Jones M. & Nussbaumer H., 1974 *Comp. Phys. Comm.* **15**, 23

Fano U., 1961 *Phys. Rev.* **124**, 1866

Ferland G. J., Williams R. E., Lambert D. L., Shields G. A., Slovak M., Gondhalekar P. M. & Truran J. W., 1984 *Astrophys. J.* **281**, 194

Gailitis M., 1963 *Sov. Phys.-JETP* **17**, 1328

Gordon W., 1929 *Ann. Phys.* **2**, 1031

Griffin D. C., 1989 *Physica Scripta* **T28**, 17

Hartmann L. & Raymond J., 1981 *The Universe at UV Wavelengths*, ed. Chapman R O (NASA Conf. Pub. 2171), 495

Hibbert A., 1975 *Comp. Phys. Comm.* **9**, 141

Hofsaess D., 1979 *At. Data & Nuc. Data Tables* **24**, 285

Hummer D. G. & Storey P. J., 1987 *Mon. Not. R. Astr. Soc.* **224**, 801

Infeld L. & Hull T. E., 1951 *Rev. Mod. Phys.* **23**, 21

Kane L., McKeith C. D. & Dufton P.L, 1980 *Astron. Astrophys.* **84**, 115

Kwong V. H. S., Fang Z. Gibbons T.T., Parkinson W. H. & Smith P. L., 1993 *Astrophys. J.* **411**, 431

Liu X.-W., Storey P. J. & Barlow M. J., 1994 *Mon. Not. R. Astr. Soc.* (in press)

Lynas-Gray A. E., 1991 *Personal Communication*

Martin P. G., 1988 *Astrophys. J. Supp.* **66**, 125

Méndez R. H., Herrero A., Manchado A. & Kudritzki R. P., 1991 *Astron. Astrophys.* **252**, 265

Mendoza C., 1982 *Planetary Nebulae, IAU Symposium* No **103**

Moore C. E., 1970 *Atomic Energy Levels* (National Bureau of Standards, USA)

Nussbaumer H. & Storey P. J., 1978 *Astron. Astrophys.* **64**, 139

Nussbaumer H. & Storey P. J., 1983 *Astron. Astrophys.* **126**, 75

Nussbaumer H. & Storey P. J., 1984 *Astron. Astrophys. Suppl. Ser.* **56**, 293

Peach G., 1967 *Mem. R. Astr. Soc.* **71**, 13

Pengelly R. M. & Seaton M. J., 1964 *Mon. Not. R. Astr. Soc.* **127**, 165

Péquignot D., Petitjean P. & Boisson C., 1991 *Astron. Astrophys.* **251**, 680

Percival I. C., 1973 *J. Phys. B* **6**, 2236

Percival I. C. & Richards D., 1978 *Mon. Not. R. Astr. Soc.* **183**, 329

Petitjean P., Boisson C. & Péquignot D., 1990 *Astron. & Astrophys* **240**, 433

van Regemorter H., Hoang Binh D. Y. & Prud'homme M., 1979 *J. Phys. B* **12**, 1053

Reistad N., Hutton R., Nilsson A. E., Martinson I. & Mannervik S., 1986 *Physica Scripta* **34**, 151

Seaton M. J., 1955 *Mon. Not. R. Astr. Soc.* **68**, 457

Seaton M. J., 1961 *Proc. Phys. Soc.* **77**, 174

Seaton M. J., 1962 *Proc. Phys. Soc.* **79**, 1105

Seaton M. J., 1983 *Rep. Prog. Phys.* **46**, 167

Seaton M. J., 1985 *J. Phys. B* **18**, 2111

Seaton M. J., 1987 *J. Phys. B* **20**, 6363

Smits D. P., 1991 *Mon. Not. R. Astr. Soc.* **248**, 193

Storey P. J., 1972 *PhD Thesis* University Of London

Storey P. J., 1981 *Mon. Not. R. Astr. Soc.* **195**, 27

Storey P. J., 1982 *Planetary Nebulae IAU Symposium* No **103**, 199

Storey P. J., 1992 *Personal Communication*

Storey P. J., 1993 *Personal Communication*

Storey P. J., 1994 *Astron. Astrophys.* **282**, 999

Storey P. J. & Hummer D. G., 1991 *Comp. Phys. Comm.* **66**, 129

Summers H. P., 1977 *Mon. Not. R. Astr. Soc.* **178**, 101

Webster B. L. & Glass I. S., 1974 *Mon. Not. R. Astr. Soc.* **166**, 491

Williams R. E., Woolf N. J., Hege E. K., Moore R. L. & Kopriva D. A., 1978 *Astrophys. J.* **224**, 171

Williams R. E., 1982 *Astrophys. J.* **261**, 170

Wolf C. & Rayet G., 1867 *Comptes Rendues* **65**, 292

Yu Yan & Seaton M. J., 1987 *J. Phys. B* **20**, 6409

Yu Yan, Taylor K. T. & Seaton M. J., 1987 *J. Phys. B* **20**, 6399

Yu Yan, 1986 *PhD Thesis* University Of London